The Thesis Committee for Lauren Patricia Redmond
Certifies that this is the approved version of the following thesis:

Lithofacies, Depositional Systems, and Depositional Model of the Mississippian Barnett Formation in the Southern Fort Worth Basin

APPROVED BY
SUPERVISING COMMITTEE:

Supervisor:

Robert G. Loucks

Co-Supervisor:

Harold D. Rowe

Charles Kerans

William Fisher

Lithofacies, Depositional Systems, and Depositional Model of the Mississippian Barnett Formation in the Southern Fort Worth Basin

by

Lauren Patricia Redmond, B.S.; B.A.

Thesis

Presented to the Faculty of the Graduate School of

The University of Texas at Austin

in Partial Fulfillment

of the Requirements

for the Degree of

Master of Science in Geological Sciences

The University of Texas at Austin

August, 2016

Dedication

To my parents, sister, family, and friends. Thank you all for your support and love.

Acknowledgements

I would like to thank Dr. Robert Loucks, my supervisor, and Dr. Harold Rowe, my co-supervisor, for their knowledge, guidance, and support throughout this project. I would also like to thank Dr. Stephen Ruppel for helpful comments on this project and the other members of my committee, Dr. Charles Kearns and Dr. William Fisher, for edits that improved this work. Thank you to my fellow graduate students, especially my officemate Ningjie Hu, for support and friendship during our time together in graduate school. Thank you to all other faculty and staff members at the Jackson School of Geosciences and the Bureau of Economic Geology who helped to make this research move forward. Thank you to the staff of the Core Repository Center for all your assistance.

This work was supported by the State of Texas Advanced Oil and Gas Resource Recovery program (STARR), led by William A. Ambrose (STARR-30), at the Bureau of Economic Geology, I very much appreciate being a part of this research consortium; and by Statoil through the University of Texas at Austin Statoil Fellows program. This work also received financial support from the Jackson School of Geosciences at the University of Texas at Austin.

Abstract

Lithofacies, Depositional Systems, and Depositional Model of the Mississippian Barnett Formation in the Southern Fort Worth Basin

Lauren Patricia Redmond, M.S. Geo. Sci.

The University of Texas at Austin, 2016

Supervisor: Robert G. Loucks

Co-Supervisor: Harold D. Rowe

The Barnett Formation in the Llano Uplift region of the southern Fort Worth Basin of north-central Texas is an Osagean-Chesterian age siliciclastic mudrock whose deposition was influenced by the structurally stable Llano Uplift, topographic variabilities, and a long-term, second-order sea-level rise. Pervious work has mostly focused on the producing northern portion of the basin. The present study uses a group of 29 cores to: (1) characterize the Barnett lithofacies, (2) define the depositional setting of each lithofacies and develop a coherent depositional model, (3) identify stacking patterns and correlative surfaces, and (4) establish a viable sequence stratigraphic framework for the succession.

On the basis of core data, the Barnett strata are interpreted to have been deposited in a basinal setting, below storm-weather wave-base, under predominantly anoxic bottom waters. The analysis of core and thin sections revealed four dominant lithofacies: (1) laminated siliceous mudstone, (2) laminated calcareous siliceous mudstone, (3) skeletal

packstone, and (4) phosphatic packstone and grainstone. Facies stacking patterns were correlated using phosphatic packstone facies as regional marker beds. These beds coincide with changes in clay-mineral abundances, revealed by chemostratigraphic data, and their occurrences were used to subdivide the Barnett strata into lower, middle, and upper units.

The lower Barnett is characterized by cyclic sedimentation of extrabasinal clays and has the greatest thickness variability related to accumulation of the calcareous siliceous mudstone facies in graben structures. The middle Barnett is characterized by an increase in extrabasinal clay abundance compared to the lower Barnett, and the upper Barnett is characterized by a decrease in the extrabasinal clay abundance compared to the lower and middle Barnett. The phosphatic packstone facies is sourced from the outer shelf/upper slope of the adjacent Chappel Shelf and is interpreted to represent cycle tops within the aggradational stacking pattern that characterized sediment accumulation style during the second-order sea-level rise that occurred throughout Barnett deposition.

The findings contribute to the understanding of the stratal architecture and depositional history of the Barnett deep-water mudrocks and are used to refine the lithofacies variability of the Barnett Formation.

Table of Contents

List of Tables

List of Figures

INTRODUCTION

The Barnett Formation is a Mississippian (Osagean-Chesterian) age (Hass, 1953) siliciclastic mudrock succession (Figure 1) composed of laminated siliceous mudstone, laminated calcareous siliceous mudstone, skeletal packstone, and phosphatic packstone and grainstone. The Barnett accumulated along the southern margin of Laurussia prior to the late Paleozoic Ouachita orogeny as the Gondwana plate approached the Laurussian craton and created the Fort Worth Basin (FWB) (Figure 2) (Walper, 1982; Meckel et al., 1992; Blakey, 2005).

The Barnett strata in the northern FWB were commercially developed for gas production in 1981, and today the Newark East field (Figure 3) remains an active shale-gas, shale-oil system (Curtis, 2002; Pollastro, 2007). Only recently, in 2013, the Barnett Formation was surpassed by the Marcellus Shale as the largest gas trend in the United States based on proven reserves, and because the Barnett Formation is a historically prolific gas reservoir, previous work has focused on the producing area of the FWB and many studies were related to the organic geochemistry of the strata. The present study investigates the low-thermal maturity, organic-rich mudrocks of the southern FWB using a series of shallow-subsurface cores (current burial depth: 93 to 2354 ft; 28 to 717 m) (Table 1; Figure 4). Specific works pertinent to the study include: Loucks and Ruppel (2007); Rowe et al., (2008); Hoelke (2011); Wood (2013); and Reed and Loucks (2015). Other relevant works include Papazis (2005); Monroe (2007); and Loucks et al., (2009).

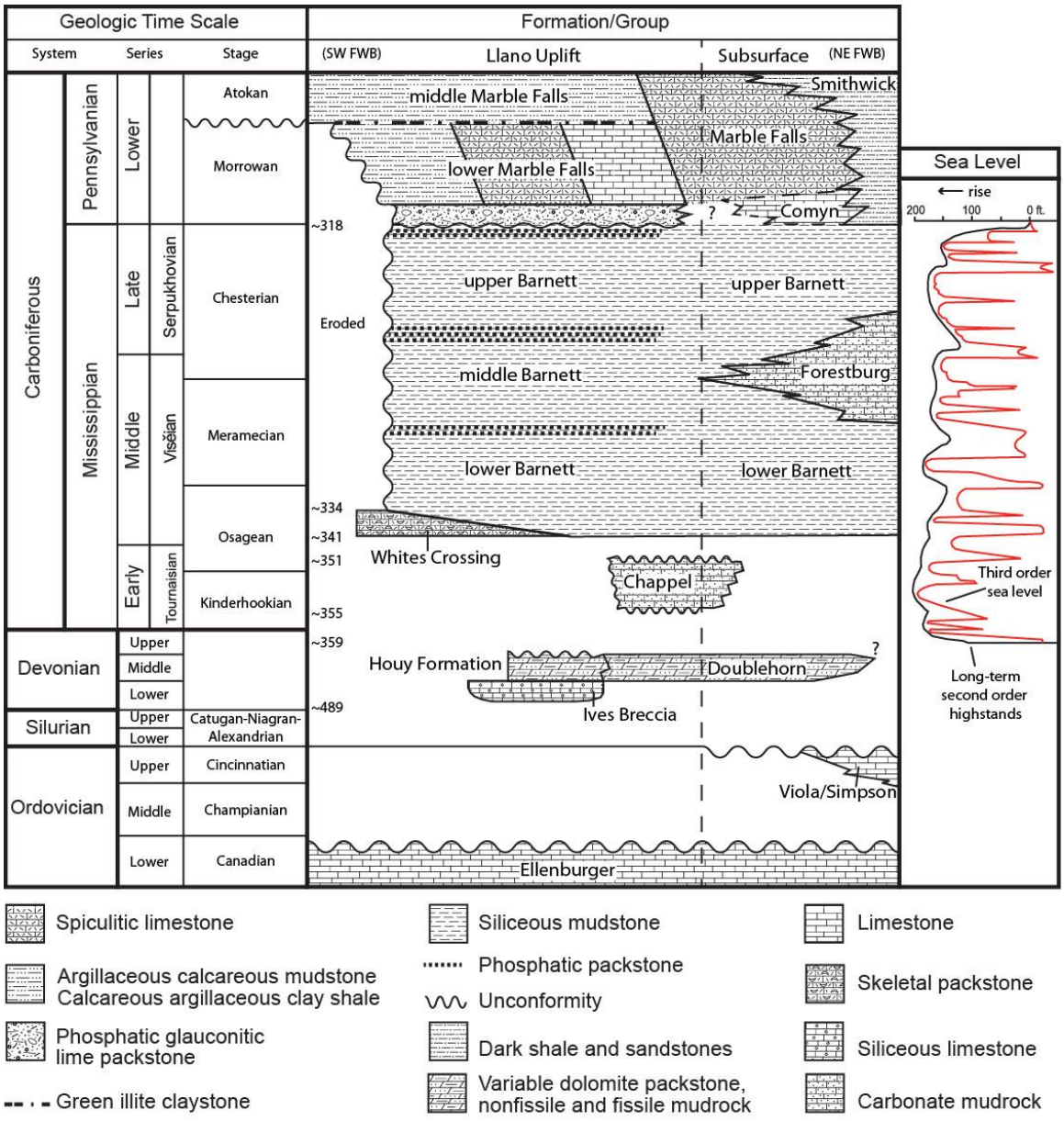

Figure 1: Stratigraphic column of the Ordovician to Pennsylvanian section in the southern FWB. Cores used in this study are located in the southern FWB. Strata relationships are based on data from this study, Loucks and Ruppel (2007), Wood (2013), as well as Crosby and Mapel (1975), Kier (1980), Lovick et al. (1982), Namy (1982), Watson (1980), Pollastro (2003), Erlich and Coleman (2005), and Farrar and Breyer (2011). Eustasy curve is modified from Ross and Ross (1987).

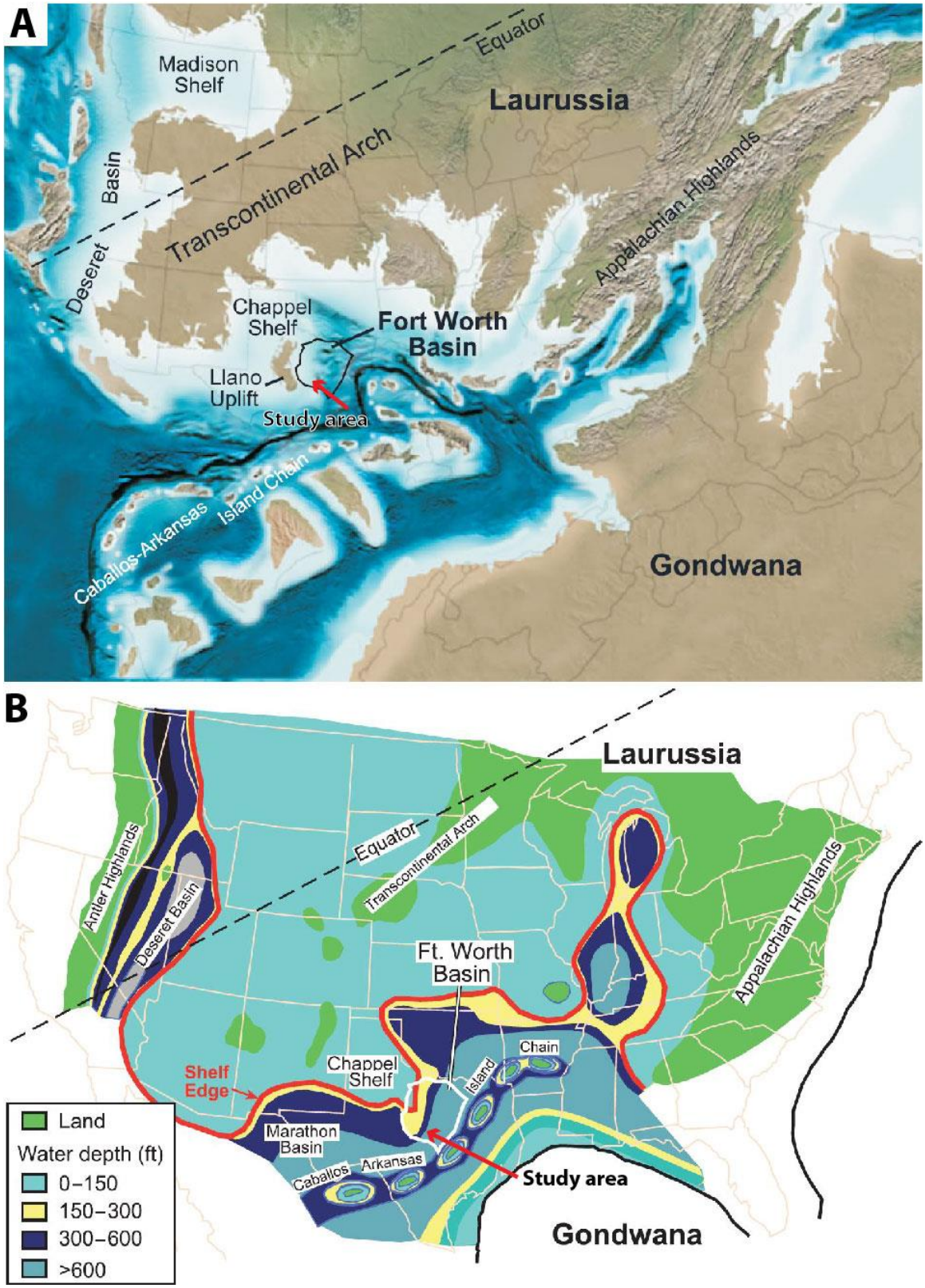
A
Equator
Madison Shelf
Laurussia
Transcontinental Arch
Deseret Basin
Appalachian Highlands
Chappel Shelf
Fort Worth Basin
Llano Uplift
Study area
Caballos-Arkansas
Island Chain
Gondwana
B
Laurussia
Equator
Transcontinental Arch
Antler Highlands
Deseret Basin
Ft. Worth Basin
Appalachian Highlands
Shelf Edge
Chappel Shelf
Island Chain
Marathon Basin
Caballos
Arkansas
Study area
Gondwana
Land
Water depth (ft)
0–150
150–300
300–600
>600

Figure 2: Paleogeographic maps of North American southern mid-continent region in the (A) late Mississippian (325 Ma) (Blakey, 2005) and (B) middle Mississippian (Gutschick and Sandberg, 1983). Slightly modified by Loucks and Ruppel (2007).

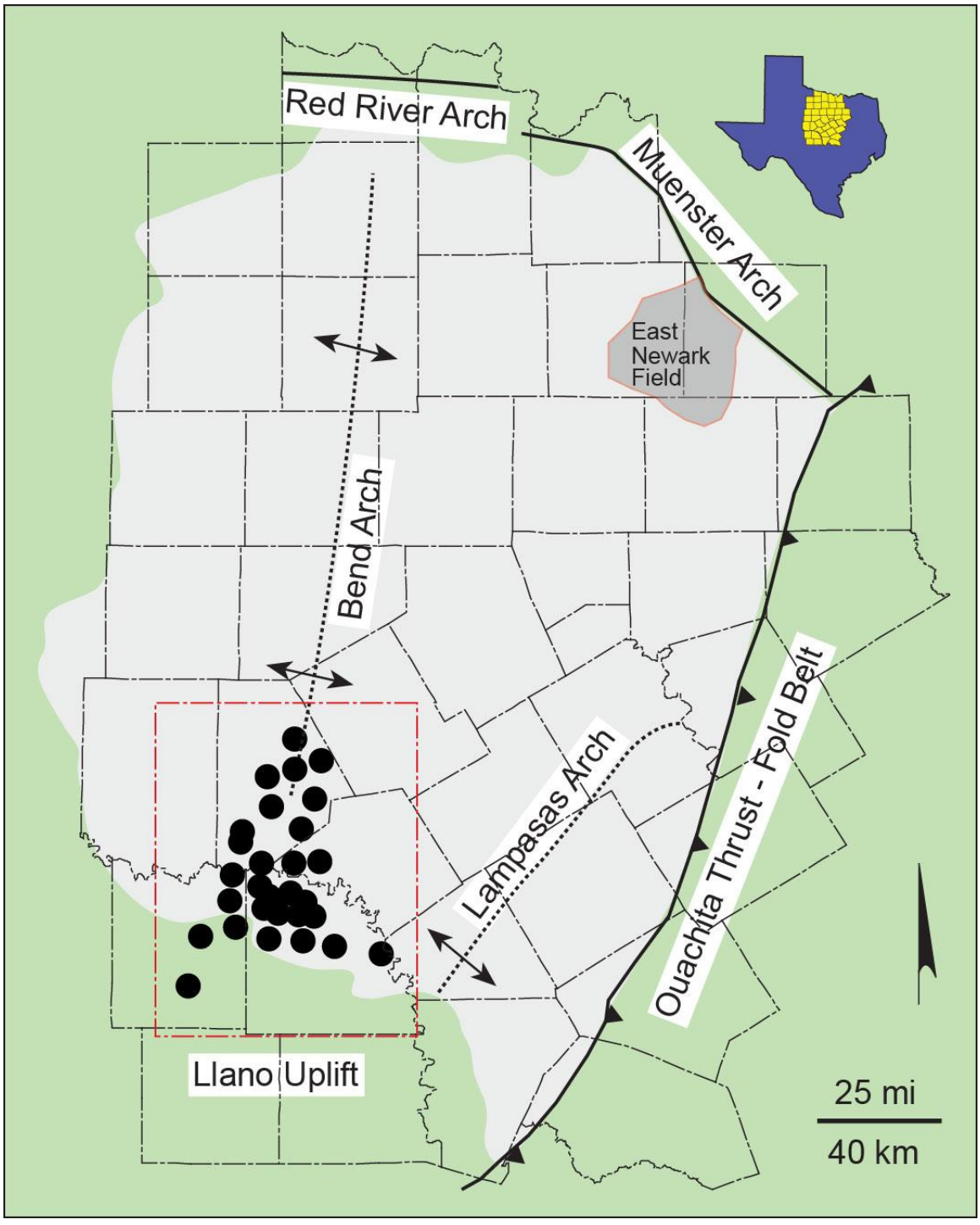
Red River Arch
Muenster Arch
East
Newark
Field
Bend Arch
Lampasas Arch
Ouachita Thrust - Fold Belt
Llano Uplift
25 mi
40 km

Figure 3: Map of the FWB showing the general structural features affecting the basin and the location of the cores used in this study (black circles in red box). Map is modified from Montgomery et al. (2005) and Loucks and Ruppel (2007).

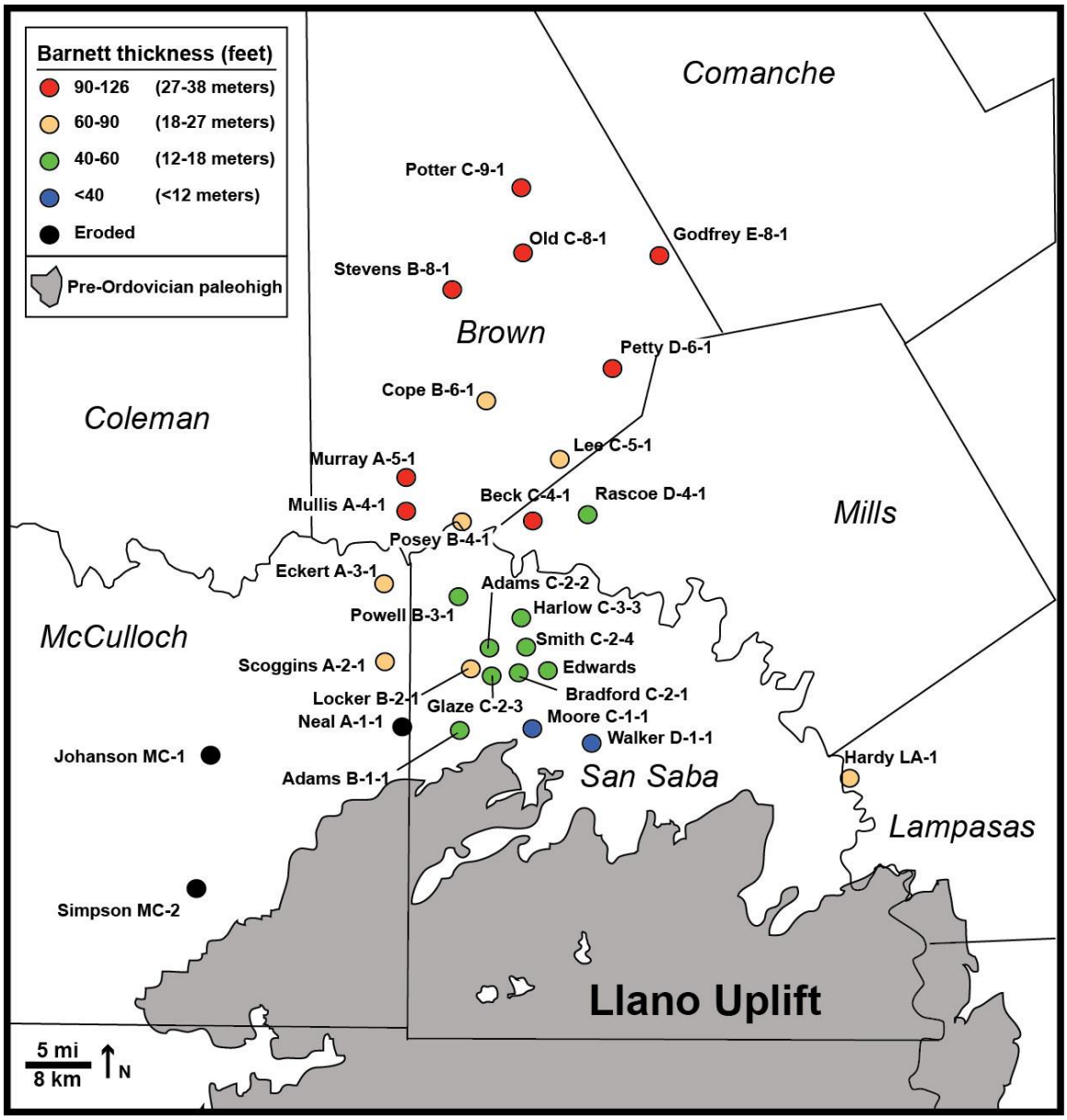

Figure 4: Map showing the distribution of the cores used in this study and the general outline of the Llano Uplift.

Well name	Well code	API	County	Thickness (ft)	Current burial depth (ft)	lower Barnett (ft)	middle Barnett (ft)	upper Barnett (ft)
NEAL^{+o*}	A-1-1	4230730429	MCCULLOCH	0	eroded	-	-	-
JOHANSON^{+xo*}	MC-1	4230730487	MCCULLOCH	0	eroded	-	-	-
SIMPSON	MC-2	4230730488	MCCULLOCH	0	eroded	-	-	-
WALKER^{+o}	D-1-1	4241130100	SAN SABA	37	1259	no core	no core	37
MOORE^{+o}	C-1-1	4241130096	SAN SABA	39	174	-	4	35
ADAMS^{o}	B-1-1	4241130099	SAN SABA	40	93	-	9	31
ADAMS^{o}	C-2-2	4241130107	SAN SABA	42	539	-	7	35
RASCO	D-4-1	4233330195	MILLS	44	1375	-	12	32
EDWARDS	C-2-5	4241130103	SAN SABA	47	545	-	25	22
GLAZE	C-2-3	4241130104	SAN SABA	47	308	-	16	31
SMITH	C-2-4	4241130106	SAN SABA	48	515	-	22	26
HARLOW^{o*}	C-3-3	4241130102	SAN SABA	49	748	-	24	25
BRADFORD	C-2-1	4241130098	SAN SABA	50	696	-	19	31
POWELL^{o}	B-3-1	4241130097	SAN SABA	51	766	-	25	26
SCOGGINS^{+o}	A-2-1	4230730447	MCCULLOCH	61	735	11	21	29
ECKERT	A-3-1	4230730421	MCCULLOCH	78	962	26	19	33
LEE^{x*}	C-5-1	4204931716	BROWN	82	1233	29	18	35
HARDY^{+o}	LA-1	4228130192	LAMPASAS	83	618	25	20	38
LOCKER^{+xo*}	B-2-1	4241130101	SAN SABA	84	555	32	20	32
COPE^{o}	B-6-1	4204931746	BROWN	89	1581	23	24	42
POSEY^{o}*	B-4-1	4204931786	BROWN	89	1077	34	21	34
OLD^{o}	C-8-1	4204931787	BROWN	91	1880	26	29	36
GODFREY^{+xo}	E-8-1	4204931815	BROWN	93	2354	33	19	41
STEVENS^{o}	B-8-1	4204931646	BROWN	100	2047	19	25	56
BECK^{+o*}	C-4-1	4233330194	MILLS	101	1182	41	24	36
POTTER^{+o}	C-9-1	4204931769	BROWN	102	2345	20	24	58
MULLIS^{+o}	A-4-1	4204931813	BROWN	105	1114	46	20	39
MURRAY	A-5-1	4204931745	BROWN	117	1282	50	26	41
PETTY^{+xo*}	D-6-1	4204931785	BROWN	126	1672	51	29	46

Table 1: Core dataset for the Barnett Formation in the southern FWB. The cores are arranged from thinnest to thickest Barnett interval. The Houston Oil and Mineral Co. was the operator for all the cores. Annotations indicate used of the cores in other studies: $^{+}$ used in Reed and Loucks (2015); ^{x} used in Hoelke (2011); ^{o} used in Wood (2013) study; * used for XRD analysis, this study; **Bold** used for XRF analysis, this study.

Loucks and Ruppel (2007) published a depositional model for the Barnett Formation in the northern FWB based on core and thin-section observations as well as wireline logs. They identified three dominant lithofacies: (1) laminated siliceous mudstone, (2) laminated argillaceous lime mudstone, and (3) skeletal, argillaceous lime packstone; and several diagenetic features, including: (1) carbonate concretions, (2) abundant framboidal pyrite, and (3) phosphate grains. The skeletal fragments were interpreted to have been transported into the basin from the adjacent carbonate shelves or upper slopes and the biogenic silica as derived from overlying, oxygenated portions of the water column. In contrast to the high productivity in the photic zone, the bottom waters of the FWB are interpreted to have been euxinic and the basin water mass circulation restricted because of poor connectivity to the open ocean.

Rowe et al. (2008) published a detailed chemostratigraphic study of the Texas United 1 Blakely core from Loucks and Ruppel (2007). The results indicated that the northern FWB was characterized by high-accumulation rates of organic matter, but was sediment starved. The study described the water column as anoxic to euxinic with estimated deep-water renewal times ranging from 8,000 to 20,000 years. Hoelke (2011) expanded the work in the southern FWB using five cores under investigation in the present study (Table 1), and concluded a maximum deep-water renewal time of 1,400 years. The variability between the renewal times estimated from the two datasets (north and south Fort Worth Basin) indicates that the waters in the southern FWB were not as deep or as hydrographically restricted as the waters in the northern FWB.

Reed and Loucks (2015) characterized the organic matter and investigated the pore systems of the low-thermal maturity, organic-rich mudrocks of the southern FWB using 12 cores that are also used in the present study (Table 1). Rock-Eval calculated TOC ranged from 3.08-7.57%, and samples were prepared for scanning electron

microscope (SEM) analysis using broad ion-beam milling with Ar ions. The study found that the ductile kerogen in low-thermal maturity, organic-rich mudrocks occluded the interparticle pores and limited much of the porosity to intraparticle pores, establishing that thermal maturity is an important factor in pore network development in some mudrocks.

Wood (2013) investigated the overlying mixed carbonate-siliciclastic Pennsylvanian Marble Falls Formation using 20 of the cores used in the present study (Figure 1; Table 1). The study investigated the lithofacies and developed a sequence stratigraphic framework, taking into account the Pennsylvanian icehouse climate, sea-level fluctuations, and the inherited FWB substratal topography. Wood (2013) interpreted the initiation of Marble Falls deposition to occur after the termination of the Mississippian sea-level rise and the deposition of the Pennsylvanian phosphatic glauconitic lime packstone condensed interval.

The purpose of the present study is to further develop the geologic framework and the processes that affected the deposition of the Barnett strata in the southern FWB. Specific objectives are to: (1) characterize the Barnett lithofacies, (2) define the depositional setting of each lithofacies and produce a coherent depositional model, (3) identify stacking patterns and correlative surfaces, and (4) suggest a viable sequence stratigraphic interpretation of the succession. It is anticipated that the stratal relationships and interpretations developed here will aid in the assessment of unrecovered hydrocarbon in the Barnett Formation in other areas of the basin.

DATA AND METHODS

The key data for the study are derived from 29 shallow, subsurface cores (Table 1; Figure 4) that completely penetrate the Barnett strata. The cored sites are located north of the Llano Uplift and extend throughout McCullough, Brown, Mills, San Saba, and Lampasas counties of north-central Texas. They were taken during the 1970s by the Houston Oil and Minerals Company and are currently stored at the Bureau of Economic Geology, The University of Texas at Austin. The core based data set provided important insights on to the character and variability of the Barnett strata in the southern Fort Worth Basin. Current burial depths of the cores range from 93 to 2354 ft (28 - 717 m) (Table 1), with depth of burial generally increasing toward the northeast (Figure 4).

CORE AND THIN-SECTION DESCRIPTIONS

Twenty-two core descriptions were generated prior to the study by Dr. Robert Loucks (Bureau of Economic Geology at The University of Texas at Austin). The descriptions were revised when necessary for a more detailed characterization of the strata and the additional seven cores were described by the author in accordance with the methodology outlined in Bebout and Loucks (1984). For naming lithofacies, the Dunham (1962) classification system was used for the carbonate and phosphatic rocks (Trappe, 1998), and the Folk (1980) classification system was used for siliciclastic mudrocks.

Using slabbed cores, the investigation included the identification of sedimentary structures, allochems, and mineralogy. Two-hundred thirty polished thin sections were prepared and examined for rock fabric and texture, biotic content, and mineralogy using a petrographic microscope equipped with a Nikon DS-Ri1 digital camera.

X-RAY POWDER DIFFRACTION

For eight wells (Table 1), a total of 250 fine-powder (<150 μm) samples were collected for bulk mineralogy by x-ray diffraction (XRD) analysis at the Bureau of Economic Geology, The University of Texas at Austin. Each sample (~15 mg) was analyzed from 5°-55° 2θ, for eight minutes with Co-Kα radiation using a Inxitu BTX308 diffractometer. Raw diffraction patterns were semi-quantified using XPowder software and the ICDD PDF 2 database. To quantify the apatite wt% and clay types and abundances, a 26-sample subset was analyzed at K-T Geoservices (Durango, Colorado). The sample preparation was done in accordance to the ASTM Designation: C1365-06 methodology.

ENERGY-DISPERSIVE X-RAY FLUORESCENCE

For eight cores (Table 1), energy-dispersive x-ray fluorescent (XRF) data were collected at a two-inch sampling interval throughout the Barnett strata and several feet into the bounding strata using a Bruker Tracer III handheld XRF unit equipped with an Rh x-ray tube. At each sample location both major and trace element spectra were collected (Table 2). The major element spectra were collected at 15 kV and 34.4 μA, for 60-seconds under a vacuum, and the trace element spectra were collected at 40 kV and 25 μA, for 90-seconds, under ambient conditions. Prior to data acquisition, quality assurance/control pressed powder pellets were scanned six times for 180-seconds in accordance with laboratory methodology. Raw sample spectra were calibrated according to Rowe et al. (2012).

	Elements	
	Major	**Minor**
Energy (Rh x-ray tube)	15 kV 34.4 uA	40 kV 25 uA
Acquisition time	60-sec	90-sec
Filter	-	Al-Ti-Cu
Vacuum	Yes	No
Std. acquisition time	180-sec	180-sec
	Si	**Mo**
	Ca	Zr
	P	Cu
	Ti	Zn
	Fe	Ni
	S	As
	K	Pb
	V	Th
	Mg	Rb
	Mn	Co
	Al	Sr
	Cr	Y
	Na	U
	Ba	Nb
		Ga

Table 2: XRF unit instrument settings for both major and trace elements data acquisition. The corresponding elements in each column indicate which elements are measure by which settings. Major elements concentrations are reported in wt% and trace element concentrations are reported in ppm. **Bolded** elements indicates use in this study.

TOTAL ORGANIC CARBON AND ROCK-EVAL PYROLYSIS

This study utilizes total organic carbon (TOC) data from Hoelke (2011) and Rock-Eval calculated TOC from Reed and Loucks (2015). In Hoelke (2011), after acidifying prepared core samples with 6% H_2SO_3 to remove inorganic carbonates in accordance with Verardo et al. (1990), bulk TOC in wt% was measured using a Costech 4010 elemental analyzer at the University of Texas at Arlington. In Reed and Loucks (2015) Rock-Eval calculated TOC sample depths correspond to SEM sample locations. The samples were analyzed at either Humble Geochemistry or GeoMark Research, Ltd.

GEOLOGIC SETTING

The FWB is a foreland basin that is approximately 200 miles (322 km) in length, 100 miles (161 km) wide in the north, and approximately 10 miles (16 km) wide in the south (Thompson, 1982; Thompson, 1988). It has an asymmetric profile with an overall deepening trend from the southwest to the northeast (Thompson, 1988; Loucks and Ruppel, 2007; Pollastro et al., 2007). It is bounded by the Muenster, Red River, Bend, and Lampasas arches, as well as the Llano Uplift (Figure 3). In areas adjacent to the Muenster Arch the Barnett strata are up to 1000 ft (304 m) thick (Pollastro, 2007), to the south of this area, in Wise County, strata average 550 ft (168 m) thick (Loucks and Ruppel, 2007), and in the southern FWB, adjacent to the Llano Uplift, strata range from 37 to 126 ft (11 to 38 m) thick (this study). In some areas west of the Llano Uplift the Barnett Formation is not present because it was eroded (this study) during falls in sea-level that may have been associated with Pennsylvanian glaciation (e.g. Fielding et al., 2008).

REGIONAL GEOLOGY OF THE FORT WORTH BASIN

From Late Mississippian to Early Pennsylvanian time the Ouachita orogeny deformed Paleozoic strata over 2000 km along the southern extent of the Laurussia craton (Thompson, 1988). During the Mississippian the subduction complex had evolved to a thrust complex and the tectonic stresses from the Ouachita Fold Thrust Front generated the northeast-trending structural elements that influenced deposition in the FWB. As the front progressed westward, the basin downwarped and the depositional axis progressively shifted westward (Walper, 1982; Thompson, 1988; Grayson and Merrill, 1991).

The Llano Uplift, Precambrian in age, was a paleotopographic high in the southern FWB that formed a buttress to the advancement of the Ouachita Fold Thrust

Front limiting subsidence in the area (Figure 3) (Lovick et al., 1982; Grayson and Merrill, 1991; Kier, 1980). To accommodate the compressional forces generated from the Ouachita Fold Thrust Front, horst blocks developed in the southern FWB as it abutted the structurally stable Llano Uplift (Grayson and Merrill, 1991; Erlich and Coleman, 2005). By the early Missourian movement along the faults was interpreted to have stopped (Roepke, 1970).

CLIMATE AND OCEAN CIRCULATION

The early Carboniferous was characterized by a greenhouse climate, and the late Visean has been interpreted as the warmest climate during Mississippian time based on foraminifera species diversity (Reitlinger, 1975). However, recent research demonstrates that several periods of glaciation occurred on Gondwana between the mid-Carboniferous (327 mya) and the early Late Permian (260 mya), each lasting from 1 to 8 million years (Fielding et al., 2008; Gradstein et al., 2012). This climatic variability could have been one cause of fluctuations in the overall second-order sea-level highstand expressed as third-order sequences that persisted throughout Barnett deposition (Figure 1) and also could have affected the sedimentary dynamics in the southern FWB.

Paleogeographic reconstructions by Gutschick and Sandberg (1983) and Blakey (2005) (Figure 2) place the southern FWB adjacent to the shallower water Chappel shelf, to the west, and the Llano Uplift, to the south. Gutschick and Sandberg (1983) estimate water depths on the Chappel Shelf to have been <150 ft (<45.7 m) and water depths on the narrow, rapidly deepening slope adjacent to the FWB to have ranged from <150 to 300 ft (<45.7 to 91.4 m). Adjacent to these environments was the area of Barnett deposition, which Gutschick and Sandberg (1983) estimate to have water depths exceeding 600 ft (183 m). These are their estimates based on anecdotal evidence and

should be revisited. These juxtaposed depositional environments affected sediment variability in the Barnett strata of the southern FWB (Loucks and Ruppel, 2007) and restricted water circulation because of the limited connectivity with the open ocean (Rowe et al., 2008).

STRATIGRAPHIC SETTING AND LITHOFACIES

The present study focuses on the Barnett Formation, with comments provided on the adjacent formations in direct contact with the Barnett strata. In the study region the Barnett Formation is generally bounded by an unconformity of more than 90 m.y. at its base, variably overlying the Whites Crossing, Doublehorn Shale, Ives Breccia, or Ellenburger Group (Figures 1 and 5). The Forestburg limestone, which divides the Barnett strata in the northern FWB into upper and lower units, is absent from the southern FWB (Figure 1). The Barnett Formation is overlain by a very thin (1 to 3 ft; 0.3 to 0.9 m) Pennsylvanian age phosphatic glauconitic lime packstone unit which is overlain by the Pennsylvanian age Marble Falls (Figure 1). The erosion of the Lower Marble Falls Member west of the Llano Uplift was recognized by Erlich and Coleman (2005) and Wood (2013), and the present study recognizes the complete erosion of Barnett strata in the same area (Figure 1).

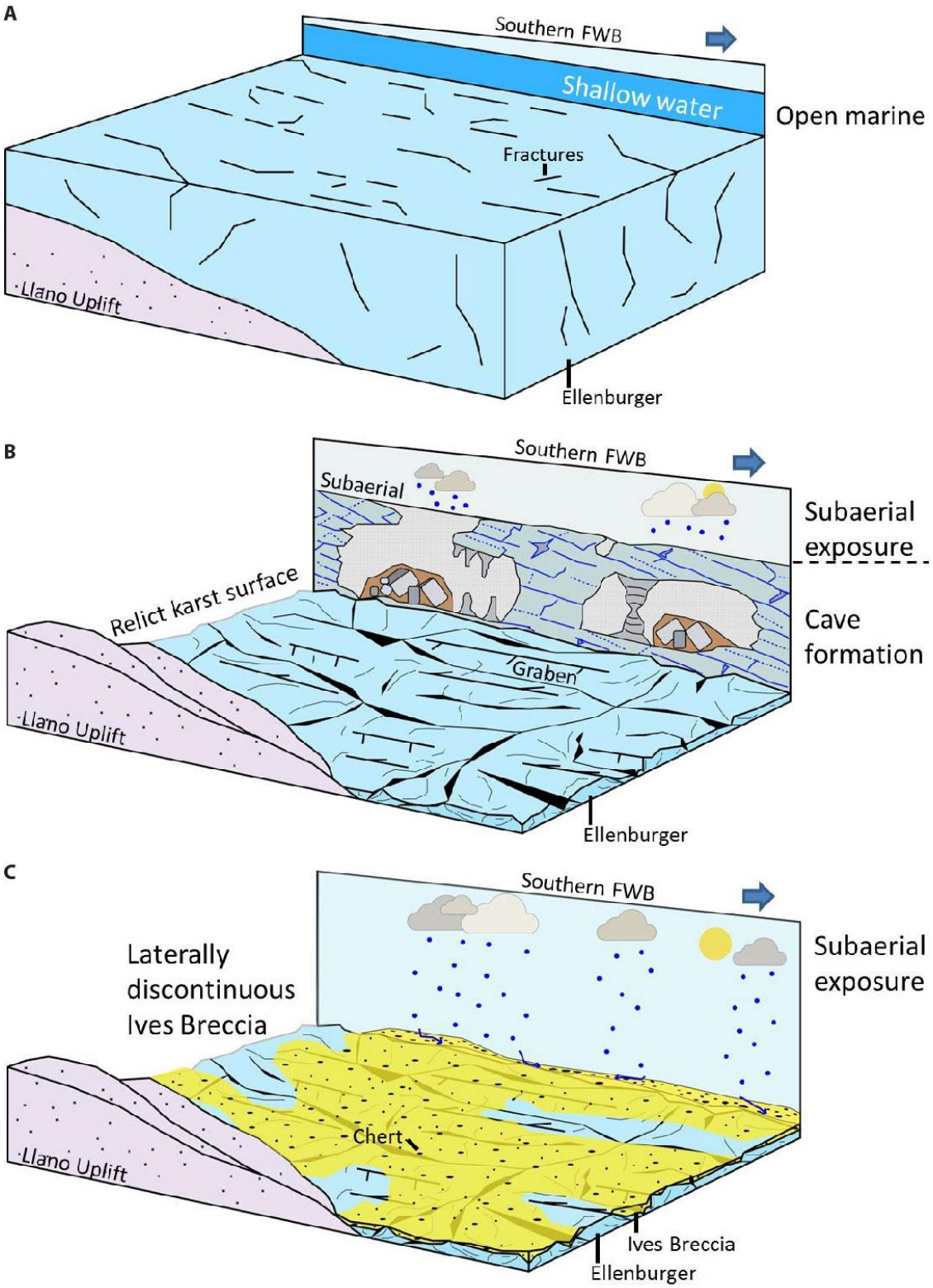
A
Southern FWB
Shallow water
Open marine
Fractures
Llano Uplift
Ellenburger
B
Southern FWB
Subaerial
Subaerial exposure
Relict karst surface
Cave formation
Graben
Llano Uplift
Ellenburger
C
Southern FWB
Laterally discontinuous Ives Breccia
Subaerial exposure
Chert
Llano Uplift
Ives Breccia
Ellenburger

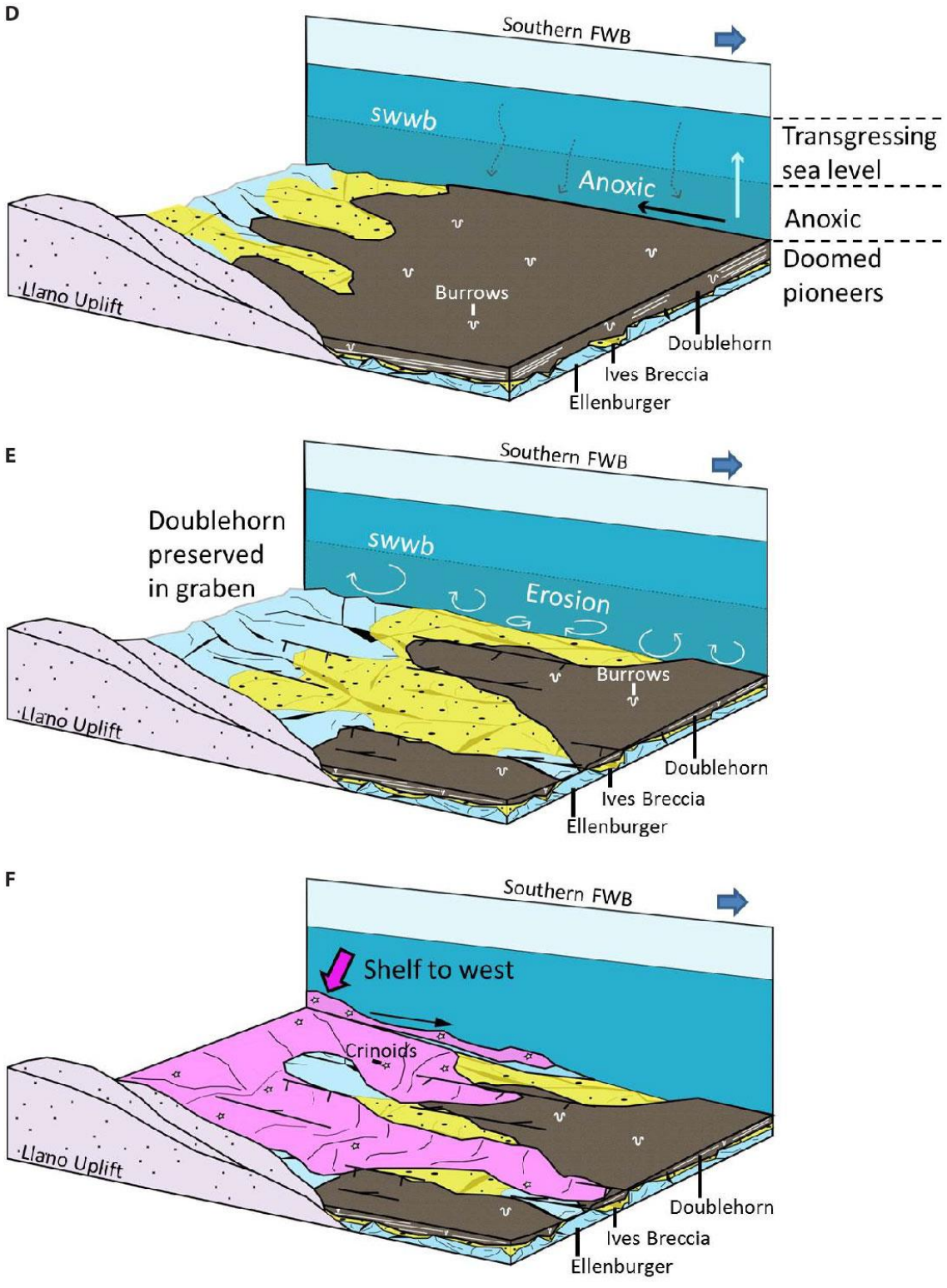
D
Southern FWB
swwb
Anoxic
Transgressing
sea level
Anoxic
Doomed
pioneers
Burrows
Llano Uplift
Doublehorn
Ives Breccia
Ellenburger
E
Southern FWB
Doublehorn
preserved
in graben
swwb
Erosion
Burrows
Llano Uplift
Doublehorn
Ives Breccia
Ellenburger
F
Southern FWB
Shelf to west
Crinoids
Llano Uplift
Doublehorn
Ives Breccia
Ellenburger

Figure 5: Block diagrams showing depositional setting of the preBarnett strata in the southern Fort Worth Basin. (A) Deposition of the Ellenburger Group in an open-marine, shallow-water environment; (B) Karsting of the Ellenburger Group; (C) Development of the Ives Breccia chert and limestone lag deposit over a long-ranging unconformity; (D) Deposition of the Doublehorn Shale during a marine transgression; (E) Erosion of the Doublehorn Shale, preserved in the grabens; (F) Deposition of the Whites Crossing in the graben structures. swwb = storm-weather wave base.

ORDOVICIAN ELLENBURGER GROUP

The Ellenburger Group is a Lower Ordovician carbonate unit (Figure 6) that was deposited in an open-marine, shallow-water environment and was subjected to karsting and cave formation during subaerial exposure related to the Sauk-Tippecanoe unconformity (Morgan, 2012) (Figure 5A-B). The karsting is regionally extensive and is present in most of the cores in the dataset. In a few cores the Ellenburger Group unconformably underlies the Barnett Shale (e.g. Glaze C-2-3), but generally in most cores other units intercede. The dominant Ellenburger Group mineralogies are calcite and dolomite, with in situ chert clasts. The cave fill mineralogy is carbonate clasts and argillaceous carbonate sediment fill with quartz sand grains (Figure 6A-B). Thin section observations include compacted argillaceous clay seams infilling between two clasts, calcite-filled crackle breccia, and euhedral zoned dolomite (Figure 6A-D). These features indicate that the argillaceous infill occurred contemporaneous with clasts deposition. Quartz and feldspar grains are present in the karst fill, but are rare (Figure 5C-D). Common lithofacies include: chaotic breccia with argillaceous sediment fill and fractured and tilted massive blocks (Figure 6E-F).

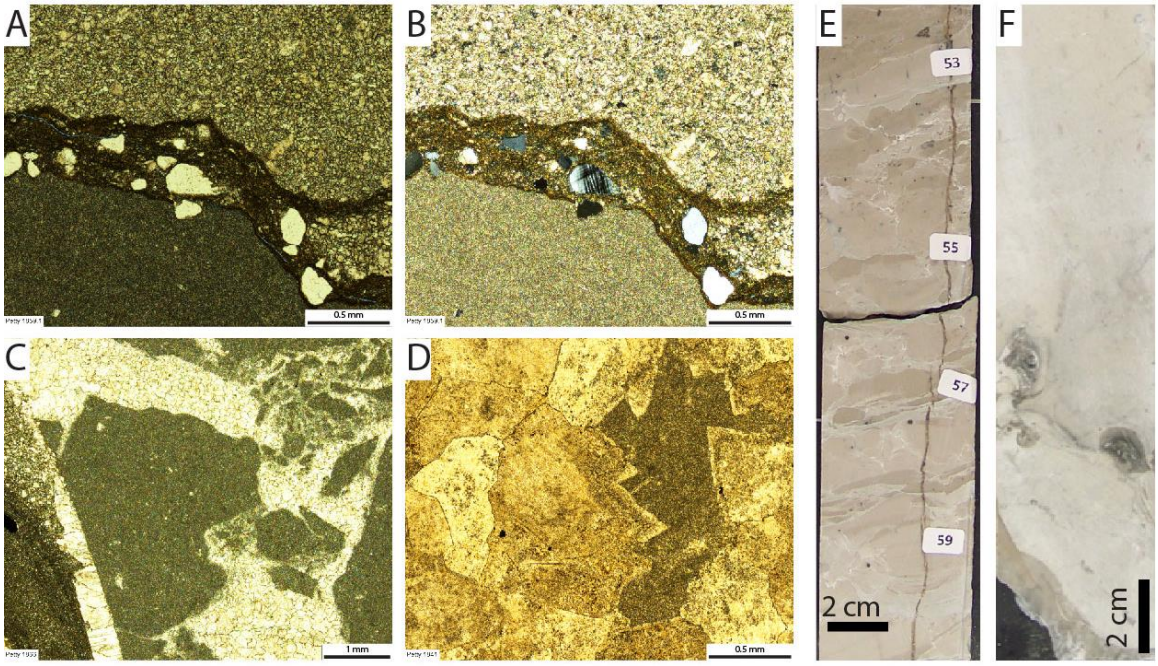

Figure 6: Core and thin section photographs of the Ellenburger Group. (A) Compacted argillaceous clay seam filling between two clasts: Petty D-6-1, 1859.1 ft (566.7 m). (B) Same as A but under cross nicols. (C) Calcite-filled crackle breccia: Petty D-6-1, 1866 ft (568.8 m). (D) Euhedral zoned dolomite with sediment in remaining pore: Petty D-6-1, 1841 ft (561.1 m). (E) Chaotic breccia with argillaceous sediment fill: Harlow C-3-3, 797 ft (242.9 m). (F) Fractured and titled massive block: Beck C-4-1, 1295 ft (394.7 m).

DEVONIAN HOUY FORMATION

The Houy Formation is a Devonian succession composed of the Ives Breccia member (Figure 7A), the Doublehorn Shale member (Figure 7B-O), and other unnamed units (Kier, 1979). The Ives Breccia member is a chert and limestone lag deposit that developed as a regolith from the underlying Ellenburger Group over a long-ranging unconformity (~90 million years) (Figure 5C). The member contains locally derived, eroded chert clasts within a fine-grained calcite matrix (Figure 7A). The member was only observed on top of the Ellenburger Group and was not seen in collapse features, indicating that the karsting and cave infilling was complete by this time. It is laterally discontinuous and occurs as isolated accumulations in wells (e.g. Neal A-1-1, Harlow C-3-3, Beck C-4-1, and Lee C-5-1).

The Doublehorn Shale variably overlies the Ives Breccia and is present in two cores in the dataset (Petty D-6-1 and Posey B-4-1). The member is composed of coarser grains than the Barnett strata and common lithofacies include: dark brown to black, finely-laminated to fissile mudrock facies and burrowed packstone facies, with some grainstone gravity flows punctuating the strata (Figure 7B-D). The dominant mineralogies are calcite, dolomite, quartz, and feldspar grains, with argillaceous material and common fauna including agglutinated foraminifera and *Tasmanites* steinkerns (Figure 7D-G). It has been interpreted by Kier (1972) to be the offshore equivalent to the Ives Breccia (Figure 5D). Erosion removed the member from most of the study area, preserving it only in interpreted graben structures (Figure 5E).

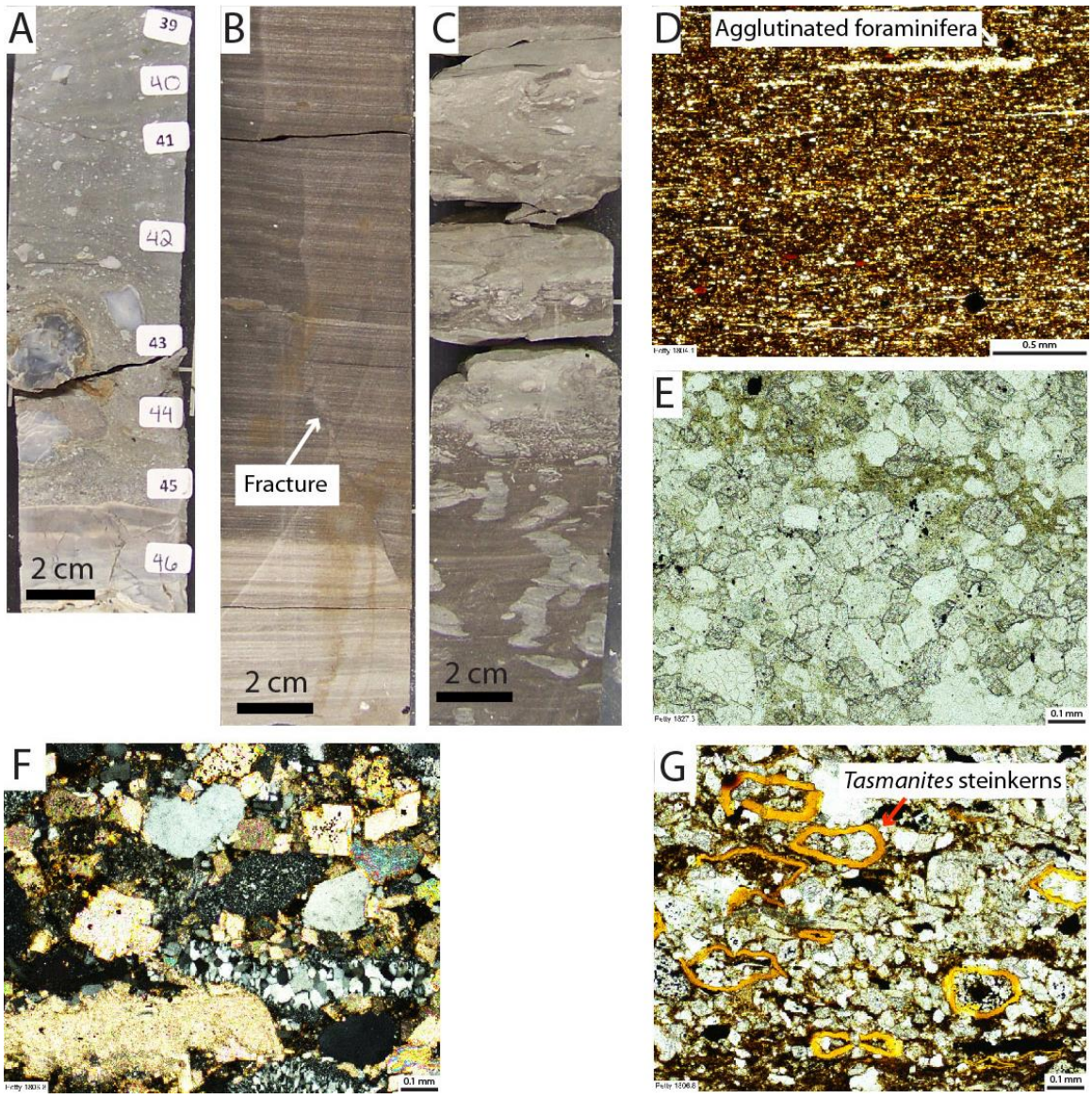
A
39
40
41
42
43
44
45
46
2 cm
B
Fracture
2 cm
C
2 cm
D
Agglutinated foraminifera
0.5 mm
E
0.1 mm
F
0.1 mm
G
Tasmanites steinkerns
0.1 mm

Figure 7: Core and thin section photographs of the Ives Breccia (A) and Doublehorn Shale (B-G). (A) Siliceous cave-sediment fill with eroded chert clasts: Harlow C-3-3, 796 ft (242.6 m). (B) Finely-laminated mudrock showing a tectonic fracturev: Posey B-4-1, 1178 ft (359.1 m). (C) Burrowed packstone facies showing doomed pioneer burrows: Posey B-4-1, 1174 ft (357.8 m). (D) Argillaceous mudrock with compacted agglutinated foraminifera and *Tasmanites* steinkerns with some phosphate grains and pyrite: Petty D-6-1, 1804.1 ft (549.9 m). (E) Fine-sand sized calcite grains and dolomite rhombs: Petty D-6-1, 1827.3 ft (557 m). (F) A variety of coarse- to medium-sand-sized grains including quartz, polycrystalline quartz, calcite grains, and dolomite rhombs under cross nicols: Petty D-6-1, 1806.8 ft (550.7 m). (G) Fine- to medium-sand-sized grains with a higher abundance of argillaceous material and slightly compacted *Tasmanites* steinkerns: Petty D-6-1, 1806.8 ft (550.7 m).

MISSISSIPPIAN WHITES CROSSING

The Whites Crossing is a late Kinderhook to early Osage age (Hass, 1959) crinoid-bearing, fine- to very coarse grained lime rudstone (Figure 8). In core and thin sections the lime rudstone has inclined bedding and is poorly sorted. It is interpreted to be sourced from the Chappel Shelf to the west and transported into the basin *via* gravity flow that preferentially preserved strata in the lows (Figure 5F). The flow is composed of crinoid stems and spines, ostracod fragments, echinoid plates, bryozoans, and rare sponge spicules and trilobites in a micritic matrix (Figure 5R-T). In some cores it unconformably overlies the Ellenburger Group (e.g. Johanson MC-1, Locker B-2-1, and Godfrey E-8-1), unconformably underlies the middle Marble Falls (Simpson MC-2, Johanson MC-1, and Neal A-1-1) and conformably underlies the Barnett Formation (e.g. Locker B-2-1, Beck C-4-1, and Petty D-6-1).

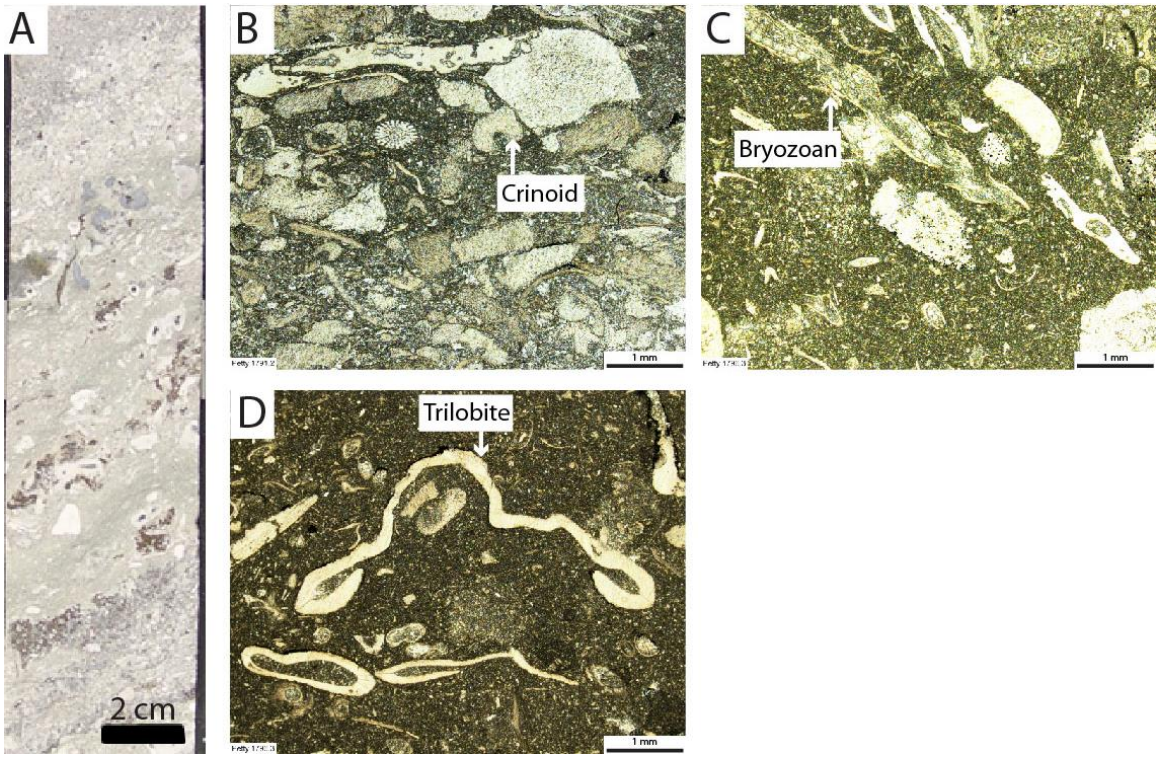

Figure 8: Core and thin section photographs of the Whites Crossing. (A) Very coarse-grained crinoid-bearing limestone: Beck C-4-1, 1280 ft (390.1 m). (B-D) Debris flow composed of crinoid stems and spines, ostracods, echinoid plates, bryozoans, rare sponge spicules, and trilobite fragments in a micritic matrix: (B) Petty D-6-1, 1791 ft (545.9 m); (C-D) 1796.3 ft (547.5 m).

MISSISSIPPIAN BARNETT FORMATION

The Barnett Formation is an Osagean-Chesterian age (Hass, 1953) siliciclastic mudrock that was deposited in the northern FWB over 25 my (Loucks and Ruppel, 2007). Using the core dataset and thin-section observations, four dominate lithofacies were identified as the rock-forming facies of the Barnett Formation in the southern FWB. These include: (1) siliceous mudstone, (2) calcareous siliceous mudstone, (3) skeletal packstone, and (4) phosphatic packstone to grainstone. Facies were further analyzed *via* XRD (Table 3) and XRF analyses. Other notable features in the strata include carbonate concretions and cone-in-cone structures.

	Siliceous mudstone	Calcareous siliceous mudstone	Skeletal packstone	Phosphatic packstone	Phosphatic grainstone	Phosphatic glauconitic lime packstone	Carbonate concretion
Calcite	**9.1**	**22.3**	**41.3**	**16.3**	**36.4**	**35.1**	**93.6**
Dolomite/ ankerite	**2.7**	**8.9**	**2.2**	**0**	**0.7**	**3.6**	**0**
Quartz	**49.2**	**37.0**	**28.0**	**27.4**	**6.4**	**11.6**	**1.5**
Feldspar	**7.6**	**6.4**	**5.4**	**1.3**	**0**	**0**	**0**
Pyrite	**3.8**	**2.5**	**2.3**	**3.1**	**0.6**	**1.9**	**0.5**
Phosphate	**0.7**	**3.2**	**4.6**	**35.7**	**51.1**	**33.6**	**0**
Clays	**27.1**	**19.8**	**16.1**	**15.1**	**4.8**	**14.4**	**4.4**
Illite and mica	14.1	12.0	8.7	8.1	2.7	7.4	4.4
Illite/ smectite	10.3	4.1	5.3	4.9	0	7.0	0
Chlorite	1.9	2.7	1.4	1.1	1.4	0	0
Kaolinite	0.8	1.1	0.7	1.0	0.7	0	0
Total	**100 wt%**	**100 wt%**	**100 wt%**	**99 wt%**	**100 wt%**	**100 wt%**	**100 wt%**

Table 3: XRD mineralogy in wt% from the 26 sample subset analyzed at KT Geoservices (Durango, Colorado).

Siliceous Mudstone

The siliceous mudstone (Figure 9) facies is the most common lithofacies in the Barnett Formation. It is a dark brown color in core (Figure 9A-B) and common components are silt-sized peloids and silt-sized quartz grains, with lesser abundances of silt-sized carbonate grains and argillaceous material. The fabric ranges from nonlaminated to laminated (Figure 9A-D), and postdepositional compaction flattened the peloids and enhanced the laminae, which are emphasized by differential compaction around rigid grains and early diagenetic carbonate concretions (Figure 9B). The facies is rich in organic matter with an average TOC value of 4.5% (Hoelke, 2011; Reed and Loucks, 2015; Appendix A). The organic material is dispersed throughout the argillaceous matrix in the form of compacted peloids, flakes, and particles (Figure 9E-K). The accumulation of organic matter enriched the argillaceous matrix with organic phosphorus and sporadically formed an apatite grain (Figure 9K). The XRD mineral composition for the siliceous mudstone facies (Table 3) is primarily quartz (average 49%, range 43%-59%) with lesser amounts of feldspars, pyrite, and phosphate. Calcite and dolomite average 9% and 3%, respectively (range 0%-15% and 0% - 6%, respectively) and clay minerals make up an average of 27% (range 21%-32%) with decreasing abundances of illite and mica, illite and smectite mixed layer clays, chlorite, and kaolinite.

Thin-section observations reveal that both detrital and biogenic quartz contribute to the total quartz abundance in the form of agglutinated foraminifera (Figure 9E) and sponge spicules (Figure 9F-H), respectively, with differing importance at various stratigraphic intervals within the formation (for details see: Subdivision of the Siliceous Mudstone Facies Using XRF Data). Radiolarians are observed in this facies but are rare (Figure 9G). Burrows are not observed in this facies. Major textural variations of the

lithofacies include broken brachiopod and filibranch mollusk shells (Figure 9H), pyrite framboids (size ranges from <5 um to less than 10 um) (Figure 9J-K), and authigenic phosphate grains (Figure 9I-K).

Phosphate grains are rare in this lithofacies, but when observed occur as isolated grains within the dark, organic-rich matrix (Figure 9J-K). The grains are not well rounded, nor do they exhibit concentric banding as is seen in the phosphatic packstone to grainstone facies. They do not have distinct grain edge boundaries, but instead, the grain boundaries grade into the argillaceous matrix.

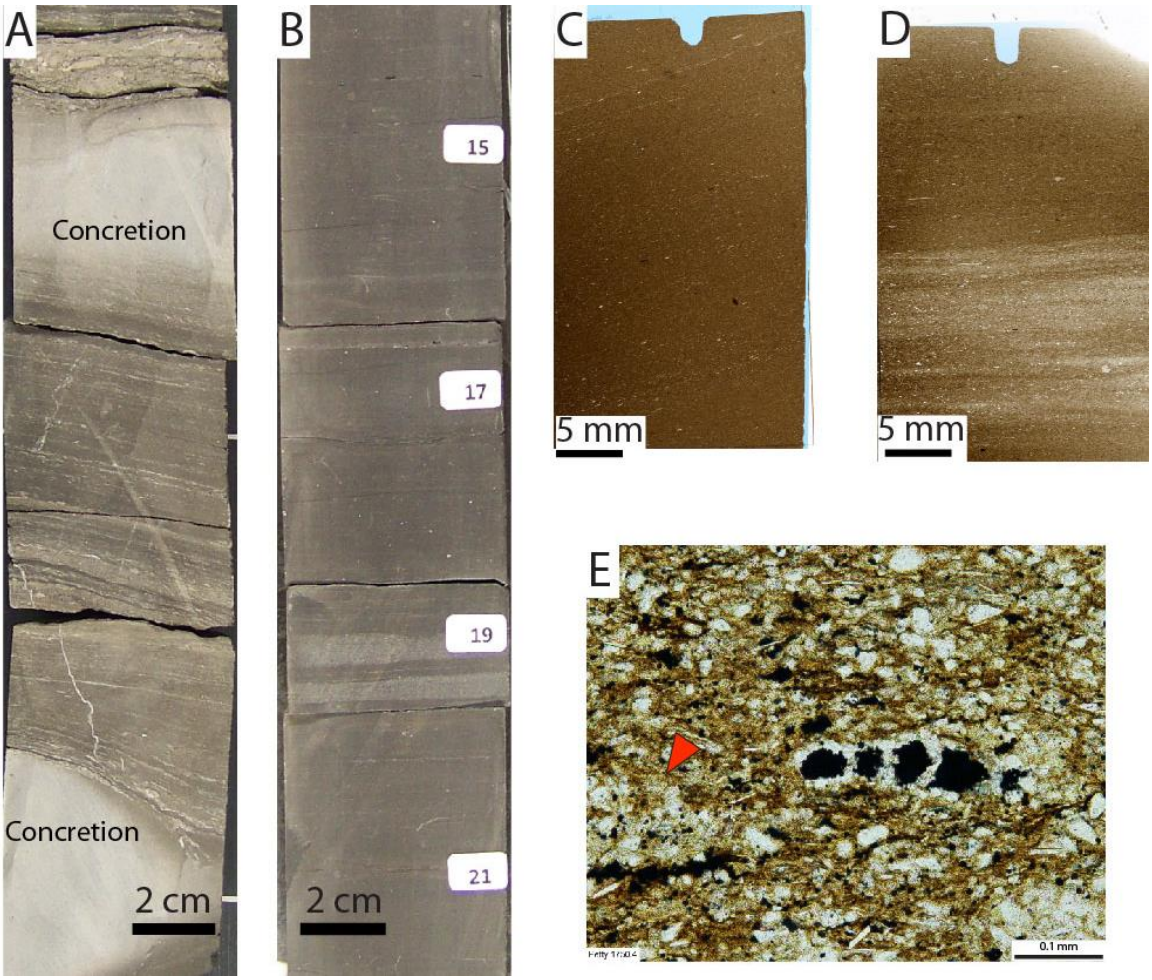
A
Concretion
Concretion
2 cm
B
15
17
19
21
2 cm
C
5 mm
D
5 mm
E
0.1 mm

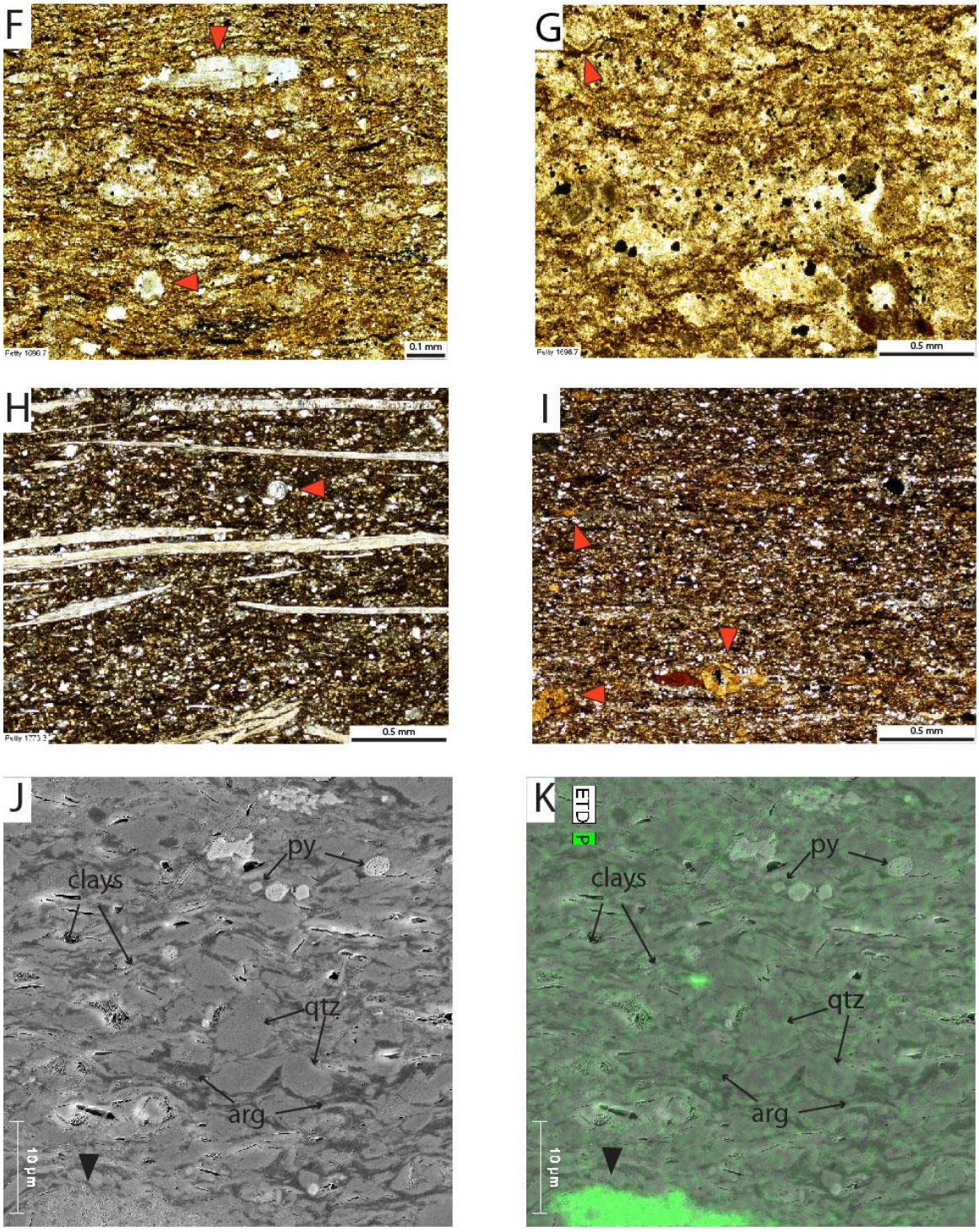
F
0.1 mm
G
0.5 mm
H
0.5 mm
I
0.5 mm
J
py
clays
qtz
arg
10 µm
K
ETD
py
clays
qtz
arg
10 µm

Figure 9: Core and thin-section photographs of the Barnett Formation siliceous mudstone facies. (A) Early carbonate concretions in the siliceous mudstone matrix with phosphatic packstone and skeletal wackestone laminae compacted around the concretion. Glaze C-2-3, 316 ft (96.3 m). (B) Sample showing the uniform color and grain size characteristic of the siliceous mudstone facies. The lighter layers are starved ripples composed of a higher abundance of carbonate silt. Lee C-5-1, 1293 ft (394.1 m). (C) Massive, dark brown argillaceous matrix with little grain-size or grain-type variability. Beck C-4-1, 1209 ft (368.5 m). (D) Starved ripples emphasize the laminated nature of the facies and indicate bottom-water reworking of sediments. Godfrey E-8-1, 2374 ft (723.6 m). (E) An agglutinated foraminifera with pyrite precipitated in the body cavity preserving its original morphology. Extrabasinal, detrital silt-sized quartz grains is common, with some silt-sized skeletal fragments and framboidal pyrite dispersed throughout the argillaceous material. Clusters of silt-sized quartz grains are attributed to foraminifera growth (arrow). Petty D-6-1, 1750.4 ft (533.5 m). (F) Abundant, calcite-replaced, sponge spicules (arrows) within an argillaceous matrix with lacking skeletal fragments and displaying compacted fabric (undulated parallel bedding). Petty D-6-1, 1698.7 ft (517.8 m). (G) A rare radiolarian (arrow) with an abundance of calcite-replaced sponge spicules, and argillaceous material with pyrite framboids dispersed throughout. Petty D-6-1, 1698.7 ft (517.8 m). (H) Broken filibranch mollusk shells aligned into laminae within the siliceous mudstone matrix that also contains calcite-replaced sponge spicules (arrow). Petty D-6-1, 1773.3 ft (540.4 m). (I) In situ authigenic phosphate grains with a mottled internal structure that do not display concentric banding or evidence of sediment reworking (i.e. rounding or grain amalgamation). Locker B-2-1, 597 ft (182 m). (J) An Ar-ion milled, electron backscatter SEM image showing an abundance of silt-size quartz grains (qtz), clays, euhedral and framboidal pyrite (py), and argillaceous material (arg) squeezed between the ridged grains. An in situ, authigenic phosphate grain (arrow) has indistinct grain boundaries with the argillaceous matrix. SEM photo from Luci Tingwei Ko, UT Austin. (K) SEM energy dispersive x-ray image of the same field of view as J, highlighting elemental phosphate dispersed throughout and the in situ phosphate grains.

Calcareous Siliceous Mudstone

Calcareous siliceous mudstone facies (Figure 10) varies from light to dark brown color in core and is composed of a subequal abundance of silt-sized quartz grains and carbonate grains with lesser abundances of silt-sized peloids and argillaceous material. It is characterized by abundant calcite-replaced, and some dolomite-replaced, sponge spicules (Figure 10E-F). The XRD mineral composition (Table 3) averages 37% quartz (range 35%-39%), 22% calcite (range 21% - 24%), and 9% dolomite (7%-11%), clay minerals average 20% (range 14%-26%) with decreasing abundances of illite and mica, illite and smectite mixed layer clays, chlorite, and kaolinite.

The calcareous siliceous mudstone is the only Barnett facies that is weakly bioturbated (Figure 10C-D). The burrows were identified as Nereites ichnofacies, specifically *Cosmorhaphe* and only disturbed a few laminae. A *Cosmorhaphe* burrow is a grazing structure found in fully marine deep-sea environments (Pemberton et al., 2009). Commonly the burrows are infilled by the siliceous mudstone facies (Figure 10D). In the absence of burrowing the fabric ranges from laminated to nonlaminated (Figure 10A-B). The facies also commonly contains fragmented mollusk shells that are dispersed throughout the mudstone matrix and postdepositional compaction has reshaped the peloids and aligned the shells into poorly defined laminae (Figure 10A-B).

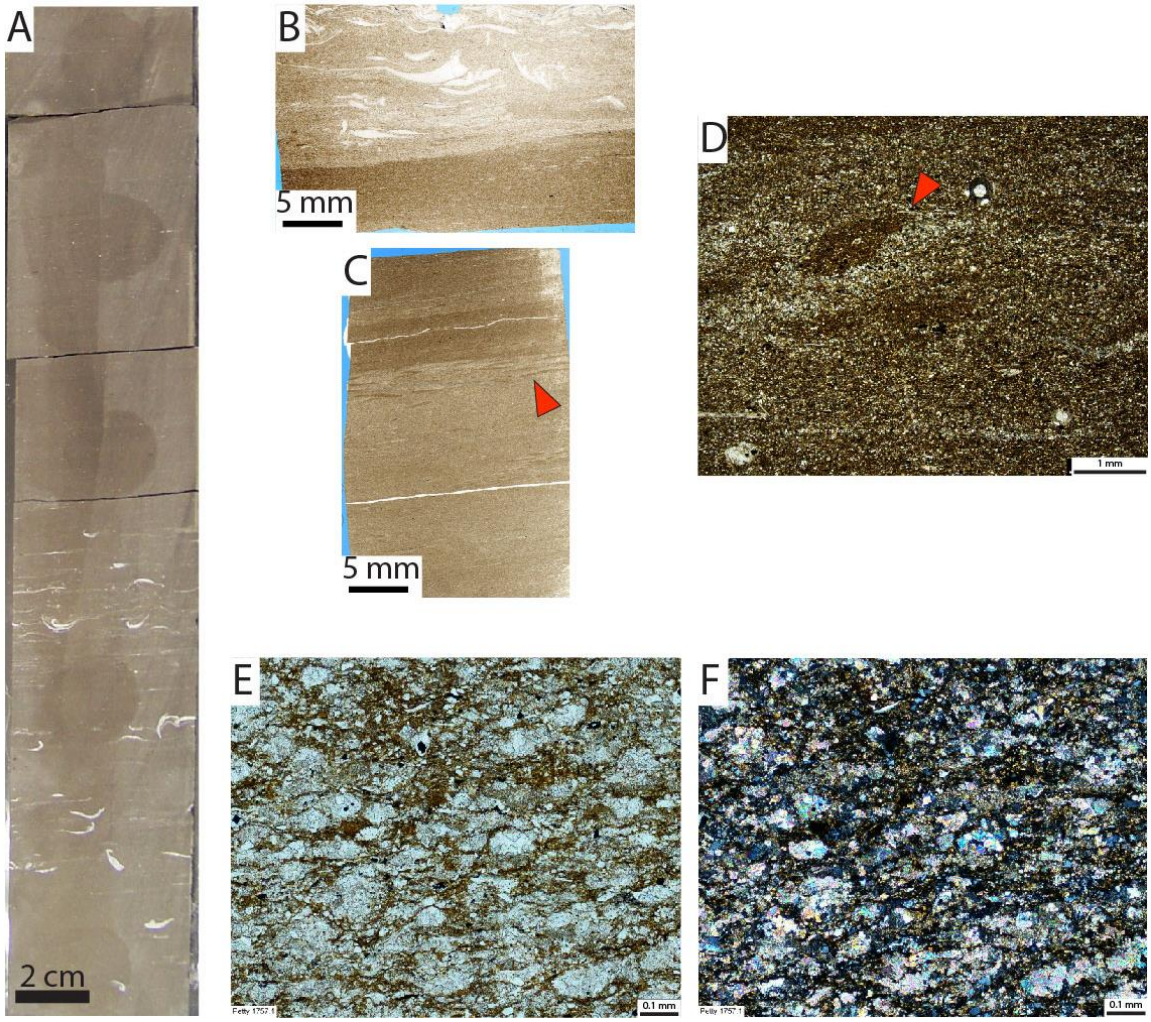

Figure 10: Core and thin-section photographs of the Barnett Formation calcareous siliceous mudstone facies. (A) Core photograph showing the facies variability of the calcareous siliceous mudstone facies with mollusk shells dispersed throughout the matrix at the bottom of the core and no visible features at the top. Posey B-4-1, 1159 ft (353.3 m). (B) Sharp contact between the calcareous siliceous mudstone facies (top) and the siliceous mudstone facies (bottom). Lee C-5-1, 1304.1 ft (397.5 m). (C-D) Weakly bioturbated sediment with siliceous mudstone infilling *Cosmorhaphe* burrows (arrow). Petty D-6-1, 1769 ft (539.2 m); Locker B-2-1, 635 ft (194 m). (E) Abundant calcite-replaced sponge spicules. Petty D-6-1, 1757.1 ft (535.6 m). (F) Same as E but in cross nicols.

Skeletal Packstone

Skeletal packstone facies (Figure 11A) is a light gray color in core and is composed of compacted, broken filibranch mollusk and brachiopod shells within a siliceous mudstone matrix displaying chaotic orientation with a large range in grain size (Figure 11B-E). It could be classified as a sublithofacies of the siliceous mudstone but instead is addressed separately because it is a significant feature in the strata and indicates a distinct sedimentary process that is different than the background sedimentation. . The XRD mineral composition (Table 3) averages 28% quartz (range 18% - 40%), 41% calcite (range 34% - 52%), and 16% clays (range 13% - 20%) with decreasing abundances of illite and mica, illite and smectite mixed layer clays, chlorite, and kaolinite. The facies occurs as millimeter- to centimeter-thick deposits except in sections where multiple flow deposits stack (Figure 11A). The facies contains rare occurrences of subrounded to rounded, fine sand-sized phosphate grains (Figure 11C-E), and in some samples phosphatic intraclasts occur (Figure 11C). Phosphatic ooids are not observed in this facies. Calcite-replaced radiolarians are also observed in this facies but are rare.

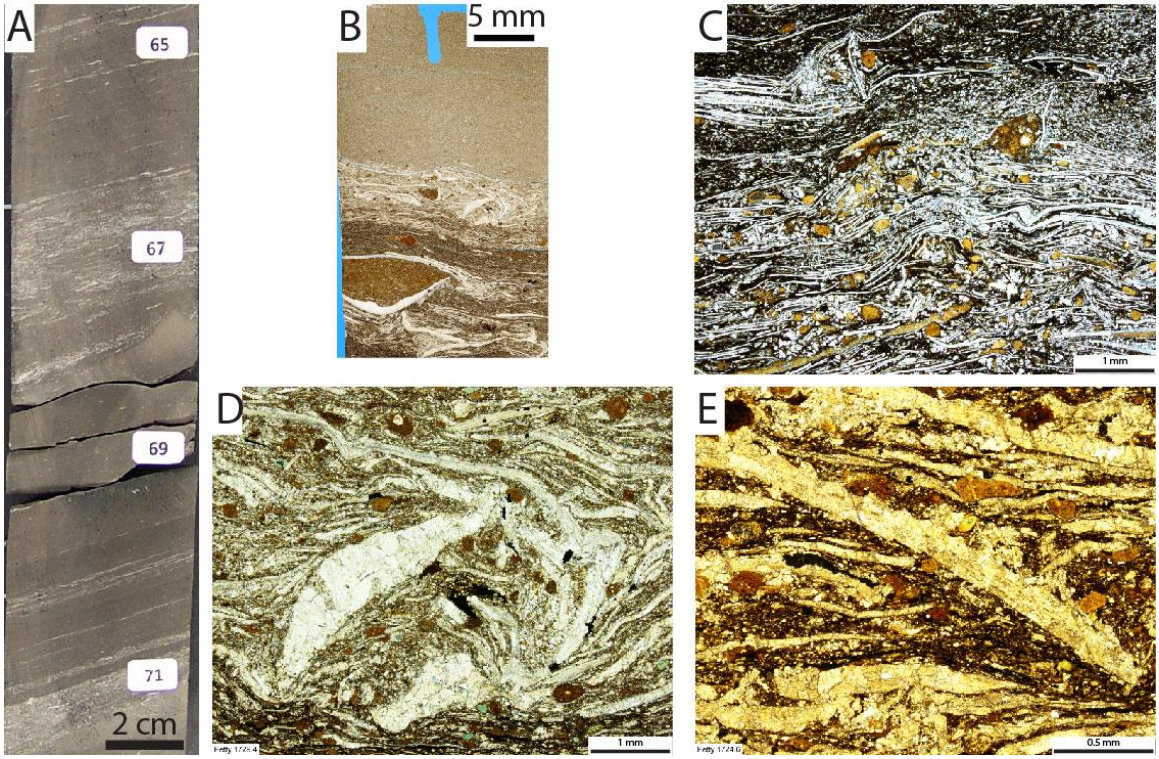

Figure 11: Core and thin-section photographs of the Barnett Formation skeletal packstone facies. (A) Core photograph of the skeletal packstone facies punctuating the siliceous mudstone facies, note the low angle of the deposits. Beck C-4-1, 1224 ft (373.1 m). (B) Shows rapid lithofacies variability with a contact between the calcareous siliceous mudstone facies (top), the skeletal packstone facies (middle and bottom), and a siliceous mudstone facies laminae (lower middle). Petty D-6-1, 1729.4 ft (527.1 m). (C) Fragmented, transported shells with phosphate grain included in the flow. Some calcite-recrystallization of the argillaceous matrix. Locker B-2-1, 590 ft (180 m). (D-E) Broken mollusk shells with chaotic grain orientation and some rounded phosphate grain inclusions and less common occurrences of rounded glauconite grains. Petty D-6-1, 1729.4 ft (527.1 m); Petty D-6-1, 1724.6 ft (525.7 m).

Phosphatic Packstone to Grainstone

Phosphatic packstone to grainstone facies is a tan color in core (Figures 12 and 13) and is composed of well-rounded, very fine sand- to sand-sized phosphatic ooids and grains (Figures 12G-H and 13B-D). The phosphatic packstone facies is characterized by sparse carbonate cements and a low abundance of dark argillaceous material between the phosphatic ooids and grains (Figure 12E-H). The XRD mineral composition of the phosphate packstone facies (Table 3) averages of 36% apatite (range 22%-49%), 27% quartz, 16% calcite, and 15% clays with decreasing abundances of illite and mica, illite and smectite mixed layer, chlorite, and kaolinite. The phosphatic grainstone facies is characterized by blocky carbonate cements and does not contain nonphosphatized shell fragments (Figure 13B-D). The XRD mineral composition (Table 3) averages 51% apatite, 36% calcite, 6% quartz, and 5% clays with decreasing abundances of illite and mica, chlorite, and kaolinite.

The phosphatic ooids and grains that characterize the facies are all well-rounded, with moderate to high sphericity and have distinct grain edge boundaries. They are moderately well-sorted and are generally less than 250 μm in diameter (Figures 12G-H and 13B-D). The phosphatic ooids have one to three concentric rings around a subrounded to rounded phosphate core. The oolitic coatings are primary in origin because the coatings make the grain-to-grain contacts, they are of uniform thickness and continuity, and no relict carbonate minerals or any other minerals are present that would suggest diagenetic replacement with phosphate. The rounded oolitic coatings indicate that the grains have experienced multiple episodes of phosphogenesis. Evidence of soft-sediment deformation is illustrated by offset of phosphate grain laminae (Figure 12C-D).

Nonphosphatized, broken mollusk shells are sporadically observed in association with the packstone facies and can serve as a nucleation site for a phosphate ooid or grain

(Figure 12G); other fossils, such as crinoids, cephalopods, gastropods, and foraminfera are observed as the nucleus, but are rare. Most commonly the phosphatic ooids and grains have an internally structureless phosphatic core. Modern phosphate accumulations are strongly coupled with bacterial biogeochemical cycling of phosphorus (Schulz and Schulz, 2005; Goldhammer et al., 2010) and the studies that have evaluated internally structureless phosphate grains attributed their nucleation sites to microbes, including: fungi, bacteria, and cyanobacteria (e.g. Dahanayake and Krumbein, 1986; Schulz and Schulz, 2005; Bailey et al., 2007).

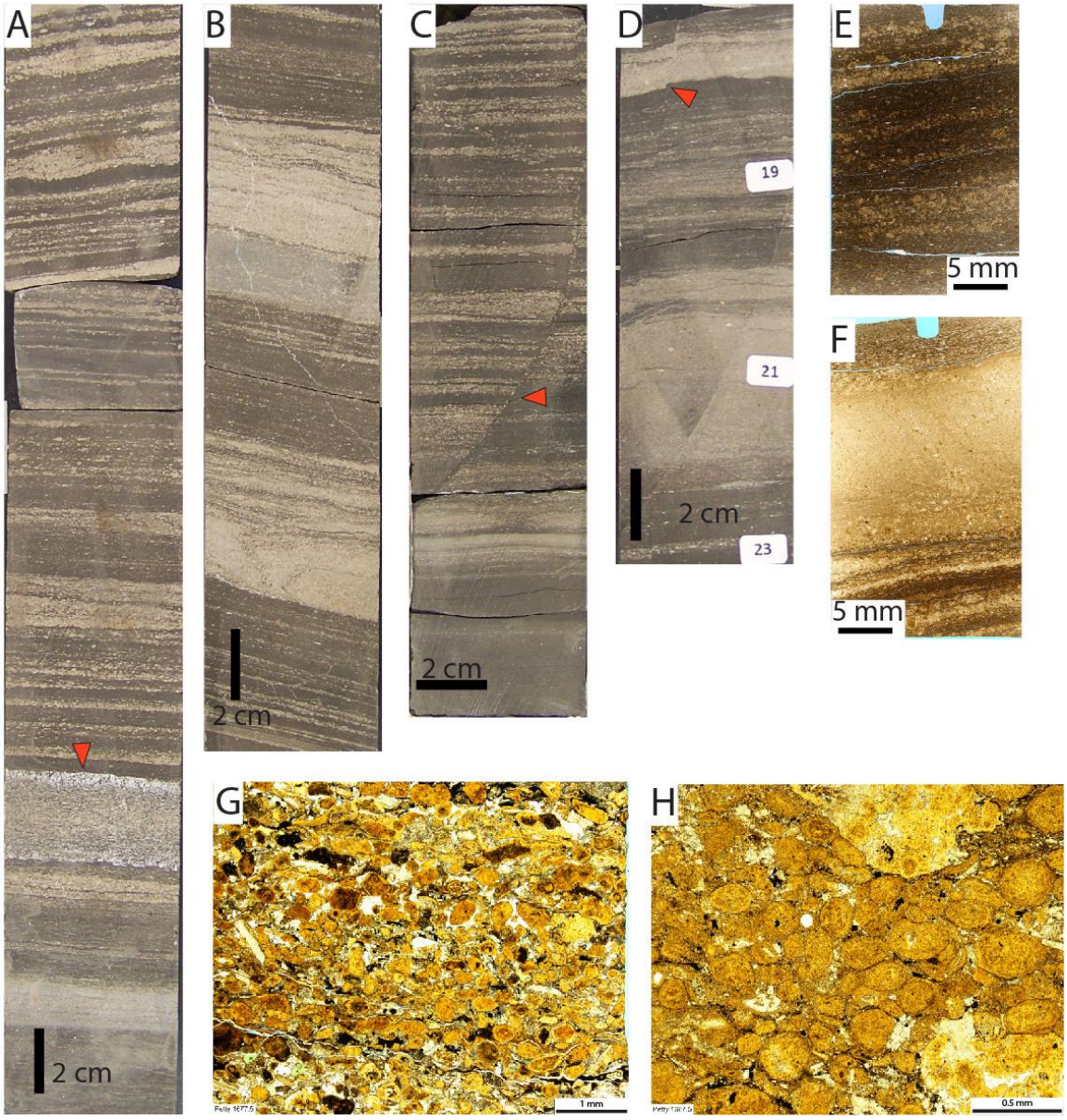
A
2 cm
B
2 cm
C
2 cm
D
19
21
2 cm
23
E
5 mm
F
5 mm
G
1 mm
H
0.5 mm

Figure 12: Core and thin-section photographs of the Barnett Formation phosphatic packstone facies. (A-D) Core photos of rapid alteration of the phosphatic packstone facies with the siliceous mudstone facies, cone-in-cone structures, and soft-sediment deformation (arrow); Glaze C-2-3, 318 ft (96.9 m); Glaze C-2-3, 351 ft (107 m); Smith C-2-4, 552 ft (168 m); Harlow C-3-3, 785 ft (239 m);. (E-F) Thin section scans showing phosphatic packstone and siliceous mudstone facies alternations with scoured contacts; Harlow C-3-3, 774 ft (236 m); Petty D-6-1, 1714.7 ft (522.6 m). (G-H) Condensed deposit showing well rounded phosphatic grains and ooids; Petty D-6-1, 1677.5 ft (511.3 m); Petty D-6-1, 1687.5 ft (514.4 m).

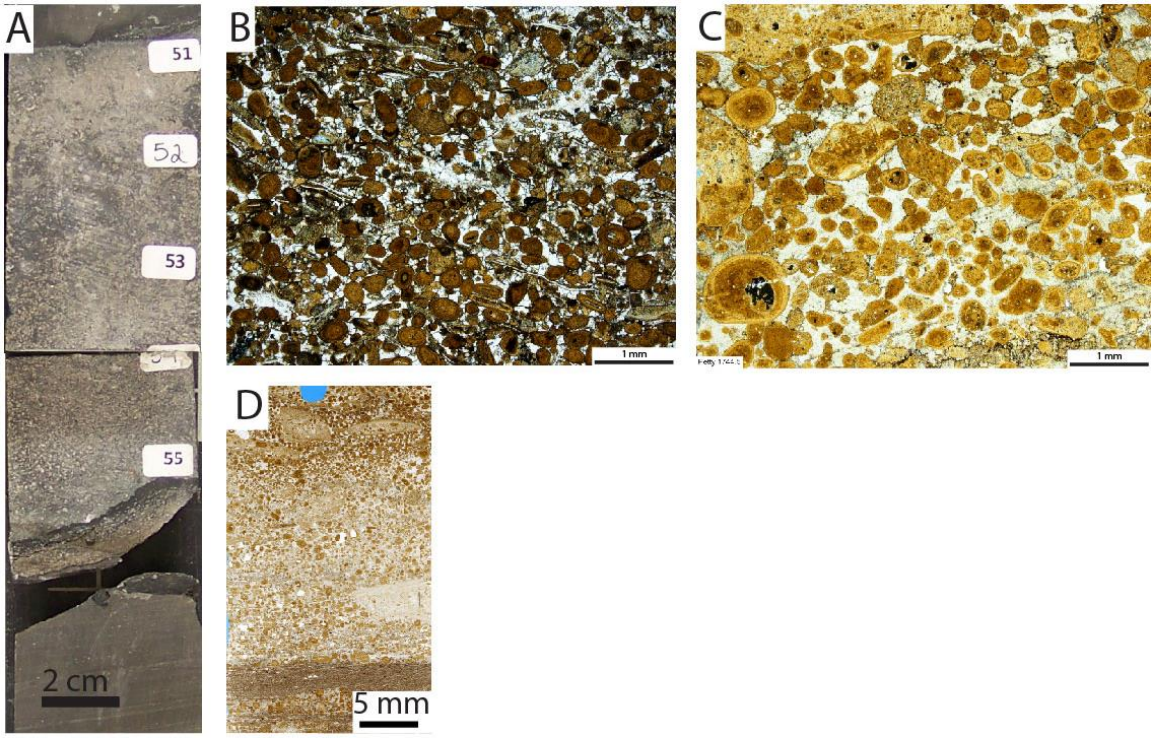

Figure 13: Core and thin-section photographs of the Barnett Formation phosphatic grainstone facies. (A) Phosphatic grainstone present at the top of the Harlow C-3-3, 748 ft (228 m) in the absence of the phosphatic glauconitic lime packstone facies. (B-D) Phosphatic grainstone facies with well-rounded phosphate grains and ooids with carbonate cements; Locker B-2-1, 590 ft (180 m); Petty D-6-1, 1744.5 ft (531.7 m); Petty D-6-1, 1744.5 ft (531.7 m).

Associated Diagenetic Features

Two other common diagenetic features observed throughout the Barnett strata are carbonate concretions (Figures 9A and 14A-B) and bedding-parallel fibrous calcite beef veins exhibiting cone-in-cone structures (Figures 12A and 14C-F).

Carbonate Concretions

Carbonate concretions (Figure 9A) are interpreted early diagenetic features that form in the upper few centimeters of the sediment-water interface under sulfidic, reducing conditions, with low sedimentation rates (e.g. Folk and Land, 1975; Coleman et al., 1993). In core they range in vertical thickness from 1 to 3 inches (2.54 to 7.62 cm) and most commonly occur in the upper portions of the Barnett strata. In thin sections the features display uncompacted fabric and have pyrite dispersed throughout (Figure 14A-B). They are commonly fractured, especially in cores near the Llano uplift, which may be related to fault movement. The XRD mineral composition, Table 3, averages 94% calcite, 2% quartz, 4% illite, and mica clay minerals 20%.

Cone-in-Cone Structures

The bedding-parallel fibrous calcite beef veins exhibiting cone-in-cone structures are nucleated on thin-walled pelecypods (Figure 14C-F), visible as the central suture line, with radial growth perpendicular to the shell fragment. They are generally between 250 μm – 2 mm in length and are found in close stratigraphic association with the phosphatic packstone to grainstone facies (Figures 12A).

Cobbold et al. (2013) compiled a worldwide catalogue of beef and cone-in-cone occurrences and noted that they are most commonly found within marine shale. It is a very common feature in the Vaca Muerta Formation (e.g. Parnell et al., 2000; Rodrigues

et al., 2009), and have been interpreted by Rodrigues et al. (2009) to be a product of differential shear. Rodrigues (2008) used carbon and oxygen isotopes and fluid inclusion work to show that these are late diagenetic features linked to high overpressures and hydrocarbon generation.

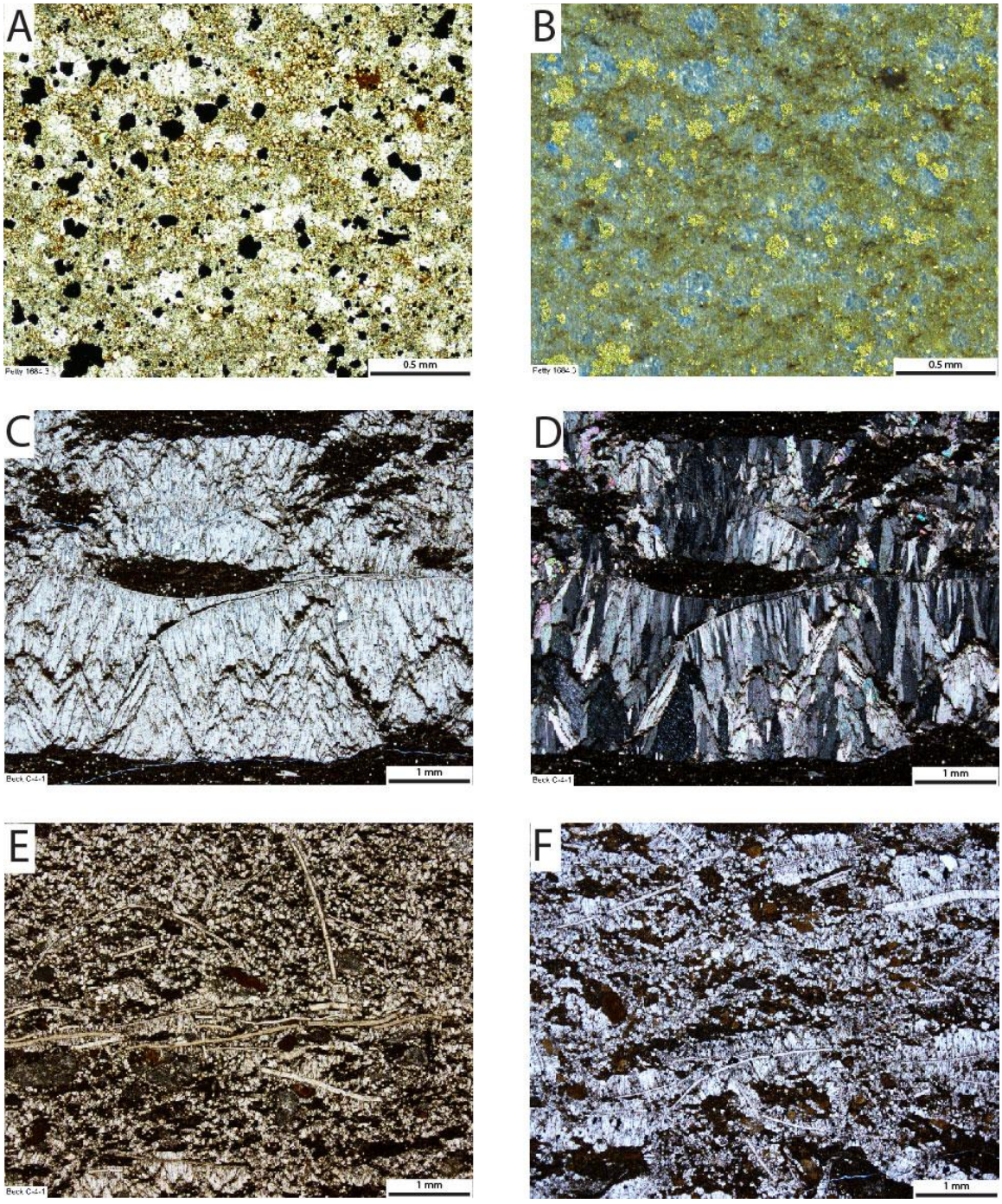
A
0.5 mm
B
0.5 mm
C
1 mm
D
1 mm
E
1 mm
F
1 mm

Figure 14: Thin-section photographs of the associated diagenetic features of the Barnett Formation. (A-B) Carbonate concretion showing uncompacted fabric and pyrite framboids; Petty D-6-1, 1684.3 ft (513.4 m) under plane light and reflected light, respectively. (C-E) Bedding-parallel fibrous calcite beef veins exhibiting cone-in-cone structures are nucleated on thin-walled pelecypods and recrystallization of the argillaceous matrix; Beck C-4-1, 1200 ft (365.8 m). (F) Phosphate grains found in association with the cone-in-cone structures; Locker B-2-1, 575 ft (175 m).

PENNSYLVANIAN PHOSPHATIC GLAUCONITIC LIME PACKSTONE

The phosphatic glauconitic lime packstone facies (Figure 15) is a Chesterian to Morrowan age (Liner et al., 1978) unit that occurs throughout the southern FWB after the deposition of the Mississippian Barnett Formation and before the deposition of the Pennsylvanian Marble Falls Formation. It ranges in thickness from 1 to 3 ft (0.3 to 0.9 m) across the study area and is pronounced in cores both proximal and distal to the Llano Uplift. It is composed of a subequal abundance of well-rounded, fine- to medium-sand-sized glauconite grains, phosphatic ooids, and intraclasts with common chert grains in a dark argillaceous matrix (Figure 15A-F). The high abundance of glauconite grains gives the facies a characteristic blue-green color in core (Figure 15G). The XRD mineral composition (Table 3) averages 34% apatite (range 23%-44%), 12% quartz (range 9%-15%), 35% calcite (range 25%-45%), and 14% clays with decreasing abundances of illite and mica, and illite and smectite mixed layer clays.

The facies is characterized by convoluted bedding and is weakly bioturbated (Figure 15G). Fish bone fragments (Figure 15C) are observed in the facies and contribute to its phosphate abundance. Some occurrences of glauconite overgrowths on phosphate grains and conversely phosphatic overgrowths on glauconite grains are documented (Figure 15C-D). Chert and sponge spicules are common, however, fossil fragments, such as brachiopods and bivalves, crinoids, echinoids, cephalopods, gastropods, and *Endothyra* foraminifera, are observed but are rare (Figure 15A-F).

The unit has a scoured basal contact with the siliceous mudstone or phosphatic packstone facies of the Barnett Formation (Figure 15G) and a gradational upper contact (Figure 15H-I) with the Marble Falls Formation. The gradational upper contact is

characterized by an increase in carbonate content, a corresponding increase of argillaceous matrix as well an increase in sponge spicule abundance, and a decrease in the phosphatic and glauconite grain abundances (Figure 15H-I). Thus the unit is interpreted to have an unconformable contact with the Mississippian Barnett Formation and a conformable contact with the Pennsylvanian Marble Falls.

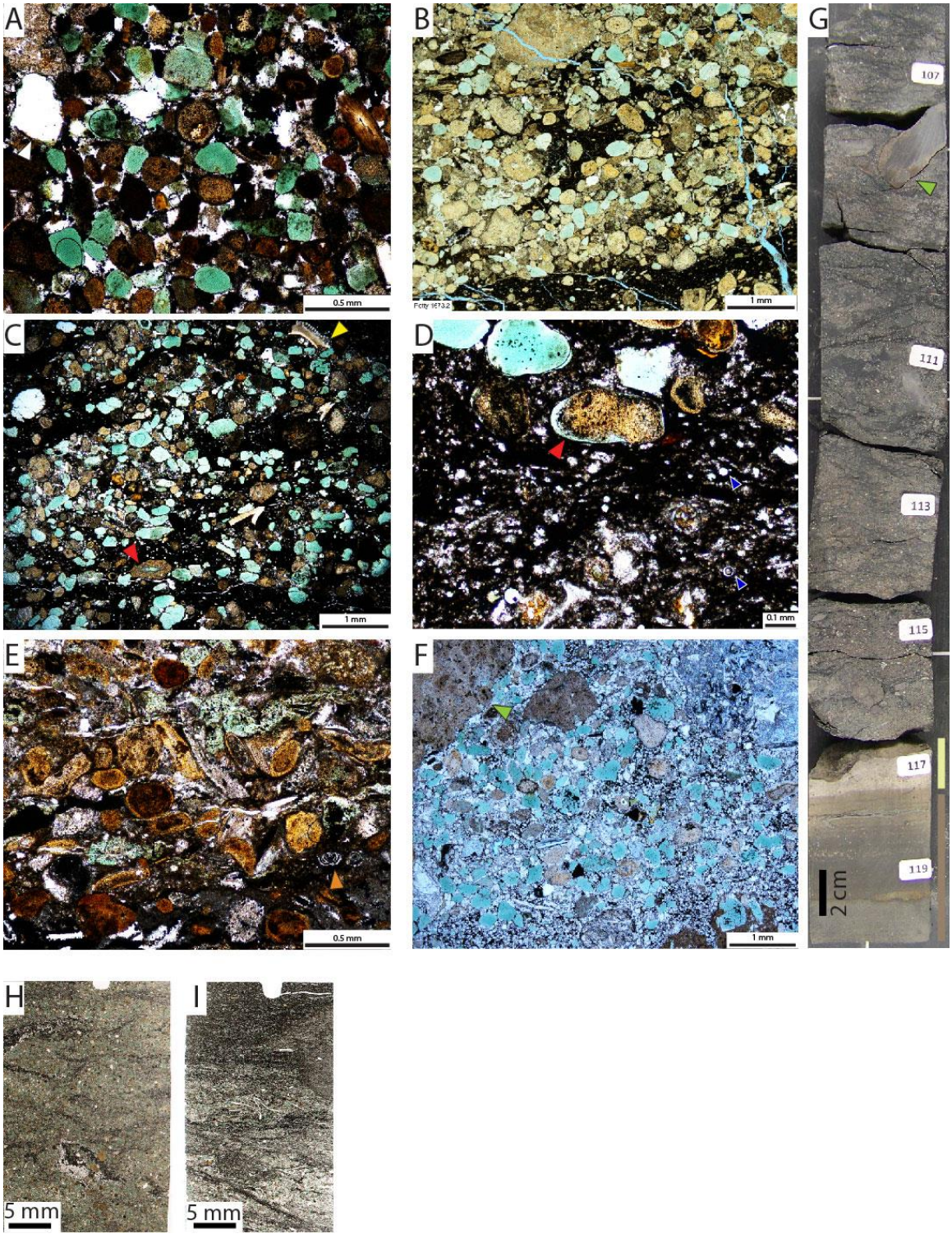
A
0.5 mm
B
1 mm
G
107
111
113
115
117
119
2 cm
C
1 mm
D
0.1 mm
E
0.5 mm
F
1 mm
H
5 mm
I
5 mm

Figure 15: Core and thin-section photographs of the Pennsylvanian phosphatic glauconitic lime packstone facies. There are an abundance of well-rounded, fine- to medium-sand-sized glauconite grains and phosphatic grains and ooids. (A) Subequal mixture of phosphate (dark brown to black) and glauconite (green) grains with chert (white arrow). Godfrey E-8-1, 2353.5 ft (717.3 m). (B) Packstone fabric with a dark argillaceous seam. Fractures shown are an artifact. Petty D-6-1, 1673.2 ft (509.9 m). (C) Phosphatic overgrowth on a glauconite grain (red arrow). Bone fragment (yellow arrow). Petty D-6-1, 1672.5 (509.8 m). (D) A glauconite overgrowth on a phosphate grain (red arrow). Abundant sponge spicules in the dark argillaceous matrix. Petty D-6-1, 1672.5 (509.8 m). (E) Higher abundance of skeletal fragments with *Endothyra* foraminifera (orange arrow). Lee C-5-1, 1233.8 ft (376.1 m). (F) Argillaceous matrix, similar to the matrix found in association with the bedding parallel fibrous calcite beef veins. Abundant skeletal fragments and a phosphatic intraclasts (green arrow). Locker B-2-1, 554 ft (168 m). (G) Core photograph showing convoluted bedding, large intraclasts (green arrow), and a sharp erosional lower contact with the Barnett strata, specifically a remnant of the isolated phosphatic grainstone flow deposit (cream colored bar) and then the siliceous mudstone facies (brown colored bar) below. Lee C-5-1, 1233 ft (375.8 m). (H-I) Thin-section scans showing a gradational contact with the overlying Marble Falls burrowed sponge spicule packstone facies, as defined by Wood (2013). Beck C-4-1, 1182.7 ft (360.5 m); Beck C-4-1, 1181.7 ft (360.2 m).

PENNSYLVANIAN MARBLE FALLS

The Marble Falls Formation is a Morrowan to Atokan age (Manger and Sutherland, 1984; Groves, 1991) mixed carbonate-siliciclastic unit that is formally subdivided into the Lower Marble Falls Member (Morrowan stage) and the Upper Marble Falls Member (Atokan stage) based on fusulinid biostratigraphy (Groves, 1991). Its facies were deposited in the southern FWB on a platform setting, with facies tract geometry controlled by both subsidence and second-order sea-level changes, and with sequence development and unconformities controlled by third-order sea-level change (Erlich and Coleman, 2005).

Wood (2013) analyzed 20 of the cores used in the present study (Table 1) to subdivide the Marble Falls into 3 depositional sequences: lower, middle, and upper Marble Falls. The lower Marble Falls is time equivalent to the Lower Marble Falls Member and the beginning deposition of the middle Marble Falls is time equivalent to the beginning deposition of the Middle Marble Falls Member (Erlich and Coleman, 2005; Wood, 2013). Wood (2013) interprets the lower Marble Falls to be an aggradational ramp deposit with deposition terminated by a major sea-level fall, the middle Marble Falls to be deposited after a sea-level lowstand followed by a marine transgression, and the upper Marble falls deposition to be influenced by increased accommodation space related to tectonic subsidence. Both Erlich and Coleman (2005) and Wood (2013) recognized the erosion of Lower Marble Falls Member strata to the west of the Llano Uplift and interpreted this to be related to a glacio-eustatic sea-level lowstand subsequent to the deposition of the Lower Marble Falls Member and prior to the deposition of the Middle Marble Falls Member (e.g. Johanson MC-1 and Neal A-1-1, (Wood, 2013), and Simpson MC-2 (present study)).

REGIONAL STRATIGRAPHIC VARIABILITY

The analysis of both lateral and vertical Barnett lithofacies distribution helps to identify depositional trends characteristic of Barnett strata. In the southern FWB specific stratigraphic intervals of phosphatic packstone facies abruptly alternate with the siliceous mudstone facies at the centimeter scale over several vertical feet (less than one meter) (Figure 12A-D; Figures 16 and 17), and outside of these intervals the phosphatic packstone facies is much less likely to occur. The intervals are separated by much thicker deposits (>3 meters) of the siliceous mudstone facies which is punctuated by laminated occurrences of the skeletal packstone facies. The incorporation of XRF curves revealed that the phosphatic packstone intervals and the phosphatic glauconitic lime packstone unit align with notable changes in the trend of the clay proxy curves (e.g. Ti) (Figures 16 and 17). The tops of the phosphatic packstone facies at these localities and the top of the phosphatic glauconitic lime packstone unit were thus used to subdivide the Barnett strata into lower, middle, and upper units (Figure 1).

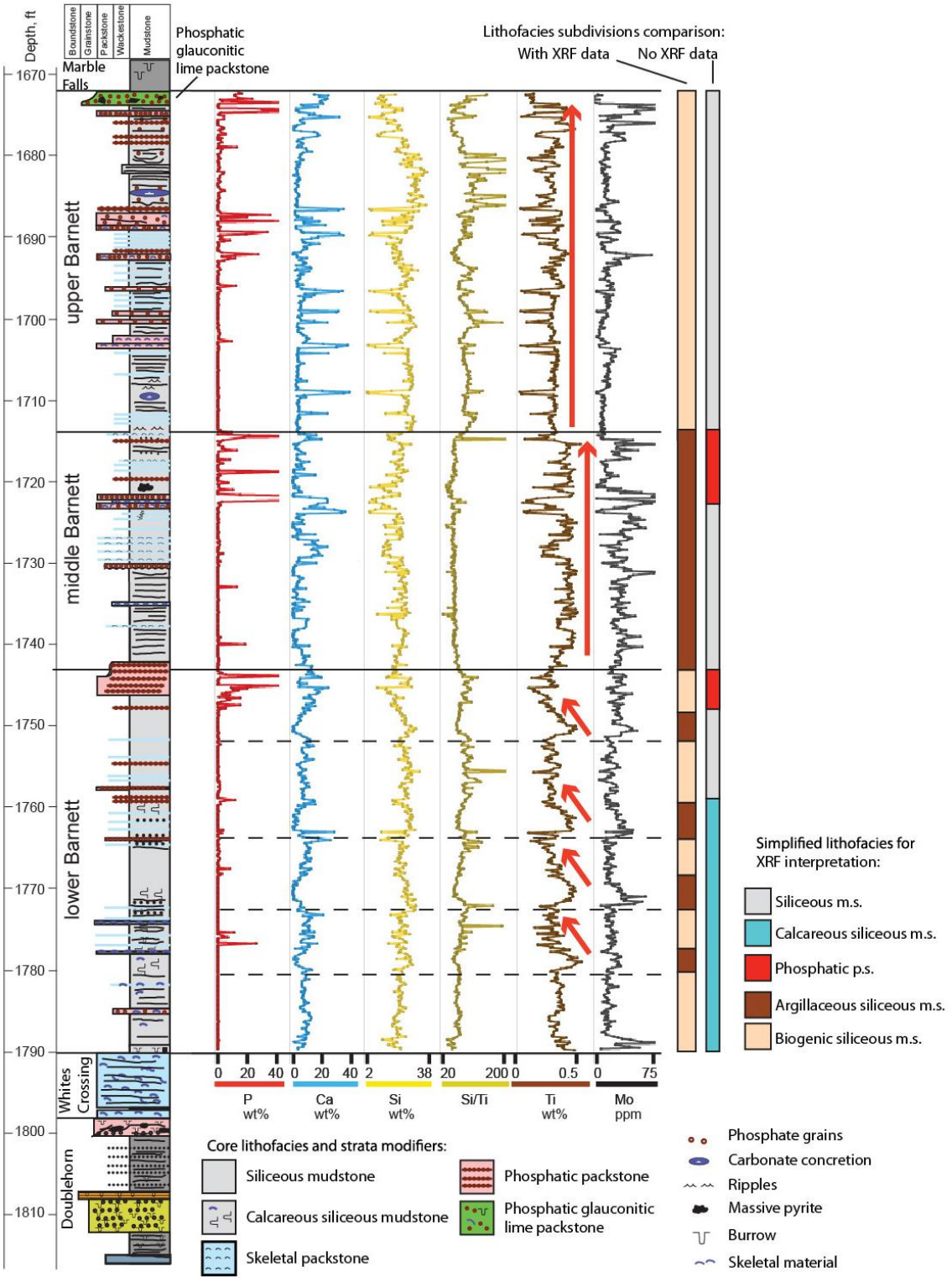
Depth, ft
Boundstone
Grainstone
Packstone
Wackestone
Mudstone
Marble Falls
Phosphatic glauconitic lime packstone
Lithofacies subdivisions comparison:
With XRF data
No XRF data
upper Barnett
middle Barnett
lower Barnett
Whites Crossing
Doublehorn
1670
1680
1690
1700
1710
1720
1730
1740
1750
1760
1770
1780
1790
1800
1810
0 20 40
P wt%
0 20 40
Ca wt%
2 38
Si wt%
20 200
Si/Ti
0 0.5
Ti wt%
0 75
Mo ppm
Simplified lithofacies for XRF interpretation:
Siliceous m.s.
Calcareous siliceous m.s.
Phosphatic p.s.
Argillaceous siliceous m.s.
Biogenic siliceous m.s.
Core lithofacies and strata modifiers:
Siliceous mudstone
Calcareous siliceous mudstone
Skeletal packstone
Phosphatic packstone
Phosphatic glauconitic lime packstone
Phosphate grains
Carbonate concretion
Ripples
Massive pyrite
Burrow
Skeletal material

Figure 16: Idealized depositional stacking pattern of the Barnett lithofacies of the Petty D-6-1 core. The red arrows indicate trends in the clay mineral proxies (Ti curve). The lower Barnett shows four clay pluses with sharp bases and linear decay, the middle Barnett is characterized by higher clay content, and the upper Barnett shows lower clay content. The phosphatic packstone facies is characterized by the P curve, which in the lower and middle Barnett is largely restricted to the phosphatic packstone facies at the top of each unit. The upper Barnett, however, has many more occurrences of the facies, the increase in the phosphatic packstone facies in the upper Barnett was not used as a subdivision because there was no apparent change in the Ti curve. The argillaceous siliceous mudstone facies is characterized by a high Ti concentration and low Ca concentration as well as a high Mo concentration. The Mo concentration fluctuates throughout the Barnett strata, somewhat mimicking the Ti curve, and shows it highest concentration in the middle Barnett. The argillaceous siliceous mudstone facies is observed at the high Ti concentrations and the biogenic siliceous mudstone facies is observed at the low Ti concentrations.

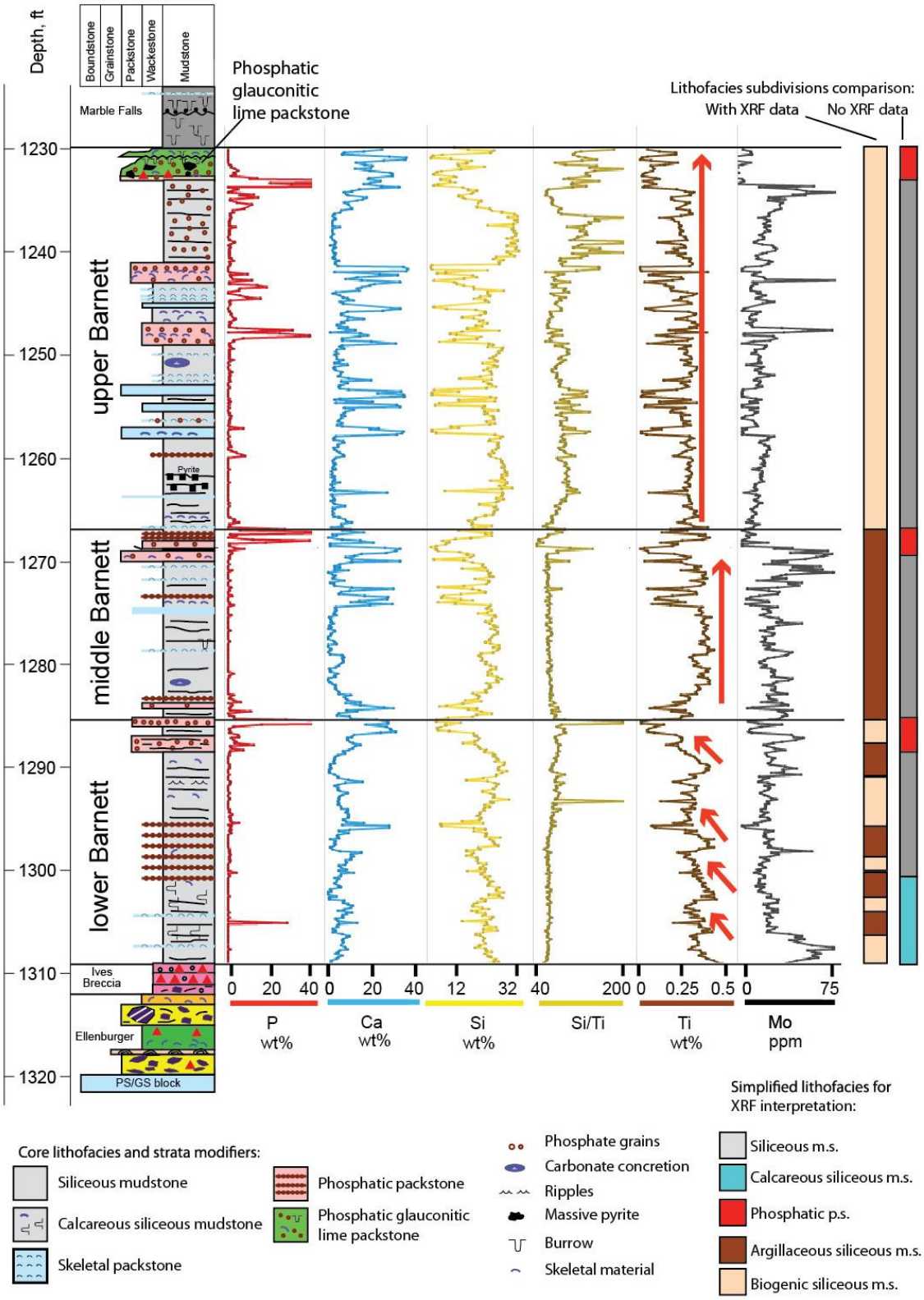
Depth, ft
Boundstone
Grainstone
Packstone
Wackestone
Mudstone
Marble Falls
Phosphatic glauconitic lime packstone
Lithofacies subdivisions comparison:
With XRF data
No XRF data
upper Barnett
middle Barnett
lower Barnett
Pyrite
Ives Breccia
Ellenburger
PS/GS block
1230
1240
1250
1260
1270
1280
1290
1300
1310
1320
0 20 40
P wt%
0 20 40
Ca wt%
12 32
Si wt%
40 200
Si/Ti
0 0.25 0.5
Ti wt%
0 75
Mo ppm
Core lithofacies and strata modifiers:
Siliceous mudstone
Calcareous siliceous mudstone
Skeletal packstone
Phosphatic packstone
Phosphatic glauconitic lime packstone
Phosphate grains
Carbonate concretion
Ripples
Massive pyrite
Burrow
Skeletal material
Simplified lithofacies for XRF interpretation:
Siliceous m.s.
Calcareous siliceous m.s.
Phosphatic p.s.
Argillaceous siliceous m.s.
Biogenic siliceous m.s.

Figure 17: Idealized depositional stacking pattern of the Barnett lithofacies of the Lee C-5-1 core. The same geochemical trends are observed as they are described in Figure 16.

USE OF XRF DATA TO INTERPRET REGIONAL LITHOFACIES VARIABILITY

For interpretation purposes, it is important to understand the Barnett lithofacies before evaluating the XRF results. With lithofacies characteristics in mind, the most important curves used for the characterization of the Barnett strata in this study are P, Ca, Ti, Si, Si/Ti, and Mo. The P curve was used to identify intrabasinal, phosphorus-rich sections and helped to subdivide the Barnett strata into depositional units. The Ca curve was variably used to identify intrabasinal, phosphate-rich intervals, skeletal and carbonate silt laminae, and carbonate concretions. Instead of the Al, the Ti curve was used as an extrabasinal clay proxy (Calvert and Pederson, 2007) because highly elevated P concentrations affected the calibration corrections, and ultimately the Al concentration (Figure 18A), but elevated phosphorous concentrations do not affect the calibration corrections and measurement accuracy of Ti concentrations. Figure 18B demonstrates that Ti and Al have a strong correlation illustrating that Ti is a viable primary proxy for extrabasinal clay content. The Si curve is a proxy for all silica-bearing phases, and in place of the Si/Al ratio, the Si/Ti ratio was used to evaluate excess silica attributed to biogenic silica (Calvert and Pederson, 2007). In Figure 18C the circled data cluster above the linear trendline are attributed to excess (biogenic) silica. The Mo curve was used to assess the redox potential of the water column because Mo precipitates from the water column and accumulates in sediments in euxinic (sulphidic) waters (Calvert and Pederson, 2007; Emerson and Huested, 1991).

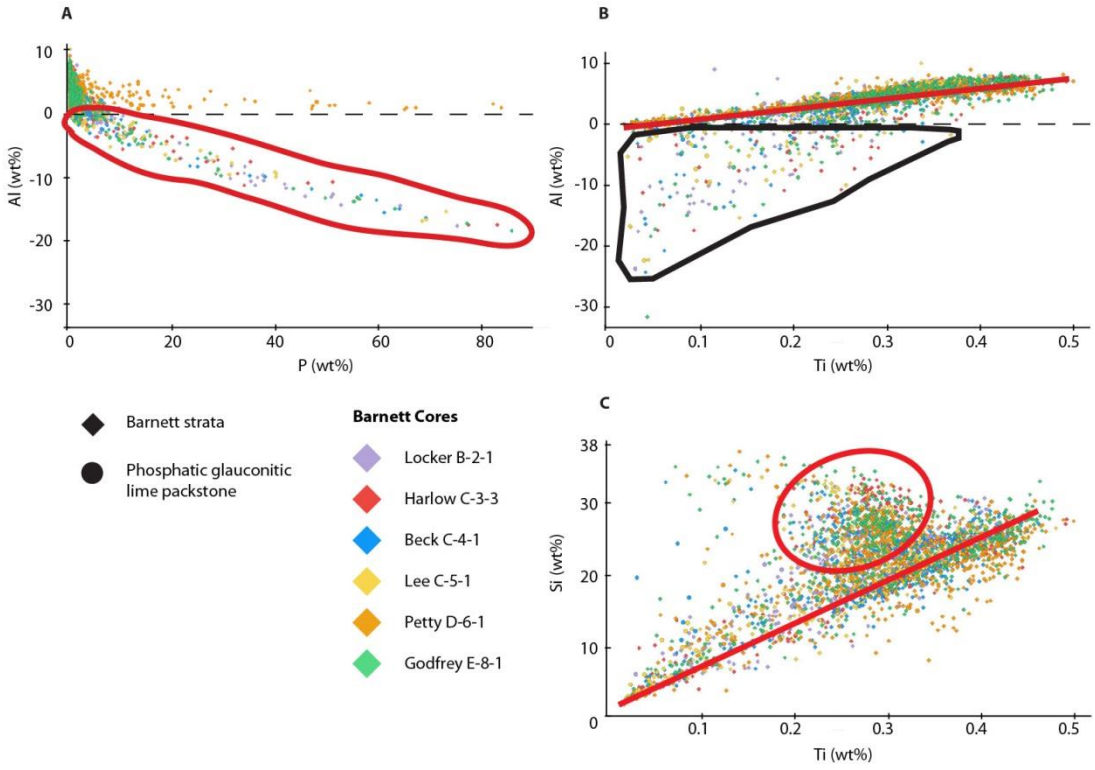

Figure 18: XRF elemental cross-plots: (A) Cross-plots of %Al versus %P showing increasingly negative %Al with increasing %P (red outline); (B) Cross-plots of %Al versus %Ti illustrating the strong correlation between the elements (red line) and positive %Ti where %Al is negative (black outline); (C) Cross-plots of %Si versus %Ti showing a strong correlation (red line) with a large clustering of data (red oval) falling off the correlation time. The points plotted in and around the red oval are excess silica and is attributed to biogenic silica.

Subdivision of the Siliceous Mudstone Facies Using XRF Data

By coupling XRF results with thin-section observations, the siliceous mudstone lithofacies was subdivided in six cores (Locker B-2-1, Harlow C-3-3, Beck C-4-1, Lee C-5-1, Petty D-6-1, and Godfrey E-8-1) into (1) biogenic siliceous mudstone and (2) argillaceous siliceous mudstone facies (Figures 16 and 17). In cores without XRF results the siliceous mudstone facies could not be subdivided with confidence. The argillaceous siliceous mudstone facies corresponds with the high Ti and the presence of abundant agglutinated foraminifera, and the biogenic siliceous mudstone facies corresponds with low Ti and the presence of sponge spicules with lesser amounts of agglutinated foraminifera.

Argillaceous Siliceous Mudstone

Detrital, silt-sized quartz is interpreted as the dominant source of silica where agglutinate foraminifera are observed in high abundance with an absence of calcite-replaced sponge spicules and radiolarians. Some of the agglutinate foraminifera tests are flattened, enhancing laminae in the dark, organic-rich matrix, and other tests have their original morphology preserved *via* pyrite precipitation in the test cavities (Figure 9E). Clusters of silt-sized quartz grains were observed in association with agglutinated foraminifera. Pike and Kemp (1996) interpreted these to be discarded "detritic covers" associated with foraminifera growth.

Biogenic Siliceous Mudstone

Biogenic quartz also contributes a significant portion of silica to the formation. Sponge spicules (common) and radiolarians (rare) (Figure 9F-G) are concentrated in the

facies. Most of the sponge spicules and radiolarians are completely or partially replaced by calcite, thus it is interpreted that the microcrystalline quartz observed and measured with XRF in the mudstone matrix is the authigenic product of the calcite replacement.

Geochemical Trends of the Lower Barnett Section using XRF Data

The lower Barnett strata record cyclic inputs of extrabasinal sediments (Figures 16 and 17). The Ti curve reflects the cyclicity with sharp basal increases in Ti concentration followed by linear decay. The Si curve mimics the Ti curve, and indicates that cyclic pulses of detrital quartz and extrabasinal clays were transported into the basin. The low Si/Ti ratio suggests that the majority of the rock forming silica in the lower Barnett originate from extrabasinal sources. The variations of Ca concentration show the opposite trend to the Ti and Si curves. When extrabasinal quartz and clays are low, the intrabasinal carbonate minerals are high, suggesting that there is background sedimentation composed of intrabasinal sediments (carbonate silts and biogenic silica) that contributed sediment throughout the deposition of the lower Barnett but its overall contribution to the strata was diminished by the more dominant influx of the extrabasinal sediments. The trends terminate at the occurrence of the phosphatic packstone interval, represented by the P curve. The Mo curve does not covary with the other elements, nor does it show concentration trends. Overall it remained elevated during the lower Barnett deposition with some fluctuations of increased concentration.

Geochemical Trends of the Middle Barnett Section using XRF Data

The middle Barnett does not record cyclic inputs of extrabasinal sediments, rather it shows an elevated influx of extrabasinal sediments throughout the interval (Figures 16 and 17). The Ti is elevated, with rare dips in concentration associated with carbonate silt beds. The Si curve mimics the Ti curve, and indicates that detrital quartz and extrabasinal

clays were transported into the basin. The low Si/Ti ratio suggests that the majority of the rock-forming silica in the middle Barnett is from extrabasinal sources. The Ca curve shows low concentrations except at rare occurrences of the skeletal packstone facies, suggesting that intrabasinal sediments (skeletal debris, carbonate minerals, and biogenic silica) contributed to the sediment supply throughout the deposition of the middle Barnett, but to a lesser amount than the extrabasinal sediments. The trends terminate at the occurrence of the phosphatic packstone interval, represented by the P curve. The Mo does not covary with the other elements; overall it shows elevated concentrations in the middle Barnett with a significant concentration increase near the top of the middle Barnett.

Geochemical of the Upper Barnett Section using XRF Data

The upper Barnett is characterized by a decreased influx of extrabasinal sediments throughout the interval (Figures 16 and 17). The Ti concentration in the upper Barnett is low compared to the lower and middle Barnett. The Si curve mimics the Ti curve in shape but remains at the same concentration as the middle Barnett. This indicates that detrital quartz and extrabasinal clays are contributing less sediment to the basin than was the case in the middle Barnett. The high Si/Ti ratio suggests that more of the silica in the upper Barnett originated from intrabasinal, biogenic sources rather than extrabasinal, detrital sources. The highly variable Ca concentrations are associated with occurrences of the skeletal packstone and phosphatic packstone facies, as well as carbonate concretions. This also suggests that intrabasinal sediments contributed more to the sediment supply of the upper Barnett than extrabasinal sediments, and the association of carbonate concretions with the upper Barnett suggests slower sedimentation during upper Barnett deposition than during the deposition of the lower and middle Barnett intervals. The

trends terminate at the occurrence of the phosphatic glauconitic lime packstone interval, represented by the P curve. The Mo does not covary with the other elements, the concentration at the base of the upper Barnett is sharply lower than the concentration at the top of the middle Barnett, and throughout the upper Barnett the Mo concentration gradually increases returning to the elevated concentration observed at the top of the middle Barnett in the phosphatic glauconitic lime packstone unit. The Mo concentration however sharply drops in this unit as it grades into the Pennsylvanian Marble Falls facies.

USE OF CORE DATA IN INTERPRETING REGIONAL LITHOFACIES VARIABILITY

The regional stratigraphic cross sections (Figures 19-22) are hung on the top of the phosphatic glauconitic lime packstone unit because it makes an excellent regional marker bed.

The Llano Uplift was a regional structural control on the deposition of the Barnett strata, limiting subsidence of the southern FWB during the approach of Gondwana toward Laurussia. The tectonic stresses generated by the fold-thrust front activated faults prior to and during Barnett deposition, and the horst and graben structures partially controlled lithofacies distribution during the deposition of the lower Barnett. Evidence for syndepositional fault movement includes the preservation of the Devonian Doublehorn Shale in graben structures, a thickened lower Barnett section in graben structures, and the offset of the phosphate bed correlations across the study area. Strata on the Llano Uplift show increased variability because of the horst and graben structures that created a paleotopographic profile which controlled initial sediment distributions (Figures 19 - 20). Cores more distal to the Llano Uplift show less thickness variability than cores proximal to the Llano Uplift (Figures 21 and 22).

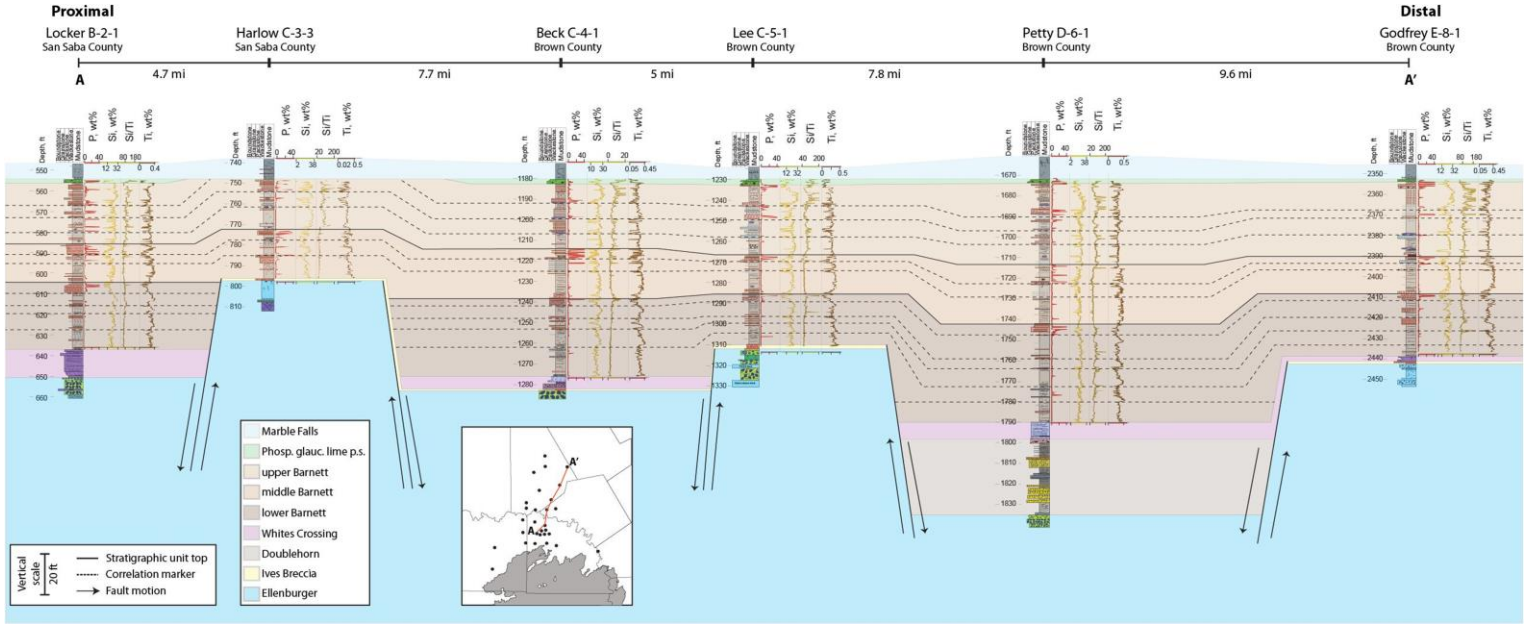

Figure 19: South to north cross section (A-A') depicting facies architecture in the Barnett Formation using the six cores that were scanned through the Barnett strata for XRF data.

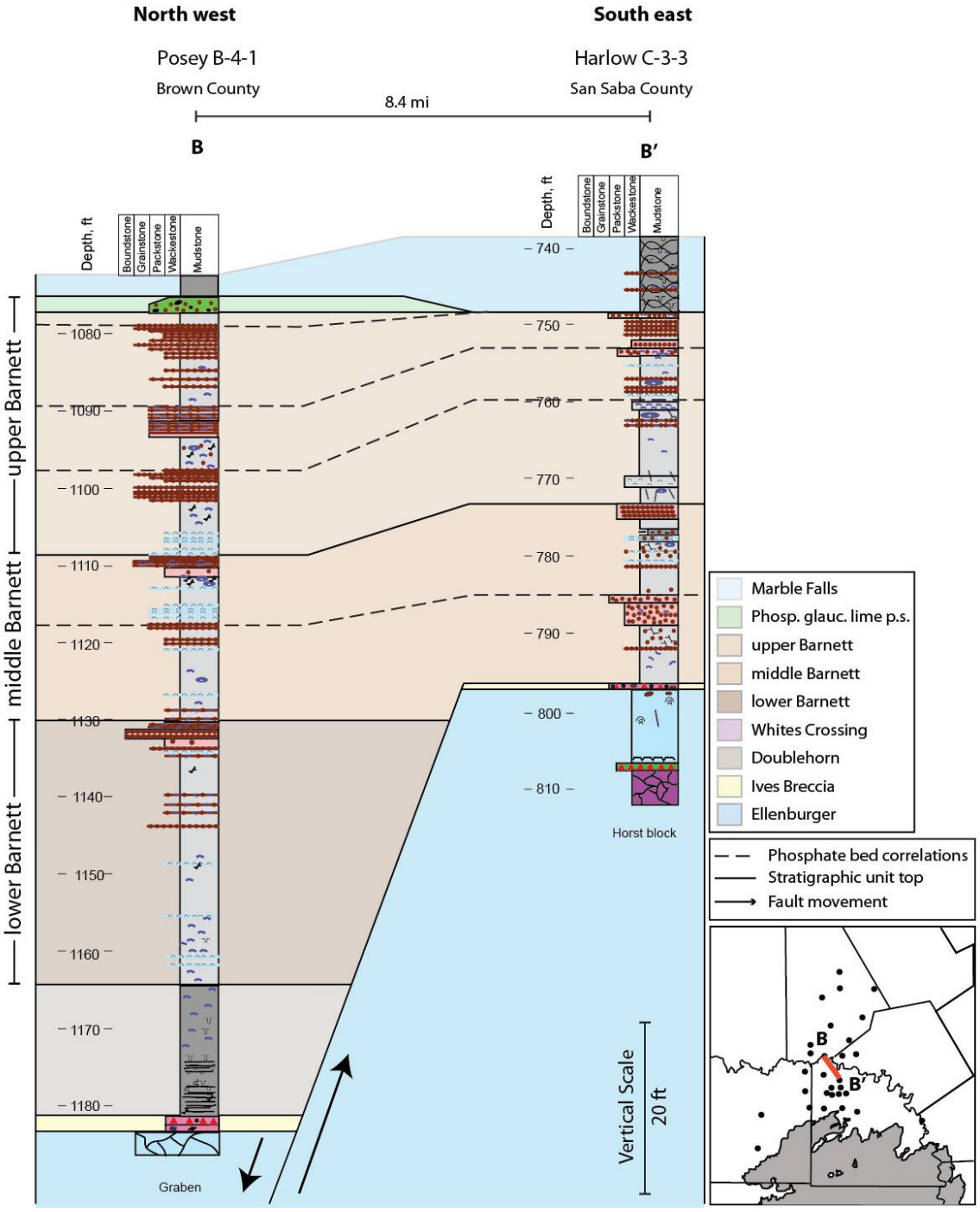

Figure 20: Northwest-southeast cross section (B-B') emphasizing the strata differences between cores located in graben structures (Posey B-4-1) and cores located on horst blocks (Harlow C-3-3). This cross section shows sediment bypass of calcareous siliceous mudstone.

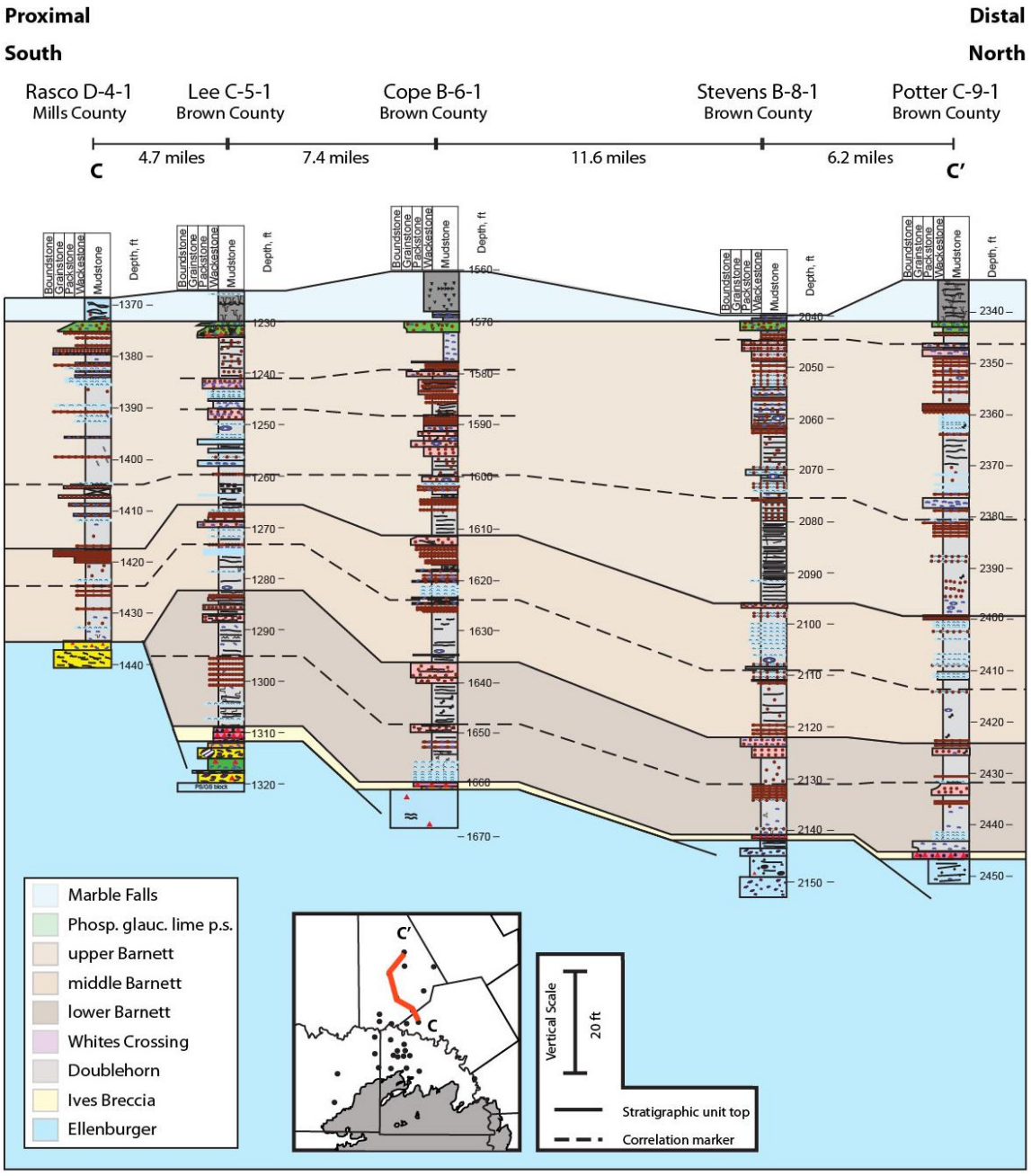

Figure 21: South-north cross section (C-C') depicting the facies architecture of the Barnett away from the influence of the Llano Uplift to the south. The Rasco D-4-1 area was bypassed during the deposition of the lower Barnett because it was a high area.

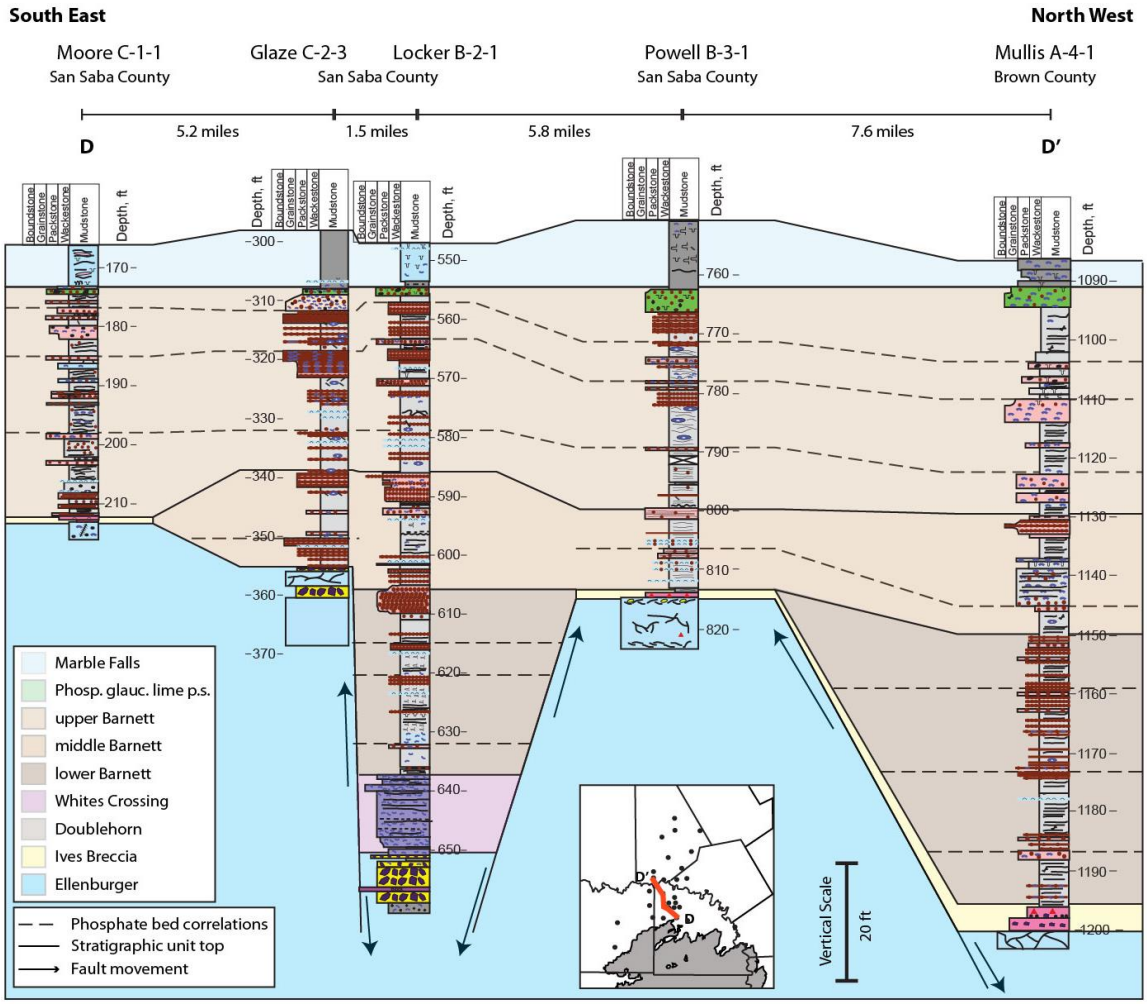

Figure 22: Southeast-northwest cross section (D-D') depicts the facies architecture of the Barnett where there was a strong influence from the Llano Uplift. This is shown by the lower Barnett deposited in the lows of the graben (Locker B-2-1 and Mullis A-4-1) but bypassed the horst block highs (Moore C-1-1, Glaze C-2-3, and Powell B-3-1).

Interpretation of the Lower Barnett Section using Core Data

Proximal to the Llano Uplift, the lower Barnett strata consist of the calcareous siliceous mudstone facies (Figures 19 and 20). The rocks are 15 to 20 ft (4.6 to 6.1 m) thick and are laterally discontinuous unit that was preferentially deposited in graben structures. In cores more distal to the Llano Uplift the lower Barnett strata undergo a lithology change and consist of the siliceous mudstone facies with occurrences of the phosphatic packstone facies prior to the top of the lower Barnett (Figures 21 and 22). Above the initial depositional phase, the remainder of the lower Barnett consists of the siliceous mudstone facies (Figures 19 – 22). The phosphatic packstone facies most commonly interrupts the siliceous mudstone deposition (Figure 22), but is less prevalent in cores containing the calcareous siliceous mudstone basal rock (Figures 19 and 20). Where XRF data are available, the lower Barnett is defined by cyclic sedimentation of the argillaceous siliceous mudstone facies and the biogenic siliceous mudstone facies (Figure 19). These rocks alternate as thin (<10 ft) deposits that are highly correlative from cores proximal to the Llano Uplift to cores distal to the Llano Uplift, with continuity only disrupted by the horst blocks (Figure 19).

Interpretation of the Middle Barnett Section using Core Data

The middle Barnett is primarily composed of the siliceous mudstone facies (Figures 19 – 22). The skeletal packstone facies is present in the middle Barnett, but the deposits cannot be correlated because they are generally less than 1 mm thick. Some stacked deposits of the skeletal packstone were observed, commonly found in stratigraphic association with laminae of the phosphatic packstone facies (Figure 20).

The stacked phosphatic packstone facies that marks the top of the middle Barnett strata is thicker, ~5 ft (1.5 m), in cores proximal to the Llano Uplift, and thinner, <1 ft (<0.3 m) in cores distal to the Llano Uplift (Figures 19-22). The trend of decreasing

thickness of the phosphatic packstone facies is likely related to phosphate grain deposition from the gravity flows, which transported less material to the distal areas. In the middle Barnett this facies is very rarely found outside this interval.

Where XRF data are available, the middle Barnett is defined by thickly bedded, ~15 ft (4.6 m) argillaceous siliceous mudstone facies (Figure 19). These rocks are highly correlative across the study area, regardless of proximity to the Llano Uplift. The trend suggests an increase in basin sediment supply and that bottom water condition remained stable across the study area.

Interpretation of the Upper Barnett Section using Core Data

On the Llano Uplift the upper Barnett is commonly composed of the siliceous mudstone facies, with strata thickening in cores distal to the Llano Uplift (Figures 19, 21 and 22), indicating increased accommodation space toward the north. Carbonate concretions are commonly observed in the upper Barnett and their abundances are interpreted to indicate net low sedimentation rates (e.g. Folk and Land, 1975; Coleman et al., 1993). Also, very common in the upper Barnett are occurrences of the phosphatic packstone facies (Figures 19-22); however, their common occurrence make the facies a challenge to correlate because of the resolution of the core description and distance between cores (Figure 21).Where XRF data are available (Figure 19) the phosphatic packstone facies was correlated using the elemental curves. This revealed highly correlative rock units showing a slight overall thickening trend in cores distal to the Llano Uplift. It also revealed evidence of erosion of the upper Barnett on a horst block (Harlow C-3-3) where as much as 10 ft (3.0 m) of strata were removed.

The Pennsylvanian phosphatic glauconitic lime packstone unit that overlies the upper Barnett strata ranges from 1 to 3 ft (0.3 to 0.9 m), but does not show thickness

trends (Figures 19-22). This suggests that the facies was reworked by bottom currents and distributed evenly over the area.

BARNETT FORMATION EROSION WEST OF THE LLANO UPLIFT

In the northwestern FWB, White (1948) and Henry (1982) both noted the removal of Barnett strata on the Bend Arch in Baylor, Archer, and Clay counties, Texas, related to erosion on the paleohigh. In the southern FWB, Erlich and Coleman (2005) recognized the complete erosion of the Lower Marble Falls Member to the west of the Llano Uplift (33-66 ft; 10-20 m); Wood (2013) also recognized erosion of lower Marble Falls strata in the area by the regional presence of the green illite claystone facies. The current study simplified the depositional history of the area through the recognition of the erosion of the lower, middle, and upper Barnett strata in association with the erosion of the lower Marble Falls (see Figure 28).

Unpublished core descriptions, logged prior to the present study, identified 24 feet of section (7.3 meters) in the Neal A-1-1 and approximately 38 feet of section (11.6 meters) in the Johanson MC-1 cores as Barnett strata. However, the facies identified did not have similar sedimentological characteristics or geochemical attributes of Barnett facies. In addition, no phosphate beds were observed, and the phosphatic glauconitic lime packstone facies was absent at the top of the presumed logged Barnett strata. At first this was explained as a lateral facies shift, but no other such facies shift is observed in the dataset. During the present study, the presumed Barnett strata in the Johanson MC-1 and Neal A-1-1 cores, as well as the Simpson MC-2 core, were reevaluated and reclassified as middle Marble Falls facies and placed into the sequence stratigraphic framework established by Wood (2013) (Figure 23).

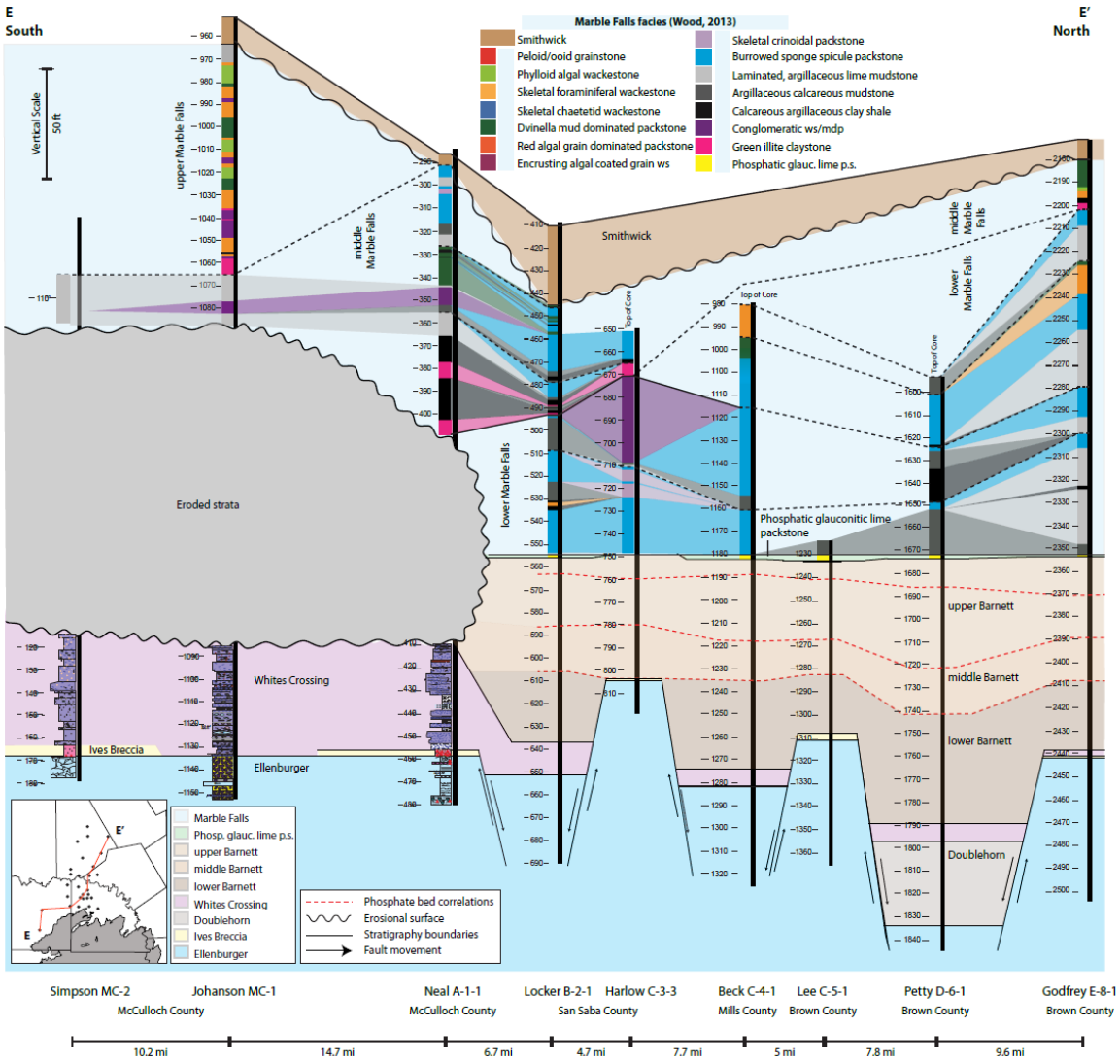

Figure 23: South to north cross section (E-E') displaying eroded Barnett strata to the west of the Llano Uplift. The Marble Falls facies are reconstructed to show the sequence stratigraphic framework established by Wood (2013).

The revised core observations of the section in the Neal A-1-1 noted 19 feet (5.8 meters) of the fissile calcareous argillaceous clay shale, described in Wood (2013) as a deep-water facies deposited under low-energy, restricted anaerobic conditions during low-sedimentation rates. In core it is dark gray color and fissile, containing abundant bryozoans, ostracods, and thin-walled brachiopods. No thin sections were taken in the facies because it is to fissile. The bottom 5 feet (1.5 meters) were identified as disaggregated chunks of the green illite claystone (Figure 23), described in Wood (2013) as either a paleosol formed during a sea-level lowstand or a transgressive marine claystone. In core it is gray-green in color and is used as a contact between the lower and middle Marble Falls facies.

Upon review of the Johanson MC-1 core, 19 feet (5.8 meters) of the argillaceous calcareous mudstone, 10 feet (3.0 meters) of the green illite claystone, 5 feet (1.5 meters) of the conglomeratic wackestone to mud-dominated packstone, and 4 feet (1.2 meters) of the skeletal foraminiferal wackestone to grainstone, (as described by Wood, 2013), were identified (Figure 23). The argillaceous calcareous mudstone is not fissile, is dark gray to black in core, and is a deep-water mudrock that was deposited as part of the middle Marble Falls transgressive system tract. The deposition was interrupted by debris-flow of a conglomeratic wackestone to packstone facies, which is light gray to cream color in core and is composed of skeletal fragments including bryozoans, crinoids, brachiopods, and ostracods. The facies occurs in the middle Marble Falls, in close association with the green illite claystone (Wood, 2013). The green illite claystone was found in association with the interval and also the argillaceous calcareous mudstone. Finally, the skeletal foraminiferal wackestone to grainstone characterized by *Eostaffella*, fusulinids, and

millerelids, as well as peloids, coated grains, and superficial ooids occurs above these facies and, according to Wood (2013), is present in the upper Marble Falls.

The Simpson MC-2 core was not previously described because it was not slabbed. The present study logged the core from the Ellenburger Group through the Marble Falls, but no Barnett strata were observed. The Marble Falls argillaceous calcareous mudstone was observed to unconformably overlie the Whites Crossing (Figure 23). It was interpreted to be equivalent to the argillaceous calcareous mudstone found in the middle Marble Falls of the Johanson MC-1 core.

Aside from the identification of Marble Falls facies, the cores also lack phosphate grains, which are characteristic of the Barnett strata in the region, and the Pennsylvanian phosphatic glauconitic lime packstone unit. The description of the facies and thin section observations differed from the Barnett lithofacies. The other 26 cores in the dataset display Barnett lithofacies, correlative phosphate beds, and contain the Pennsylvanian phosphatic glauconitic lime packstone unit; they do not display the facies that were misclassified as Barnett outside of the Marble Falls Formation.

The erosional event that occurred during the Pennsylvanian removed at least 40 feet (12.2 meters) of lower Marble Falls strata, 2 feet (0.6 meters) of the phosphatic glauconitic lime packstone unit, and 30 feet (9.1 meters) of the Barnett Formation from the area (Figure 23). The erosion of the Barnett strata is restricted to the west of the Llano Uplift where accommodation space was less than that north of the Llano Uplift and further from the influence of the paleohigh. These cores are also located near or on other paleohighs, such as the Hall Uplift (Turner, 1970), whereas cores to the north were buried more deeply and the strata were not eroded.

PHOSPHOGENESIS DEPOSITIONAL MODEL

Phosphate ooids, grains, and intraclasts are important components of the Barnett strata in the southern FWB in both abundance and use for correlations. For these reasons a phosphogenesis model is discussed before a depositional model for the Barnett Formation is presented. A literature review is presented here that identifies a phosphogenesis model applicable to the facies relationships, grain types, and grain-to-grain relationships of the phosphatic packstone facies in the Barnett strata and the Pennsylvanian phosphatic glauconitic lime packstone unit.

In modern environments phosphogenesis occurs at continental margins affected by upwelling which brings phosphorous-enriched waters to the surface, promoting primary productivity in the photic zone, leading to the development of suboxic to anoxic bottom waters and the supersaturation of pore waters with dissolved phosphate (Burnett, 1977; Föllmi, 1993; Glenn et al., 1994a; Föllmi, 1996). With an abundant phosphorous supply, a zone of phosphogenesis (ZOP) develops on the outer shelf/upper slope at the upper boundary of the oxygen minimum zone (Figure 24) (Wignall, 1994; Föllmi 2016). In this zone the phosphorous is removed from the biologic cycling and concentrated in the sediment by an Fe-redox pumping mechanism that promotes the precipitation of apatite (Figure 25A) (Baturin, 1972; Föllmi, 1996; Trappe, 1998; Hiatt et al., 2015; Föllmi, 2016).

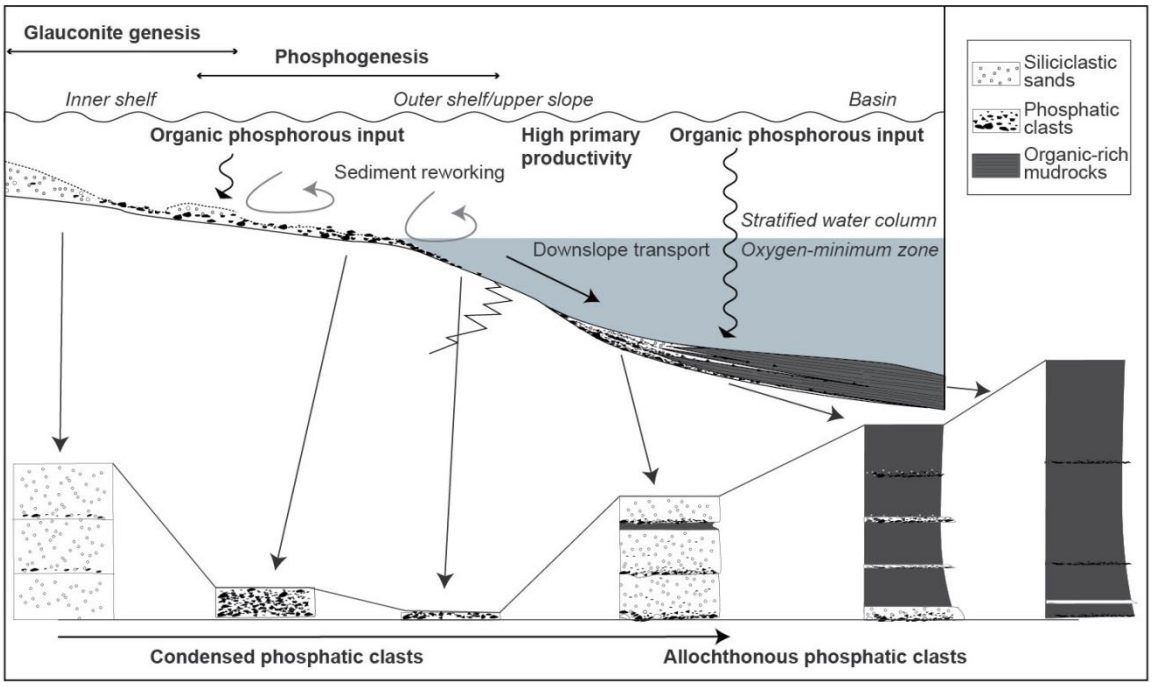

Figure 24: Idealized phosophgenesis model. Phosphate forms on the outer-shelf/upper-slope at the oxygen-minimum zone. Vertical migration of the redox boundary in the sediment allows for multiple episodes of phosphosgensis at the outer-shelf/upper-slope and lateral transport downslope producing interbedding of the phosphate grains and organic-rich mudrocks. Glauconite genesis occurs on the inner shelf. Modified from Follmi (1996) and Suan et al. (2011).

This mechanism creates a chemical gradient in the sediment that promotes phosphate mineral precipitation by the adsorption of organic phosphorous onto Fe-oxyhydroxides in oxic bottom waters, and upon burial the phosphorous is released in the suboxic to anoxic interface where it becomes concentrated and precipitates as apatite (Jarvis et al. 1994; Föllmi, 1996). The pumping mechanism inhibits phosphorous from escaping from the sediments into the overlying water column by readsorption onto the Fe-oxyhydroxides (Jarvis et al., 1994). This zone is restricted to the upper 5 to 20 cm of sediment (Pufahl and Grimm, 2003) where phosphorous and other elements are readily available from seawater and alkaline elements are abundant (Figure 25A) (Glenn et al., 1994b; Trappe, 1998).

Apatite grain nucleation and crystallization occurs on existing mineral surfaces and biologic material (Föllmi, 1996), and some studies have attributed apatite precipitation to bacteria nucleation sites (e.g. Dahanayake and Krumbein, 1986; Schulz and Schulz, 2005; Bailey et al., 2007). Once nucleated, precipitation preferentially occurs on an existing apatite grain until phosphorous concentrations are too low (Van Cappellen, 1991) or alkaline concentrations are too high (Baturin and Savenko, 1985; Glenn et al., 1988). Pufahl and Grimm (2003) recognized that phosphatic ooids form by two mechanisms: (1) phosphogenesis, sediment reworking, reburial, and continued phosphogenesis, and (2) phosphogenesis, vertical migration of the redox boundary in the sediment, and continued phosphogenesis (Figure 25B).

In sediment, a phosphate accumulation could remain pristine, as a single phosphate generation, undisturbed by bottom-water currents; it could become condensed through sediment winnowing and erosion; or it could become allochthonous re-exposing the deposit at the sediment-water interface through sediment reworking, lateral transport, and winnowing (Figure 25C) (Föllmi et al., 1991 and Föllmi, 1996). The phosphate

stratification type and energy intensity of the basin are interpreted based on the grain-to-grain relationships, internal boundaries separating phosphate accumulation layers, internal microstratigraphic relationships, and sharp and erosive basal contacts (Föllmi, 1996).

In the Barnett strata the phosphatic packstone facies is interbedded with the organic-rich siliceous mudstone facies (Figure 12A-D), the phosphatic ooids show concordant concentric phosphate laminae (Figures 12G-H and Figure 13C), and condensed (Figures 12G-H and Figure 13C) to allochthonous deposits (Figure 15H-I).

A

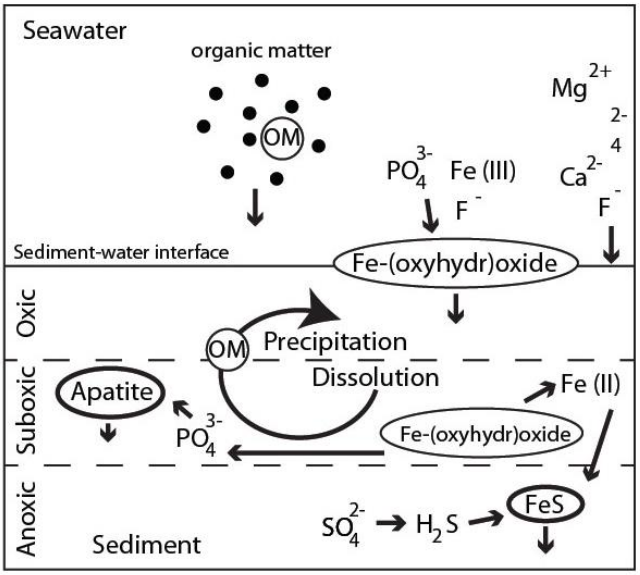
Seawater
organic matter
OM
Mg^{2+}
SO_4^{2-}
PO_4^{3-}
Fe (III)
F^-
Ca^{2-}
F^-
Sediment-water interface
Fe-(oxyhydr)oxide
Oxic
OM
Precipitation
Dissolution
Suboxic
Apatite
PO_4^{3-}
Fe (II)
Fe-(oxyhydr)oxide
Anoxic
SO_4^{2-}
H_2S
FeS
Sediment

B

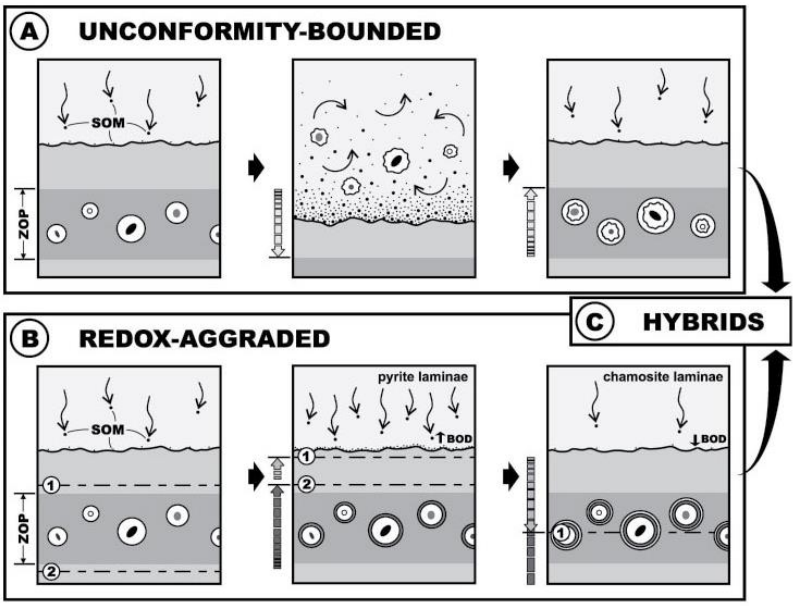
A
UNCONFORMITY-BOUNDED
SOM
ZOP
B
REDOX-AGGRADED
SOM
ZOP
pyrite laminae
BOD
chamosite laminae
BOD
C
HYBRIDS

C

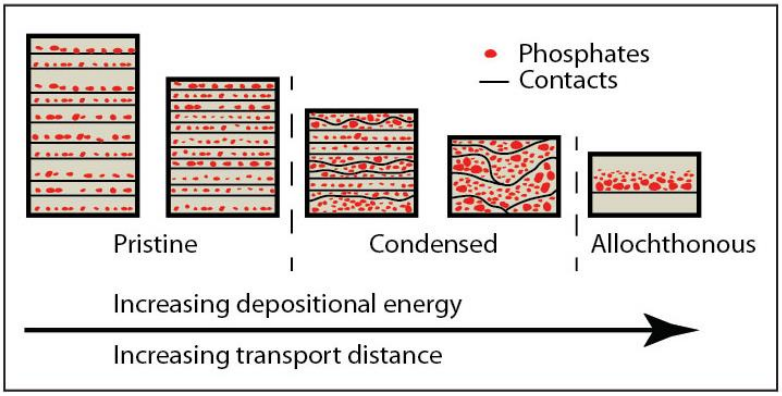
Phosphates
Contacts
Pristine
Condensed
Allochthonous
Increasing depositional energy
Increasing transport distance

Figure 25: Phosphate grain accumulation schematics and stratification types. (A) Schematic diagram of the Fe-redox cycle. The phosphorous from the organic matter is taken up by the Fe-oxyhydroxy complexes. These complexes are buried and release the phosphorous in the sediment where it accumulates until high concentrations promote the precipitation of apatite. The upward migration of phosphorous is recycled back into the sediment by readsorption onto the Fe-oxyhydroxy complex (Trappe, 1998). (B) Mechanism of phosphatic ooid accretion from Pufahl and Grimm (2003). (C) Diagram depicted the different stratification types found in sedimentary phosphate accumulations. Modified from Follmi (1996).

BARNETT FORMATION DEPOSITIONAL MODEL

Based on lithofacies, sedimentary structures, flora and fauna, organic and inorganic geochemistry, as well as the regional setting, a depositional model is presented for the Barnett Formation in the southern FWB that suggests the Barnett facies accumulated at the base of a deep-water slope to basinal setting between two widely separated paleotopographic highs, the Chappel Shelf to the west and the Llano Uplift to the south (Figure 26).

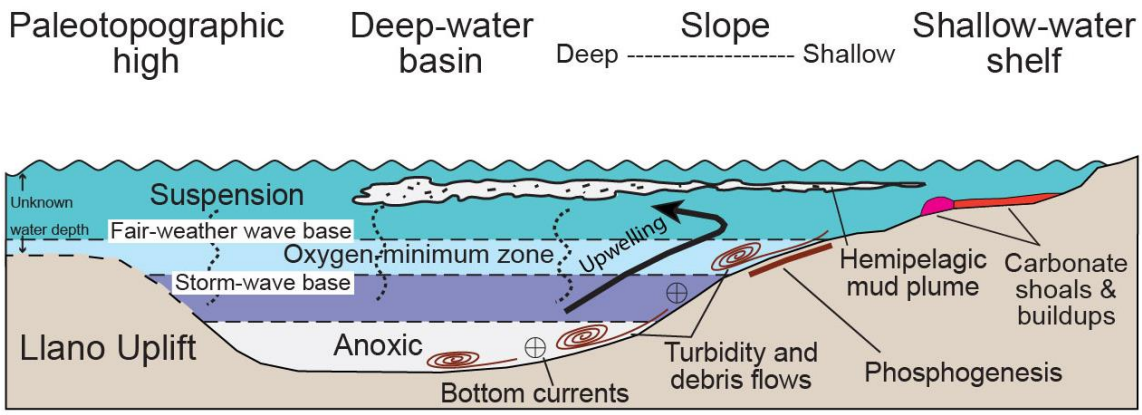

Figure 26: Generalized depositional model for the Barnett Formation that shows depositional processes that affected the strata. Highly modified from Loucks and Ruppel (2007).

DEPOSITIONAL SETTING AND PROCESSES

The Barnett Formation was deposited in the FWB, a foreland basin that had limited connectivity to the open ocean which contributed to a stratified water column, shown by high phosphorous content, high organic matter content (average TOC 4.5%; Appendix A), elevated concentrations of Mo, and pyrite framboids throughout the section. During its deposition, basin upwelling along the Chappel Shelf, as well as terrigenous phosphorous inputs, brought phosphorous to the photic zone of the overlying water column and promoted primary productivity. Organic matter accumulations on the seafloor led to the high concentrations of organic phosphorous in the sediments. The high phosphorous concentrations promoted the formation of a ZOP at the outer-shelf/upper-slope near the oxic-suboxic redox boundary.

In the northern FWB the Barnett was deposited over a 25-m.y. period that had an average sediment accumulation rate of 14 μm/yr (Loucks and Ruppel, 2007). The biostratigraphic age controls in the southern FWB are not refined enough to calculate a precise sedimentation rate for different intervals, but because the observed lithofacies and depositional processes of the northern FWB are very similar to those of the southern FWB we suggest the southern FWB had a similar sedimentation rate. The significantly thicker strata in the northern FWB (550-1000 ft, 168-1000 m; Loucks and Ruppel, 2007; Pollastro, 2007) than the southern FWB (37-126 ft; 11-38 m) would suggest a lower sedimentation rate in the southern FWB, however, deposition of the Barnett strata in the northern FWB is interpreted to have begun earlier (Ruppel, 1989) than the Barnett deposition in the southern FWB based on the times constrained by conodont data from Barnett outcrops in the hill country of Texas. Therefore we suggest a maximum sediment

accumulation rate of the southern FWB to be 14 μm/yr with the possibility that it was less than that.

The extremely low sedimentation rates and the high organic matter content 4.5% (Hoelke, 2011; Reed and Loucks, 2015; Appendix A) preserved in the Barnett strata indicates anaerobic bottom waters. In an aerobic environment bacteria rapidly consume organic matter, so the high TOC content in a starved basin suggests anoxic bottom waters persisted throughout Barnett deposition. Sedimentological evidence such as rare bioturbation, laminated sediments, fine pyrite framboids, and phosphates, also support this interpretation.

All lithofacies show laminations that have been enhanced by postdepositional compaction; in the northern FWB the siliceous mudstone facies is estimated to show 65% compaction and the skeletal packstone facies is estimated to be compacted by 90% (Loucks and Ruppel, 2007). The laminated sediments are composed of compacted peloids, extrabasinal clays, and quartz and feldspar silt, which are likely sourced from the Caballos Arkansas island chain to the east, and intrabasinal carbonate shell fragments and phosphatic ooids and grains, which are sourced from the Chappel Shelf to the west. All these sediments indicate transport and the fine-grain size of the clays, quartz, and feldspars suggest a long-distance transport mechanism, such as turbidity currents, brought these sediments into the basin. Turbidity currents can transport material for hundreds of miles (Mulder and Alexander, 2001) and deposit a dilute turbidite in the basin because all the coarser material had already deposited before reaching the basin.

Sediment composing the siliceous mudstone facies and the calcareous siliceous mudstone facies was sourced from (1) fine-grained material suspended in the water column (clays, quartz, and feldspar grains) (2) pelagic skeletal material from the overlying water column (rare radiolarians were observed), and (3) from material shed off

the thrust front to the east and the Chappel Shelf to the west. Evidence of more proximal sediment sources include abundant sponge spicules which are transported into the basin from the adjacent slopes. Accumulation of fine-grained particles of clay, organic-matter, etc. is attributed to clay-flocculation in the water column, which forms larger, peloidal grains (Boggs, 1987) that can settle at a faster rate than clay-sized particles. The siliceous mudstone and calcareous siliceous mudstone lithofacies are interpreted to be deposited by settling from gravity flows and hemipelagic settling and later reworking by bottom currents on the basis of the fine-grain size, uniform mineralogical composition, lack of faunal diversity and in situ fauna, as well as starved ripples that were observed throughout the strata which are evidence of higher energy bottom-water currents that reworked sediment.

Detrital, silt-sized quartz is a dominant source of silica where agglutinate foraminifera are dispersed throughout the argillaceous matrix. Studies investigating modern agglutinated foraminifera have found that they can survive short periods of anoxia (e.g. Bernhard and Reimers, 1991). Where they are present the bottom waters are interpreted to have had very low oxygen concentrations (e.g. ~0.05 ml/L or less; Bograd et al., 2002) and there could have been periods of anoxia that lasted for several months at a time (Schieber, 2009). The association of the agglutinated foraminifera with the framboidal pyrite (Figure 9E) is a strong indicator for anoxia in the overlying water column, and suggests that the gravity flows bringing in the sediment transported oxygen into the basin creating an opportunistic environment for the agglutinated foraminifera. However, once the flow stopped the waters became oxygen depleted and halted their proliferation as anoxic waters returned in the basin.

The significant increase in the carbonate content of the calcareous siliceous mudstone facies (31.2% compared to 11.8% in the siliceous mudstone facies) is attributed

to mudflows originating from the Chappel Shelf and transporting fine-grained carbonate material into the basin during the initial Barnett deposition. These mudflows are expressed in the rock by the weakly laminated thin-shelled filibranch mollusk and weakly bioturbated sediments identified to be *Cosmorhaphe* burrows. These burrows are made by vermiform organisms in low-oxygen, fully marine, deep-sea environments (Pemberton et al., 2009) so doomed pioneer surfaces of these burrows suggests that the waters in the southern FWB were anoxic to euxinic during initial Barnett deposition, and once the oxygen transported into the basin was metabolized the vermiform organisms perished.

The presence of the skeletal packstone facies in the strata is evidence of event deposits that interrupt the background sedimentation. The skeletal packstone is interpreted to be deposited by gravity flows of the downslope transport of filibranch mollusk and brachiopod skeletal fragments. The skeletal material was supported by both buoyancy and fluid pressure (Mulder and Alexander, 2001) and as the flow moved downslope phosphate grains were incorporated into the debris flow as an accessory grains. The phosphate grains observed in this facies are interpreted to represent the grains formed at the uppermost limit of the ZOP that became exposed at the sediment surface by bottom-water currents and were not reburied, thus easily being picked up by the flows moving across the area. The skeletal packstone facies occurs as millimeter thick deposits except in sections where multiple flows stack, where they are up to one inch (2.54 cm) in thickness. The thin laminae support long-distant transport of these sediments and are interpreted to be sourced from the upper slope of the Chappel Shelf. The initiation of the gravity flows is likely related to episodic storm events because no discernable depositional pattern was noted.

The phosphatic packstone facies that subdivides the lower and middle Barnett strata are composed mainly of phosphatic ooids and occur at stratigraphic intervals that

correspond with major changes in clay mineral abundances. The phosphatic ooids are interpreted to have formed at the outer shelf/upper slope by a redox-aggradation mechanism, where phosphatic oolitic coatings are attributed to vertical migration of the redox boundary within the sediment evidenced by the concordant concentric phosphate laminae (Pufahl and Grimm, 2003). The ooids are not observed in any other lithofacies and are interpreted to have remained buried in the sediment while bottom water currents reworked the sediment above the ZOP and gravity flows transported other sediment into the basin. The accumulation of condensed deposits of the phosphatic packstone facies in abrupt alternation with the siliceous mudstone facies is therefore interpreted to be a result of downslope transport of ooids from the outer shelf/upper slope. Because these ooids are not seen in any other facies and because their occurrence correlates with major changes in clay mineral abundances we interpret that the ooids are transported into the basin as a result of an allocyclic change that initiated gravity flow transport of sediment from the outer shelf/upper slope.

Though the phosphatic glauconitic lime packstone facies is of Pennsylvanian age it is discussed in the Barnett depositional model because it occurs at the top of the final change in clay mineral abundances, marking the top of the upper Barnett, and signals the end of Barnett deposition. The phosphatic ooids in this facies are also interpreted to have formed at the outer shelf/upper slope by a redox-aggradation mechanism, because of the concordant concentric phosphate laminae (Pufahl and Grimm, 2003), however the high abundance of glauconite grains suggests that sediment was also sourced from inner shelf where there was also a high Fe and K input to create the glauconite grains (Odin & Matter, 1981; Föllmi, 2016). The accumulation of allochthonous phosphatic glauconitic lime packstone facies is thus interpreted to be a result of downslope transport via gravity flows of phosphatic ooids from the outer shelf/upper slope and glauconite grains from the

inner shelf and subjected to subsequent reworking, during a period of sedimentary condensation related to an allocyclic change. This interpretation is supported because a high abundance of glauconite grains in the facies strongly suggests changes in paleoceanographic and paleogeographic conditions of the basin (e.g. Föllmi, 2016) and the presence of both phosphatic ooids and glauconite grains indicates long-term, low-sedimentation rates, and sediment reworking (Föllmi, 2016).

As discussed earlier, the cone-in-cone structures in the Vaca Meurta are late diagenetic features that are linked to hydrocarbon generation and high overpressures interpreted to be a product of differential shear (Rodrigues, 2008; Rodrigues et al. 2009). In the low-thermal maturity Barnett strata of the southern FWB the cone-in-cone structures are interpreted to be generated by differential shear between the siliceous mudstone matrix and the phosphatic packstone facies related to overpressure during hydrocarbon generation and migration. The thermally immature Barnett strata (Appendix A) in the southern FWB could explain why these features did not develop to the large scale as seen in the Vaca Muerta (e.g. Parnell et al., 2000; Rodrigues et al., 2009) and instead are small, few, and isolated.

SEQUENCE STRATIGRAPHY SUMMARY

Sequence stratigraphy applies a chronostratigraphic framework to a depositional model in order to understand facies response to changes of sediment supply and/or in accommodation related to sea-level changes and/or tectonic movements. It is difficult to apply these concepts to basinal mudrocks because of the limited facies variability and also because changes in sea level may not be reflected by the sediment deposited in a basin, for example Ross and Ross (1987) show a possible 12 third order sea level changes during Barnett deposition (Figure 1), but they are not recognizable in the southern FWB.

In this study I apply some sequence stratigraphic concepts to this data set because the phosphatic packstone facies and the phosphatic glauconitic lime packstone unit used to subdivide the Barnett strata are reliable chronostratigraphic marker beds.

In other studies the occurrence of phosphates reflect major climate signal feedbacks and represent major changes in the depositional environment of the strata (e.g. Föllmi et al., 1994; Hiatt and Budd, 2001; Pufahl et al., 2003; Soudry et al., 2004), phosphates have been related to periods of sea-level rise (e.g. Sheldon, 1980; Arthur and Jenkyns, 1981; Baturin, 1982; Riggs, 1984; Cook et al., 1990; Glenn and Arthur, 1990; Riggs and Sheldon, 1990), and the comixing of the phosphates and glauconite grains has previously been related to a sea-level highstand (Amorosi, 1995)..

In this study the occurrence and distribution of the phosphatic packstone facies is not random, other studies have noted this as well (e.g. Föllmi, 1996). The distribution of phosphate-rich intervals have been linked with marine transgression, periods of net low-sedimentation rates, and condensed sections that can persist for several million years (e.g., Krajewski, 1984 and 1989; Hesselbo et al., 1990; Föllmi, 1996; Schutter, 1996; Proust et al., 1998; Trela, 1998; Siegmund et al., 2002; Pufahl et al., 2003; Shields et al, 2004; Brett et al., 2004; Suan et al., 2011). For these reasons the phosphatic packstone facies and the phosphatic glauconitic lime packstone facies are used to define the tops of depositional cycles in the Barnett strata that relate to changes in sea-level.

In this study a cycle is defined as a repeatable large scale pattern of deposition occurring over several million years. It is assumed that the cycles are on the million year time scale because the Barnett strata was deposited over 25-my in the northern FWB (Loucks and Ruppel, 2007). It is likely that there are many other depositional cycles in nearshore facies that record much shorter time frames, but in the basinal setting of the

Barnett strata the deposition rate is so slow that the sea-level fluctuations shown by Ross and Ross (1987) (Figure 1) cannot be defined in the rocks.

The Barnett strata were deposited as a second-order sea-level rise (Figure 1) and the phosphatic packstone facies and phosphatic glauconitic lime packstone facies mark three cycle tops that show an aggradational stacking pattern. In the basin The lower Barnett cycle shows cyclic sedimentation of the distal, argillaceous siliceous mudstone facies and the proximal, biogenic siliceous mudstone facies, terminated at the phosphatic packstone facies cycle top; the middle Barnett cycle shows an increase in the distal, argillaceous siliceous mudstone facies terminated by the phosphatic packstone facies cycle top; and the upper Barnett cycle shows a decrease of the distal, argillaceous siliceous mudstone facies and an increase in the proximal, biogenic siliceous mudstone facies, terminated by the phosphatic glauconitic lime packstone facies cycle top. The cyclic stacking pattern shows an overall aggradational trend because the cycles show minimal facies variability and the same facies stacking pattern, and the sea-level curve (Figure 1) shows high sea-level persisted throughout Barnett deposition. The phosphatic glauconitic lime packstone facies is also interpreted to be the condensed section associated with the maximum flooding surface between the aggradational Barnett Formation and the progradational Marble Falls mudrocks. This interpretation is supported by the high abundance of glauconite grains which strongly supports changes in paleoceanographic and paleogeographic conditions of the basin and both the phosphatic ooids and glauconite grains observed in this unit indicates long-term, low-sedimentation rates (Föllmi, 2016).

STRATIGRAPHIC ARCHITECTURE

In order to better understand the variability and distribution of the Barnett facies, the identified facies relationships were used to create an idealized depositional model (Figure 27) for the lower, middle, and upper Barnett Formation.

LOWER BARNETT DEPOSITIONAL SUCCESSION

Early Barnett sedimentation in the southern FWB was dominated by fine-grain carbonate-rich argillaceous sediments, derived from the adjacent Chappel Shelf, which were transported into the study area via mudflows and dilute turbidites (Figure 27A-C). Its geographic distribution was controlled by the horst and graben topography associated with the Llano Uplift and sediment preferentially accumulated in the graben structures. The resulting strata, calcareous siliceous mudrock facies, are interpreted to record deposition of the shallowest water Barnett sediment in a below storm-wave base, anoxic setting (Figure 27A).

Continued deposition of the lower Barnett was dominated by peloids and an increase in fine-grained quartz sediments and clay minerals, and a corresponding decrease in the carbonate-rich sediments. The resulting strata, siliceous mudstone facies, are interpreted to record the deposition of dilute turbidites that originated from the distal structural highs bounding the basin (Figure 27B). Deposits of well-rounded, phosphate ooids were deposited throughout the study area and are interpreted to be an expression of a depositional cycle top (Figure 27C). The interpreted depositional environment of the lower Barnett strata is below storm-wave base, lower energy, anoxic setting with oxygen transported into the basin during the initial Barnett deposition.

MIDDLE BARNETT DEPOSITIONAL SUCCESSION

Overlying the cycle top, the middle Barnett depositional succession shows less lithologic variability than the lower Barnett (Figure 27D). Sediments were dominated by peloids, fine-grained quartz, and clay minerals. The resulting strata, siliceous mudstone facies, are interpreted to record the deposition of a dilute turbidite that originated from the distal structural highs bounding the basin. Fragmented filibranch mollusks composed the only lithofacies variability in the middle Barnett. The resulting strata, skeletal packstone facies, are interpreted to be sourced from the adjacent Chappel Shelf and transported into the southern FWB via debris flows. Deposits of well-rounded, phosphate ooids at the end of the deposition of the siliceous mudstone facies are interpreted to be an expression of a depositional cycle top (Figure 27E). The interpreted depositional environment of the middle Barnett strata is below storm-wave base, lower energy, anoxic setting.

UPPER BARNETT DEPOSITIONAL SUCCESSION

Overlying the cycle top, the upper Barnett depositional succession shows greater lithologic variability than the middle Barnett (Figure 27F). As was the case for the lower and middle Barnett, sediments for the upper Barnett were dominated by peloids, fine-grained quartz, and clay minerals. The resulting strata, siliceous mudstone facies, however are interpreted to have a greater intrabasinal sediment contribution attributed to hemipelagic settling and less frequent dilute turbidites entering the basin compared to the lower and middle Barnett mudrocks. Evidence for slower sedimentation rates is shown by the common occurrence of carbonate concretions and the common phosphatic packstone facies punctuating the siliceous mudstone facies. Deposits of well-rounded, fine-sand sized glauconite grains and phosphate ooids are interpreted to be the expression of a depositional cycle top and also the maximum flooding surface (Figure 27G), which

marks a transition from anoxic bottom waters of the Barnett strata to shallower, better oxygenated waters characteristic of the Marble Falls. The interpreted depositional environment of the upper Barnett strata is below storm-wave base, lower energy, anoxic setting.

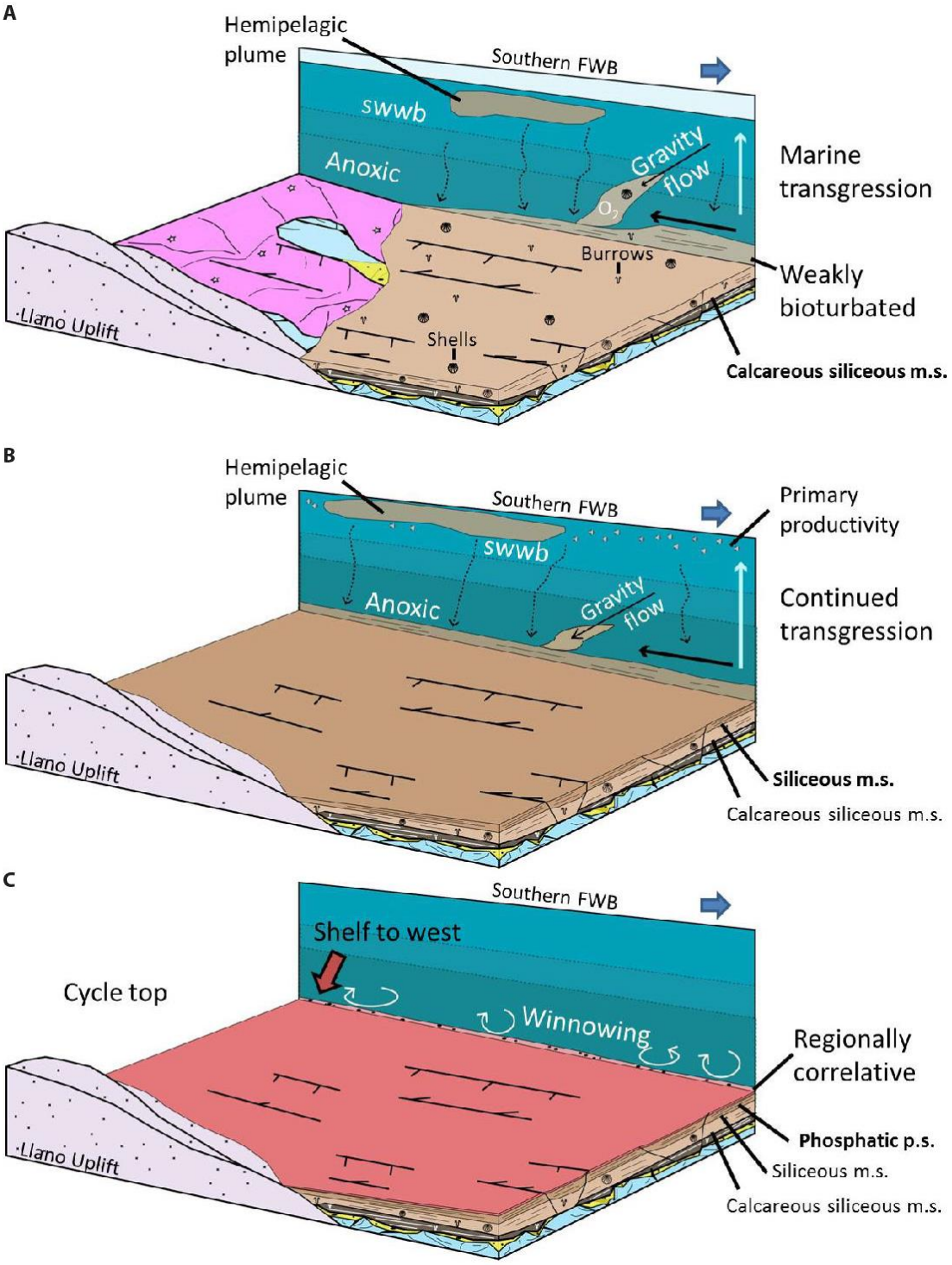
A
Hemipelagic plume
Southern FWB
SWWB
Anoxic
Gravity flow
O_2
Marine transgression
Burrows
Weakly bioturbated
Llano Uplift
Shells
Calcareous siliceous m.s.
B
Hemipelagic plume
Southern FWB
Primary productivity
SWWB
Anoxic
Gravity flow
Continued transgression
Llano Uplift
Siliceous m.s.
Calcareous siliceous m.s.
C
Southern FWB
Shelf to west
Cycle top
Winnowing
Regionally correlative
Llano Uplift
Phosphatic p.s.
Siliceous m.s.
Calcareous siliceous m.s.

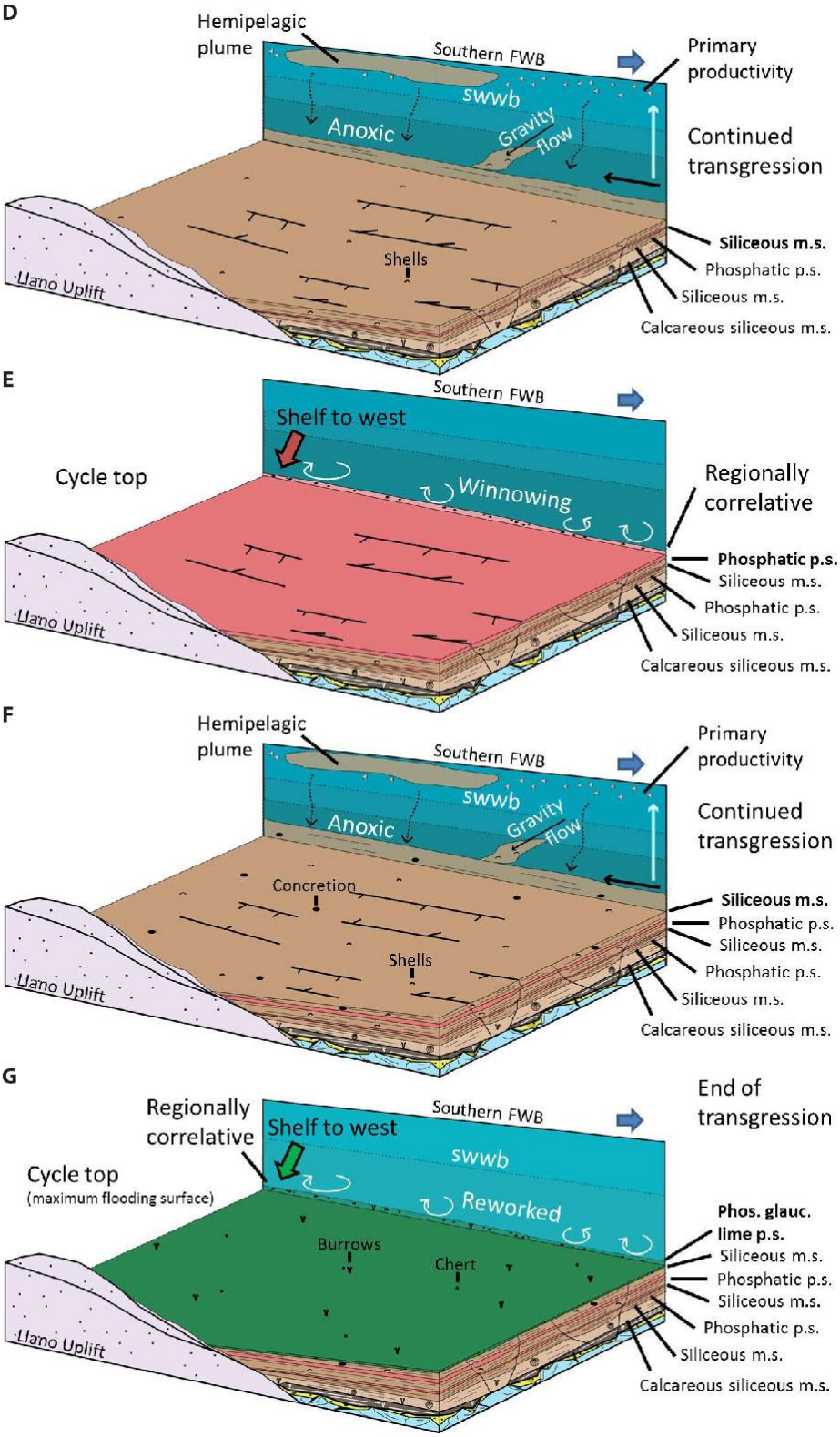
D
Hemipelagic plume
Southern FWB
swwb
Anoxic
Gravity flow
Primary productivity
Continued transgression
Shells
Llano Uplift
Siliceous m.s.
Phosphatic p.s.
Siliceous m.s.
Calcareous siliceous m.s.
E
Southern FWB
Shelf to west
Cycle top
Winnowing
Regionally correlative
Phosphatic p.s.
Siliceous m.s.
Phosphatic p.s.
Siliceous m.s.
Calcareous siliceous m.s.
Llano Uplift
F
Hemipelagic plume
Southern FWB
swwb
Anoxic
Gravity flow
Primary productivity
Continued transgression
Concretion
Shells
Llano Uplift
Siliceous m.s.
Phosphatic p.s.
Siliceous m.s.
Phosphatic p.s.
Siliceous m.s.
Calcareous siliceous m.s.
G
Regionally correlative
Shelf to west
Southern FWB
swwb
Cycle top
(maximum flooding surface)
Reworked
End of transgression
Burrows
Chert
Llano Uplift
Phos. glauc. lime p.s.
Siliceous m.s.
Phosphatic p.s.
Siliceous m.s.
Phosphatic p.s.
Siliceous m.s.
Calcareous siliceous m.s.

Figure 27: Block models showing the depositional setting and facies patterns during the (A-C) lower Barnett, (D-E) middle Barnett, and (F-G) upper Barnett. (A) Deposition of the calcareous siliceous mudstone; (B) deposition of the siliceous mudstone; (C) deposition of the phosphatic packstone; (D) deposition of the siliceous mudstone and skeletal packstone; (E) deposition of the phosphatic packstone; (F) deposition of the siliceous mudstone, skeletal packstone, and carbonate concretion generation; (G) deposition of the phosphatic glauconitic lime packstone.

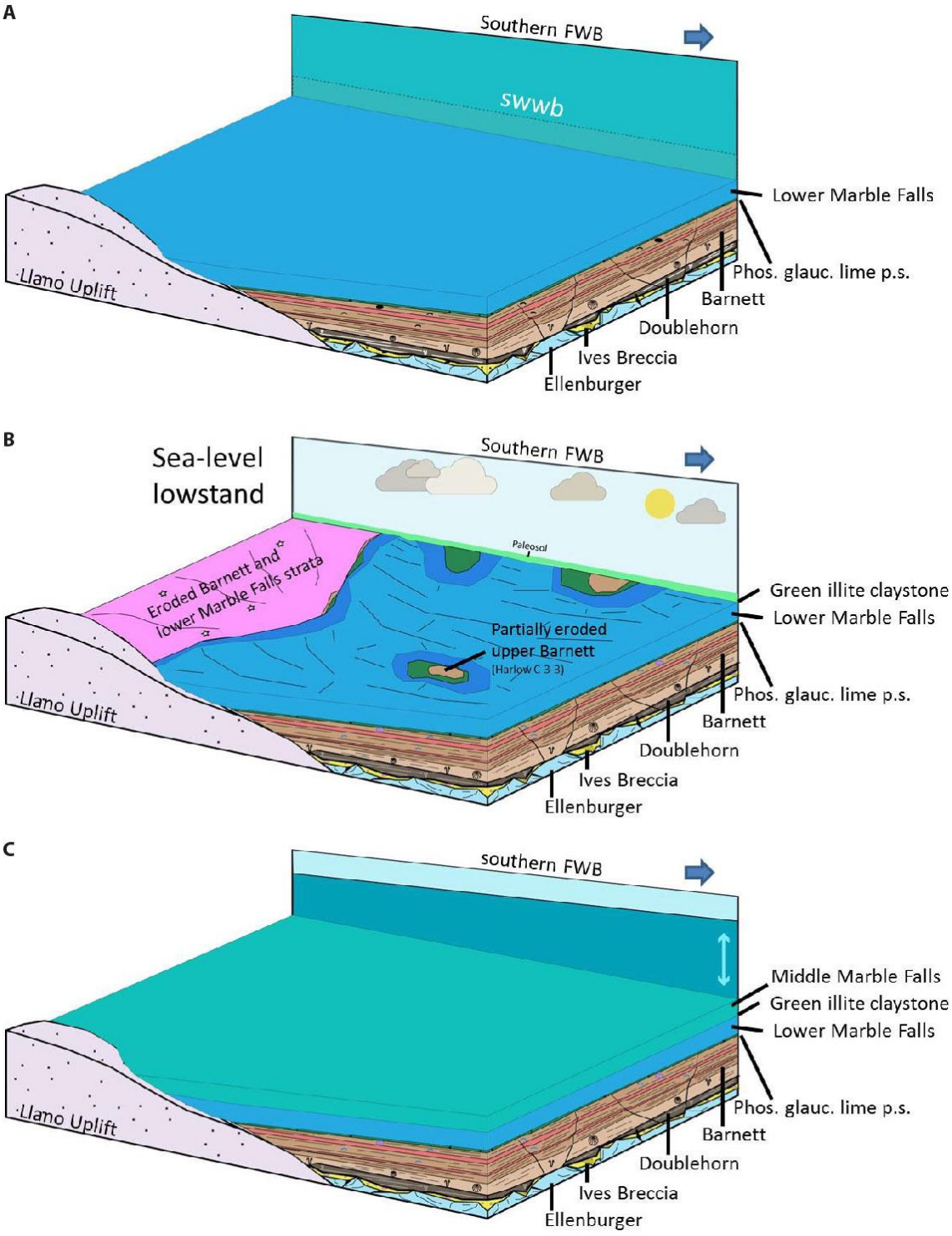
A
Southern FWB
swwb
Lower Marble Falls
Phos. glauc. lime p.s.
Barnett
Doublehorn
Ives Breccia
Ellenburger
Llano Uplift
B
Sea-level
lowstand
Southern FWB
Paleosol
Eroded Barnett and
lower Marble Falls strata
Green illite claystone
Lower Marble Falls
Partially eroded
upper Barnett
(Harlow C 3 3)
Phos. glauc. lime p.s.
Barnett
Doublehorn
Ives Breccia
Ellenburger
Llano Uplift
C
southern FWB
Middle Marble Falls
Green illite claystone
Lower Marble Falls
Phos. glauc. lime p.s.
Barnett
Doublehorn
Ives Breccia
Ellenburger
Llano Uplift

Figure 28: Block models showing the depositional setting of the lower Marble Falls to the middle Marble Falls. (A) The lower Marble Falls was deposited across the basin after the cessation of sedimentary condensation recognized by the phosphatic glauconitic packstone facies, (B) a sea-level fall caused the the lower Marble Falls and the lower, middle, and upper Barnett strata to erode to the west of the Llano Uplift and on isolated horst blocks (e.g. Harlow C-3-3), (C) the green illite claystone was deposited as sea-level transgressed (Wood, 2013) and the middle Marble Falls was deposited across the region.

DISCUSSION

The data in this study suggest an anoxic, deep-water, below storm-weather wave base, depositional setting for the Barnett strata in the southern FWB. Evidence supporting this interpretation includes depositional processes and fauna that suggest downslope transport from shallower water areas and distal sediment sources. Laminated sediments, rare bioturbation, elevated Mo concentrations, and high TOC percentages also suggest anoxic bottom waters. On a regional scale, there are many similarities between the Barnett mudrocks of the southern FWB and those of the northern FWB. The general lithofacies identified are similar and the sedimentary processes acted on Barnett strata in both the northern and southern FWB. Major differences include the much more common occurrence of radiolarians in the northern FWB and the less frequent occurrence of phosphate grains (Papazis, 2005; Loucks and Ruppel, 2007), as well as increased clay mineral abundances in the southern FWB (Figure 29; data from northern FWB from Loucks and Ruppel, 2007). These differences suggest that the Barnett mudrocks of the southern FWB are more proximal to a shoreline and the Barnett mudrocks of the northern FWB are more distal to a shoreline.

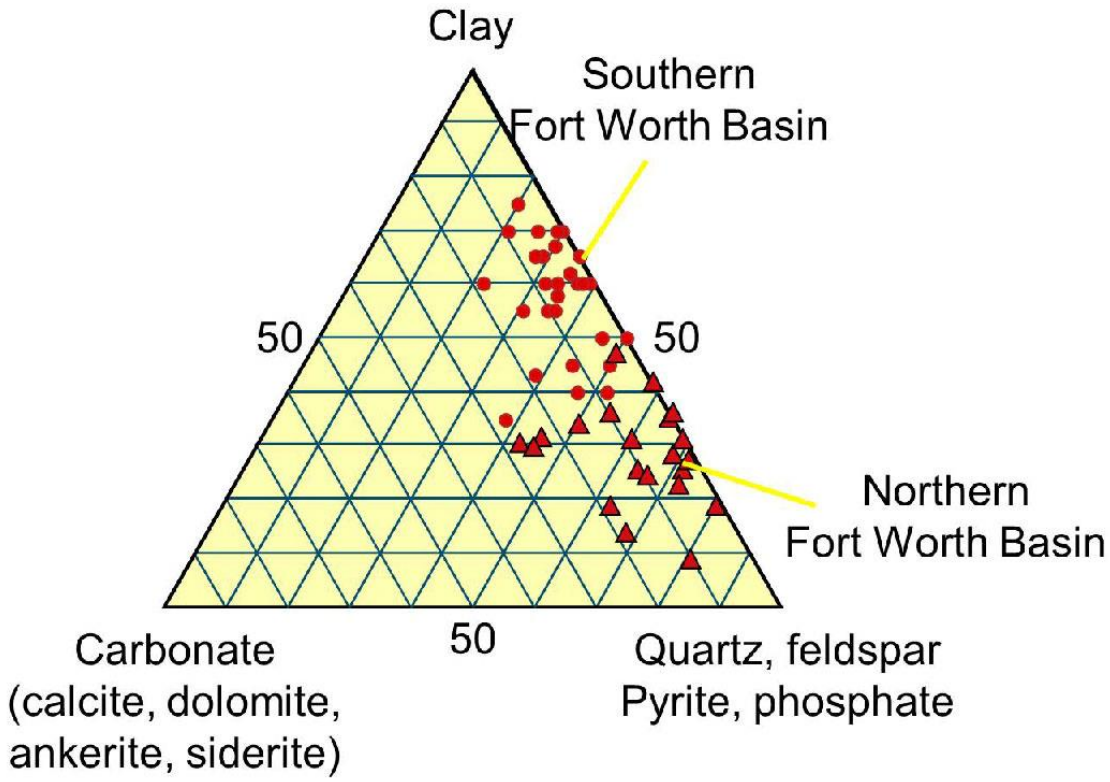

Figure 29: XRD analysis comparing the clay mineral abundances of the northern and southern FWB.

In addition to these differences the northern FWB shows an increase in pyrite framboids (Loucks and Ruppel, 2007) compared to the southern FWB (pyrite abundance by facies in northern FWB vs. southern FWB: (1) siliceous mudstone facies: 9.4% vs. 3.8%, (2) skeletal packstone facies: 10.5% vs. 2.3%, and (3) carbonate concretion: 8.5% vs. 0.5%). The fine pyrite framboids found in the northern FWB Barnett strata are attributed to precipitation in a euxinic water column (Wilkin et al., 1997) and settling to the sea bottom (Loucks and Ruppel, 2007), the lower abundance in the southern FWB suggests an anoxic, rather than euxinic, water column. The longer deep-water renewal times of the northern FWB (8,000 to 20,000 years; Rowe et al. 2008) compared to the southern FWB (1,400 years; Hoelke, 2011) support a less restricted water mass in the southern FWB. These lines of evidence indicate that the waters of the southern FWB were less restricted than the waters of the northern FWB and indicate anoxic bottom-waters, rather than the more restricted euxinic bottom-waters in the northern FWB.

Monroe (2009) mapped the Barnett Formation in the southern FWB using 171 wells from Johnson, Hill, Hood, and Somervell, and Bosque Counties TX and used the phosphatic intervals to correlate cycles in the Barnett Formation. The characteristics identified from wireline logs and thin section observations subdivided the Barnett into three cycles deposited in an aggradational stacking pattern and identified a phosphatic and glauconite rich condensed zone at the top of the formation as the maximum flooding surface. The wireline logs used in Monroe (2009) support the subdivision of the Barnett into lower, middle, and upper units made in this study using the phosphatic packstone, phosphatic glauconitic lime packstone, and XRF clay proxy curves.

CONCLUSION

The Mississippian Barnett Formation in the southern FWB is composed of four lithofacies: (1) siliceous mudstone, (2) calcareous siliceous mudstone, (3) skeletal packstone, and (4) phosphatic packstone to grainstone. Also noted are carbonate concretions and bedding-parallel fibrous calcite beef veins exhibiting cone-in-cone structures. The Pennsylvanian phosphatic glauconitic lime packstone facies marks the transition from the deposition of the aggradational Mississippian Barnett mudrocks to the deposition of the progradational Pennsylvanian Marble Falls mudrocks.

The Barnett Formation was deposited in a foreland basin that was poorly connected to the open ocean and had a stratified water column. Phosphogenesis occurred throughout Barnett strata deposition. The laminated sediments, high organic matter preservation, diagenetic pyrite framboids and rhombs as well as carbonate concretions, and the lack of infauna all indicate anoxic bottom waters throughout its deposition. The rare bioturbation is confined to the basal calcareous siliceous mudstone facies and is attributed to oxygen transport into the basin by gravity flow processes. The phosphatic packstone facies as well as the starved ripples observed throughout the section are indicative of reworked strata *via* bottom-water currents. Grain flocculation in the shallower water column is interpreted to have contributed to sediment deposition.

Deposition of the strata is largely a result of dilute turbidites and other gravity flow processes that transported argillaceous and terrigenous sediments from the structural highs bounding the basin. The consistently fine grain size supports the concept that the sediment was transported for a long distance before reaching the FWB, or fine-grained sediment sources were available. The skeletal material and the phosphate grains were sourced from the adjacent Chappel Shelf by gravity flows. Hemipelagic and pelagic

sedimentation expressed in the sediment by peloids and rare radiolarians, contributed sediment from the oxygenated mixed layer of the water column.

In the southern FWB the Barnett Formation was deposited over inherited basin topography related to the karsting of the Ordovician Ellenburger Group and syndepositional fault movement reacting to the tectonic forces generated by the approach of the Gondwanna towards Laurussia. Strata thickening in the graben structures, as well as offset of the phosphatic packstone facies provide some evidence of the inherited basin topography.

The Barnett Formation was deposited during a long-term, second-order sea-level rise. The phosphatic packstone intervals used to subdivide the Barnett strata and the phosphatic glauconitic lime packstone unit are interpreted as cycle tops and the phosphatic glauconitic lime packstone is additionally interpreted as the maximum flooding surface. To the west of the Llano Uplift the Barnett strata have been eroded, along with the lower Marble Falls, as a result of horst activation and a Pennsylvanian glacioeustatic sea-level fall.

The present study was undertaken to complete the depositional model of Barnett strata in the FWB of north-central Texas by investigating the strata in the southern FWB and comparing it to the strata of the northern FWB. A depositional model was presented that incorporated the vertical and lateral lithofacies variability observed in cores, thin sections, and organic and inorganic geochemical results. The interpretations presented in the present study can be applied to other areas of the basin to better understand the regional depositional history of the Barnett Formation.

Appendix A – TOC Data

Godfrey E-8-1			
Depth (ft.)	% TOC	Depth (ft.)	% TOC
2353.5	1.88	2394.0	11.99
2354.5	11.88	2395.0	3.42
2355.5	4.55	2396.0	6.02
2356.5	5.40	2397.0	5.57
2357.5	4.57	2398.0	3.83
2358.5	4.14	2399.0	2.32
2359.5	2.67	2399.9	2.56
2360.5	4.93	2400.9	8.68
2361.5	5.90	2401.8	2.10
2362.0	6.75	2402.8	1.31
2363.5	5.93	2403.7	1.52
2364.3	6.33	2404.7	5.15
2365.0	4.60	2405.6	4.28
2365.8	5.60	2406.6	5.48
2366.5	5.57	2407.5	1.07
2367.3	2.78	2408.5	5.59
2368.0	3.62	2409.5	3.58
2368.8	4.55	2410.5	2.93
2369.5	2.76	2411.5	5.31
2370.3	9.30	2412.5	2.30
2371.0	6.01	2413.5	2.94
2372.0	6.98	2414.5	3.62
2373.0	7.03	2415.5	3.12
2374.0	6.86	2416.5	4.84
2375.0	5.12	2417.5	3.94
2376.0	5.72	2418.5	4.52
2377.0	5.49	2419.4	2.68
2378.0	5.33	2420.4	4.13
2379.0	1.39	2421.3	3.91
2380.0	4.82	2422.3	3.39
2381.0	4.22	2423.2	3.15
2381.2	4.66	2424.2	2.68
2382.4	4.97	2425.1	2.57
2383.1	4.65	2426.1	4.25
2383.8	4.06	2427.0	3.90
2384.5	3.96	2428.0	3.40
2385.2	4.31	2428.9	3.69
2385.9	4.13	2429.9	4.11
2386.6	0.21	2430.8	4.29
2387.3	3.97	2431.8	2.55
2388.0	3.40	2432.7	4.23
2389.0	4.00	2433.7	4.05
2390.0	9.99	2434.6	4.33
2391.0	3.51	2435.6	2.86
2391.5	0.97	2436.5	1.43
2392.0	3.77	2437.5	3.96
2393.0	2.80	2438.5	3.36

Petty D-6-1					
Depth (ft.)	% TOC	Depth (ft.)	% TOC	Depth (ft.)	% TOC
1673.0	3.00	1713.0	5.79	1753.5	4.22
1673.0	5.98	1713.9	5.64	1754.5	5.63
1674.0	1.51	1714.8	3.57	1755.4	3.27
1674.0	5.39	1715.7	4.30	1756.3	2.05
1675.0	2.27	1716.6	3.71	1757.2	2.50
1676.0	3.92	1717.5	3.48	1758.1	3.91
1676.0	5.07	1718.4	4.88	1759.0	2.54
1677.0	4.28	1719.3	2.71	1759.9	2.86
1678.0	5.22	1720.2	3.62	1760.8	3.53
1679.0	4.55	1721.1	3.19	1761.7	4.88
1680.0	4.16	1722.0	1.63	1762.6	3.20
1681.0	6.34	1722.0	2.18	1763.5	2.87
1682.0	2.17	1722.9	3.33	1764.5	2.28
1683.0	4.97	1723.1	5.37	1765.5	2.46
1684.0	7.15	1723.5	6.53	1766.5	1.90
1685.0	3.83	1723.8	9.58	1767.5	3.61
1686.0	6.64	1725.6	2.76	1768.5	3.64
1687.0	4.55	1726.5	3.05	1769.5	3.79
1687.0	2.95	1727.4	3.63	1770.5	5.99
1687.0	5.96	1728.3	5.04	1771.5	3.72
1688.0	7.22	1729.2	5.21	1772.5	1.51
1689.0	6.70	1730.3	3.03	1773.4	1.68
1690.0	7.25	1730.4	5.46	1774.3	2.54
1691.0	7.42	1731.1	5.57	1775.2	5.70
1692.0	5.34	1732.0	4.39	1776.1	5.04
1693.0	4.96	1732.9	6.21	1777.0	2.69
1694.0	5.40	1733.8	4.58	1777.9	3.14
1695.0	2.49	1734.7	4.15	1778.8	3.63
1696.0	5.14	1735.5	7.84	1779.7	5.06
1697.0	4.61	1736.4	4.45	1780.6	6.32
1698.0	5.05	1737.3	8.72	1781.5	2.73
1698.0	4.80	1738.2	3.02	1782.5	5.60
1699.0	2.86	1739.1	2.91	1783.5	5.68
1700.0	2.29	1740.0	5.46	1784.5	0.52
1701.0	4.74	1740.9	4.22	1785.5	7.78
1702.0	4.96	1741.8	5.20	1786.5	0.79
1703.0	4.82	1742.7	3.68	1787.5	1.93
1703.0	4.50	1743.6	4.71	1788.5	2.15
1703.0	4.13	1744.5	2.62	1789.5	1.64
1704.0	4.28	1745.5	3.78	1790.5	2.89
1706.0	3.70	1746.5	5.41		
1707.0	3.34	1747.5	4.71		
1708.5	2.29	1748.5	4.00		
1709.4	2.52	1749.5	4.21		
1710.3	2.08	1750.5	3.90		
1711.2	4.79	1751.5	4.14		
1712.1	3.78	1752.5	4.47		

Table A1: TOC data (wt%) from Hoelke (2011).

Locker B-2-1					
Depth (ft.)	% TOC	Depth (ft.)	% TOC	Depth (ft.)	% TOC
555.1	2.23	595.3	4.14	635.8	1.07
556.0	2.30	596.2	3.31	636.3	5.35
556.3	5.81	597.2	7.22	637.1	6.52
557.5	0.79	598.4	6.82		
558.2	0.95	599.1	1.64		
559.0	5.45	599.6	8.14		
559.7	5.29	600.3	3.86		
560.4	6.86	601.1	4.49		
561.2	4.17	601.4	1.91		
562.4	6.17	602.2	3.02		
563.2	7.58	603.1	6.49		
564.1	5.61	604.0	4.82		
565.1	6.06	604.0	7.92		
565.5	2.61	604.4	5.04		
566.7	3.48	605.1	10.33		
567.6	5.05	606.1	4.08		
568.5	5.31	607.3	4.26		
570.2	4.71	608.1	2.06		
570.8	7.22	609.1	2.50		
571.6	8.51	610.1	3.58		
573.1	3.65	611.2	4.88		
574.4	3.81	612.1	5.88		
575.4	5.66	613.1	3.91		
576.5	6.10	613.6	4.35		
577.5	7.85	614.1	5.28		
578.8	6.10	615.0	5.21		
579.6	6.24	616.6	3.95		
580.5	4.94	617.1	2.65		
581.3	5.58	618.1	2.49		
581.6	1.81	619.2	3.67		
582.4	6.50	620.2	2.77		
583.2	5.79	621.2	2.88		
584.7	7.07	622.2	3.55		
585.1	6.47	623.0	2.14		
585.6	6.49	624.1	3.10		
586.3	6.49	625.1	2.97		
587.3	5.65	626.2	3.05		
587.6	0.51	627.1	3.38		
587.9	6.42	628.1	4.83		
588.6	5.48	629.1	1.70		
589.1	3.26	630.1	6.78		
590.0	0.31	631.1	5.20		
592.1	2.39	632.1	1.71		
592.7	7.85	632.5	0.90		
593.3	5.66	633.1	3.69		
594.1	2.55	634.0	4.43		
594.7	8.37	635.3	5.84		

Lee C-5-1	
Depth (ft.)	% TOC
1231.5	3.03
1233.1	4.39
1235.0	4.81
1237.5	5.59
1240.0	4.09
1244.0	6.57
1245.7	4.83
1247.2	7.84
1248.5	4.53
1250.0	8.09
1251.0	8.67
1253.0	5.60
1255.6	6.08
1258.0	5.69
1262.8	5.17
1265.5	4.43
1268.5	0.93
1270.2	7.36
1271.7	5.28
1273.5	6.14
1275.0	3.06
1276.6	4.72
1278.2	5.08
1280.2	4.86
1283.0	9.21
1284.0	1.30
1286.0	4.77
1287.6	6.24
1289.8	3.45
1291.6	4.38
1294.0	5.14
1296.6	4.25
1299.0	5.57
1302.0	3.29
1304.8	9.27
1308.7	3.39

Table A1 continued: TOC data (wt%) from Hoelke (2011).

Well Name	Well Code	Depth (ft)	LECO TOC
Lee	C-5-1	1240	4.78
Lee	C-5-1	1250	7.88
Lee	C-5-1	1258	4.60
Lee	C-5-1	1263	4.20
Lee	C-5-1	1265	4.55
Lee	C-5-1	1278	8.19
Lee	C-5-1	1281	5.52
Lee	C-5-1	1289	5.86
Lee	C-5-1	1301	5.42
Lee	C-5-1	1305	1.60
Lee	C-5-1	1306	1.66
Petty	D-6-1	1675	6.21
Petty	D-6-1	1678	5.56
Petty	D-6-1	1685	5.24
Petty	D-6-1	1715	9.00
Petty	D-6-1	1720	8.76
Petty	D-6-1	1735	2.95
Petty	D-6-1	1746	3.80
Petty	D-6-1	1769	3.82
Petty	D-6-1	1778	5.62
Scoggins*	A-2-1	767	7.57
Scoggins*	A-2-1	789	3.89
Scoggins*	A-2-1	793	4.21
Locker*	B-2-1	603.1	3.75
Locker*	B-2-1	628.25	7.07
Beck*	C-4-1	1254.33	3.75
Beck*	C-4-1	1270	3.08

Table A2: Leco TOC data (wt%). * indicate data from Reed and Loucks, 2015.

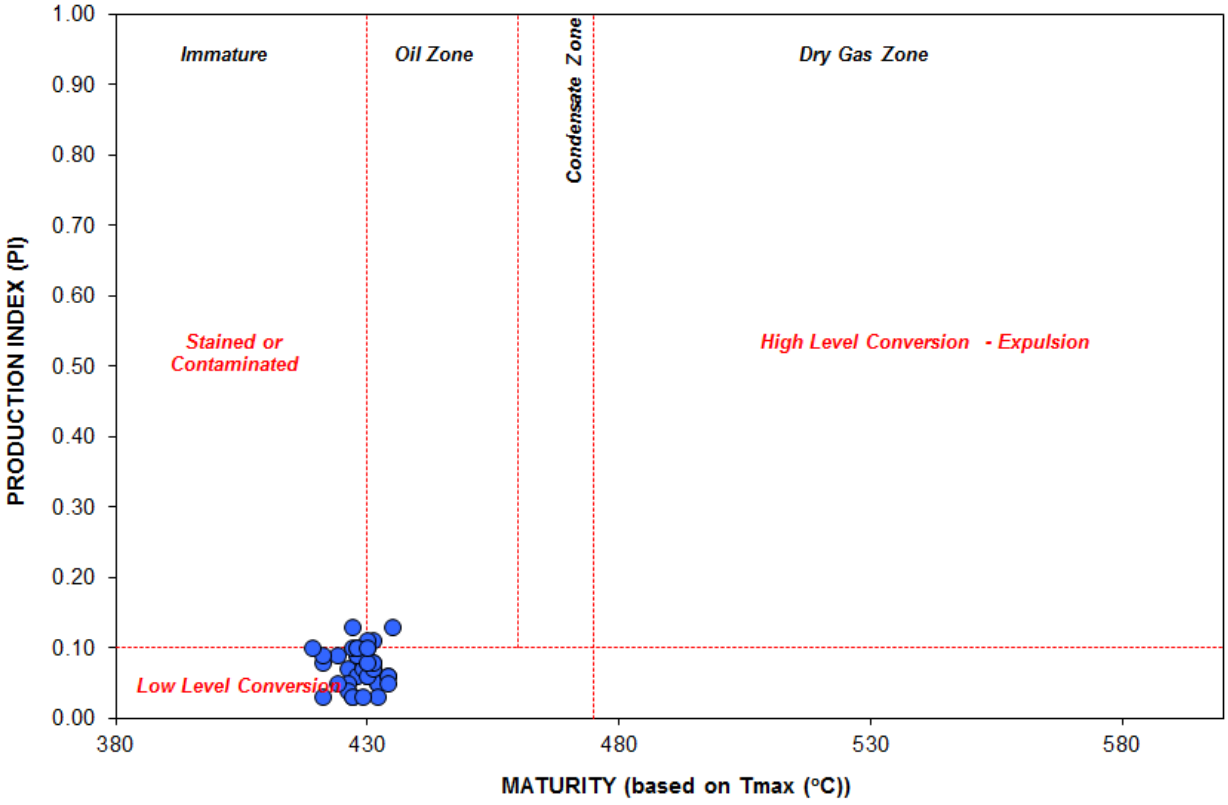

Table A3: Rock-Eval pyrolysis of samples in Table A2 showing the Barnett Formation in the southern FWB is thermally immature.

Appendix B – Core Descriptions

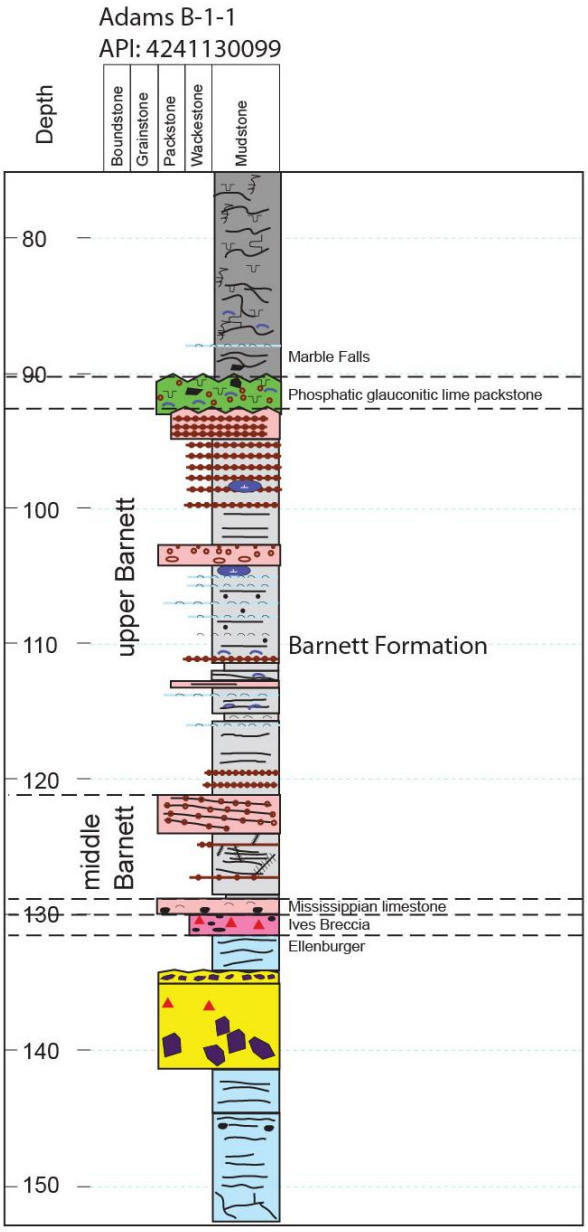

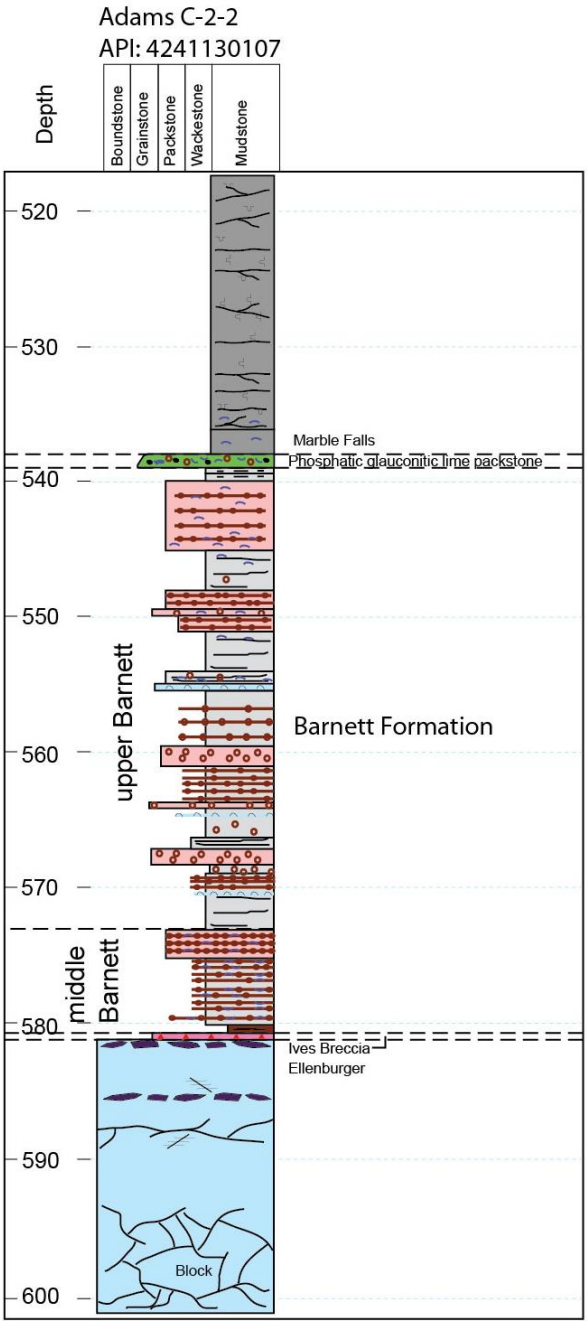
Adams C-2-2
API: 4241130107
Depth
Boundstone
Grainstone
Packstone
Wackestone
Mudstone
520
530
540
550
560
570
580
590
600
Marble Falls
Phosphatic glauconitic lime packstone
upper Barnett
Barnett Formation
middle Barnett
Ives Breccia
Ellenburger
Block

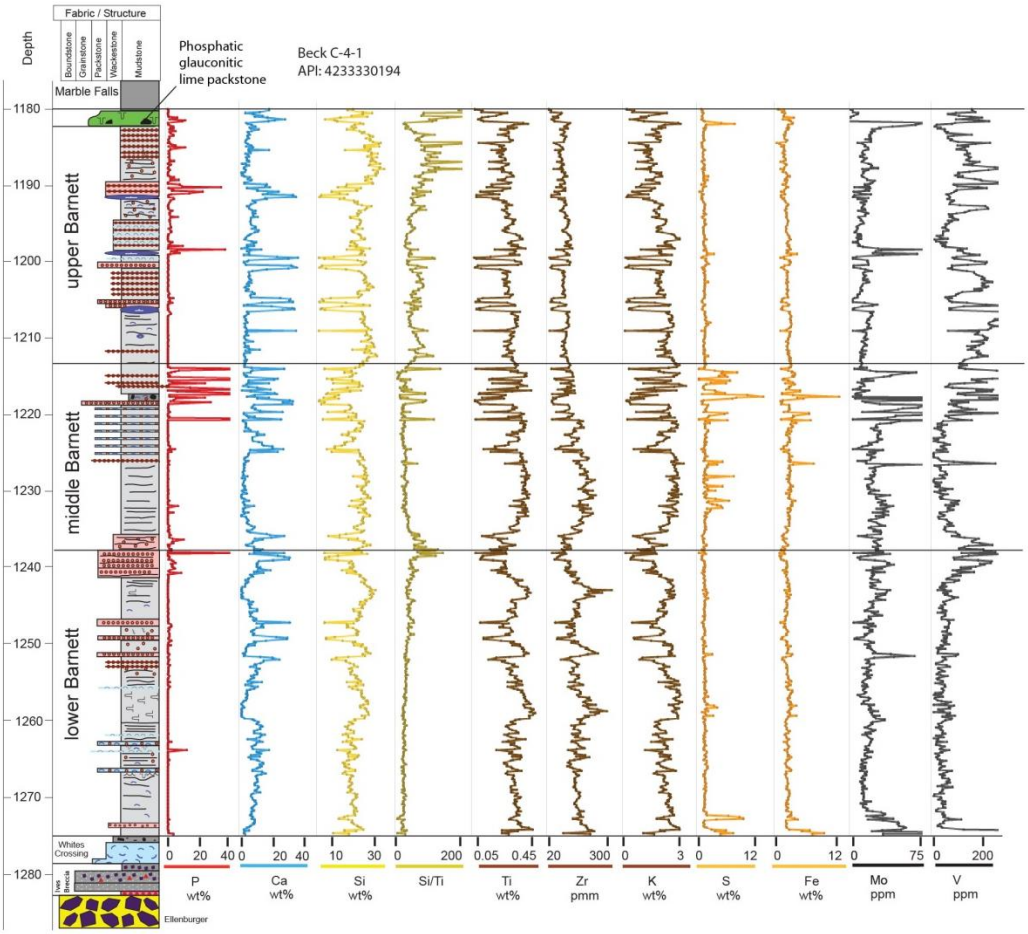
Fabric / Structure
Boundstone
Grainstone
Packstone
Wackestone
Mudstone
Depth
Phosphatic glauconitic lime packstone
Beck C-4-1
API: 4233330194
Marble Falls
upper Barnett
middle Barnett
lower Barnett
Whites Crossing
Ellenburger
1180
1190
1200
1210
1220
1230
1240
1250
1260
1270
1280
0 20 40
P wt%
0 20 40
Ca wt%
10 30
Si wt%
0 200
Si/Ti
0.05 0.45
Ti wt%
20 300
Zr ppm
0 3
K wt%
0 12
S wt%
0 12
Fe wt%
0 75
Mo ppm
0 200
V ppm

Glaze C-2-3
API: 4241130104

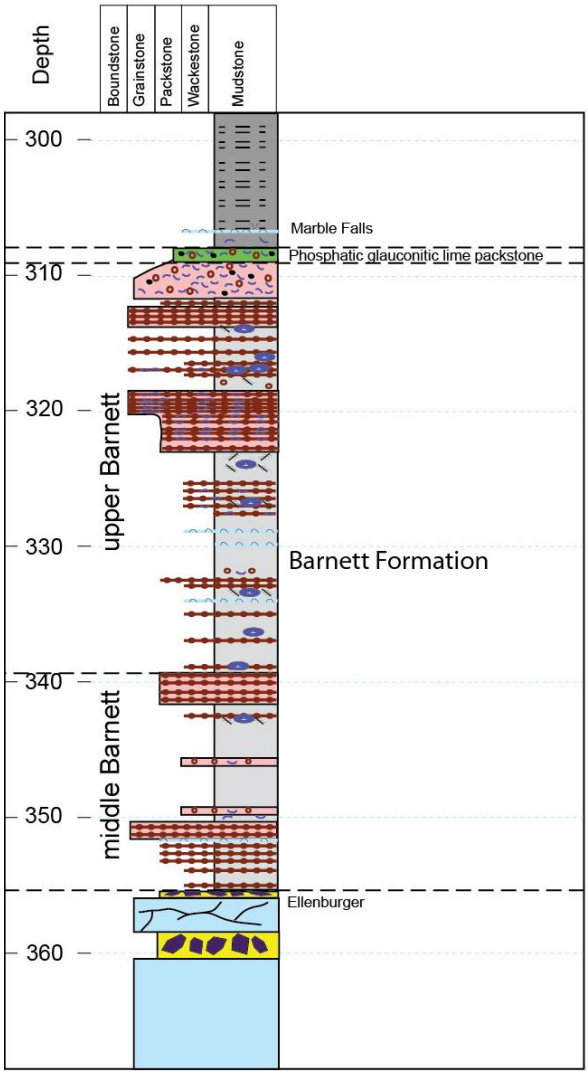

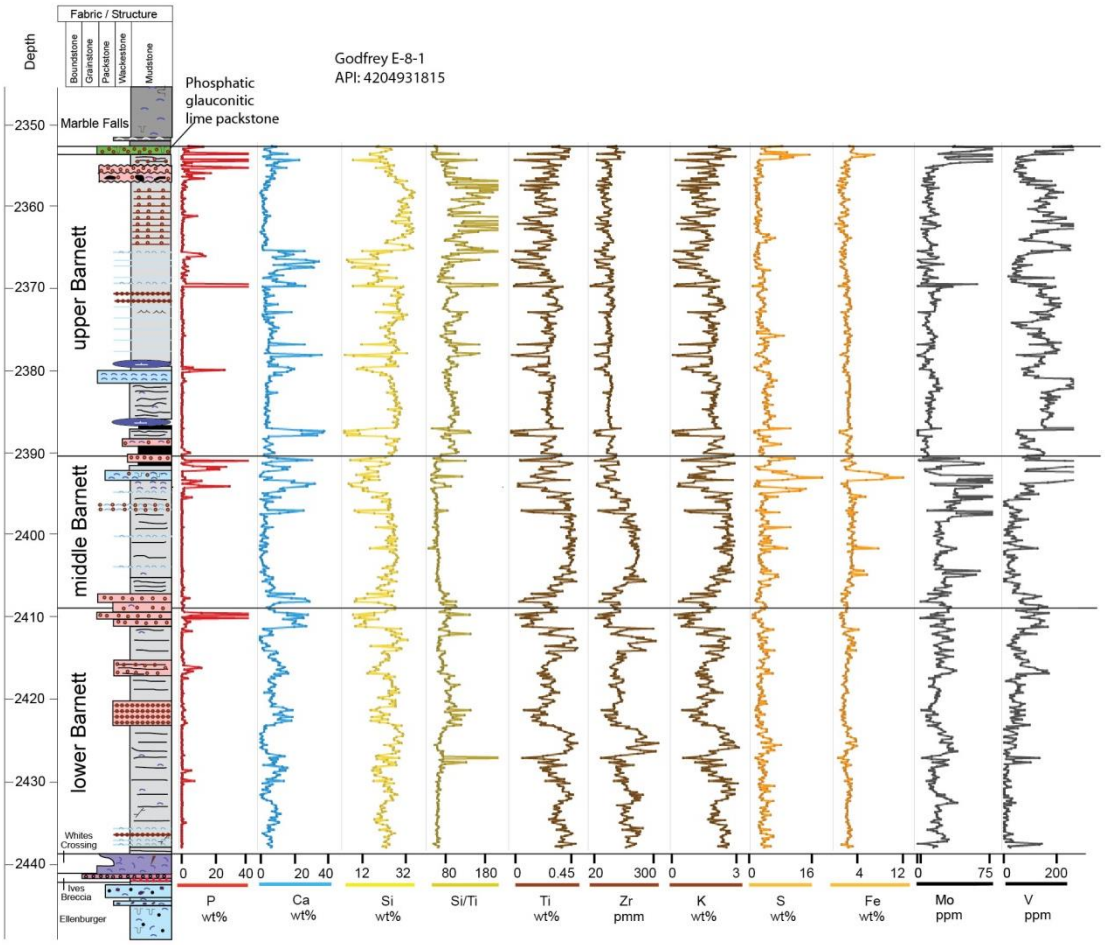
Fabric / Structure
Boundstone
Grainstone
Packstone
Wackestone
Mudstone
Depth
Godfrey E-8-1
API: 4204931815
Phosphatic glauconitic lime packstone
Marble Falls
upper Barnett
middle Barnett
lower Barnett
Whites Crossing
Ives Breccia
Ellenburger
2350
2360
2370
2380
2390
2400
2410
2420
2430
2440
0 20 40
P wt%
0 20 40
Ca wt%
12 32
Si wt%
80 180
Si/Ti
0 0.45
Ti wt%
20 300
Zr pmm
0 3
K wt%
0 16
S wt%
4 12
Fe wt%
0 75
Mo ppm
0 200
V ppm

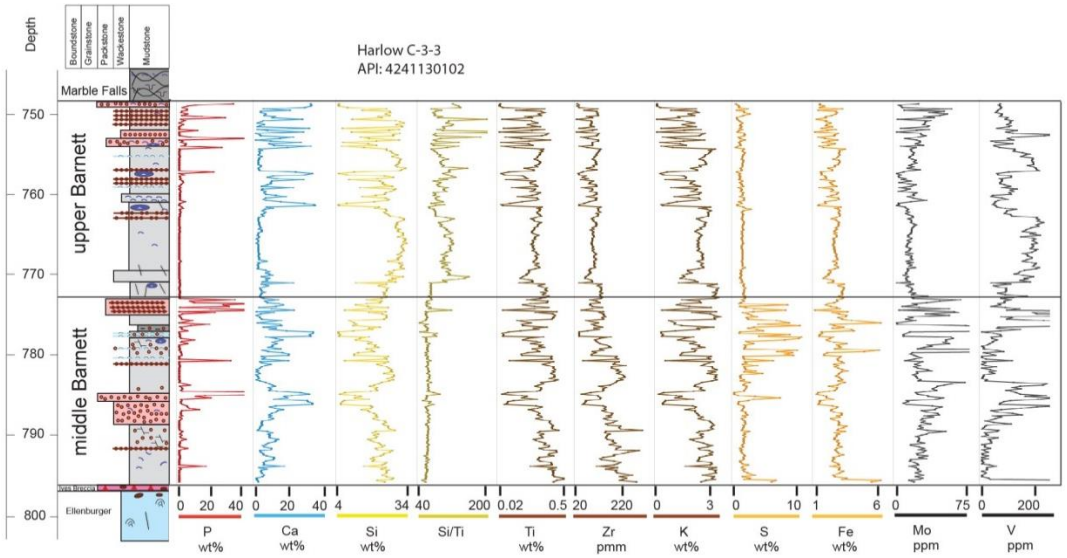
Harlow C-3-3
API: 4241130102
Depth
Boundstone
Grainstone
Packstone
Wackestone
Mudstone
Marble Falls
upper Barnett
middle Barnett
Ellenburger
750
760
770
780
790
800
0 20 40
P wt%
0 20 40
Ca wt%
4 34
Si wt%
40 200
Si/Ti
0.02 0.5
Ti wt%
20 220
Zr pmm
0 3
K wt%
0 10
S wt%
1 6
Fe wt%
0 75
Mo ppm
0 200
V ppm

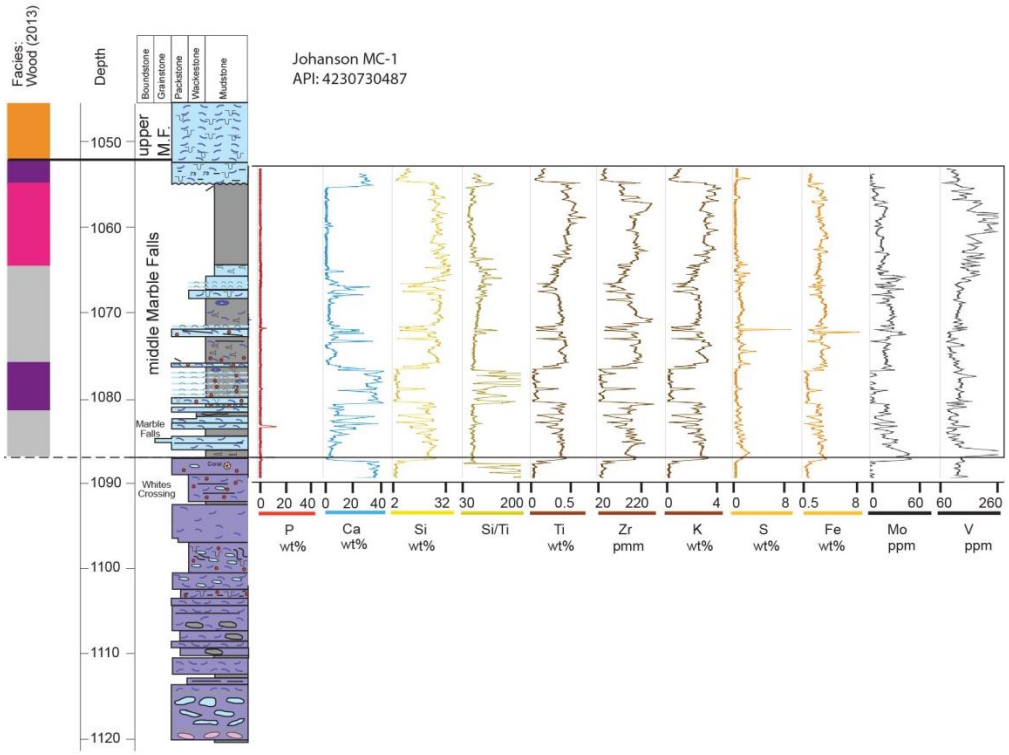
Facies: Wood (2013)
Depth
Boundstone
Grainstone
Packstone
Wackestone
Mudstone
Johanson MC-1
API: 4230730487
upper M.F.
middle Marble Falls
Marble Falls
Whites Crossing
Coral
1050
1060
1070
1080
1090
1100
1110
1120
0 20 40
P wt%
0 20 40
Ca wt%
2 32
Si wt%
30 200
Si/Ti
0 0.5
Ti wt%
20 220
Zr pmm
0 4
K wt%
0 8
S wt%
0.5 8
Fe wt%
0 60
Mo ppm
60 260
V ppm

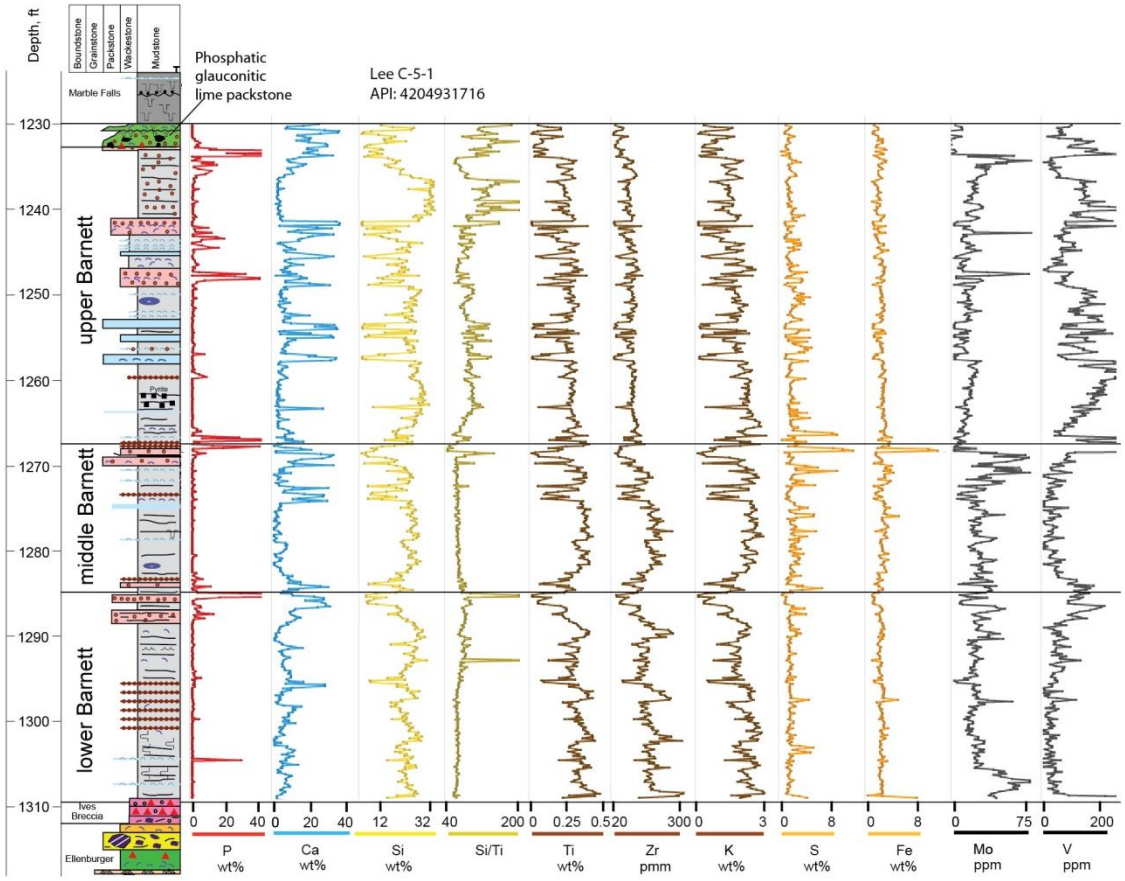
Depth, ft
Boundstone
Grainstone
Packstone
Wackestone
Mudstone
Phosphatic glauconitic lime packstone
Lee C-5-1
API: 4204931716
Marble Falls
upper Barnett
middle Barnett
lower Barnett
Pyrite
Ives Breccia
Ellenburger
1230
1240
1250
1260
1270
1280
1290
1300
1310
0 20 40
P wt%
0 20 40
Ca wt%
12 32
Si wt%
40 200
Si/Ti
0 0.25 0.5
Ti wt%
20 300
Zr pmm
0 3
K wt%
0 8
S wt%
0 8
Fe wt%
0 75
Mo ppm
0 200
V ppm

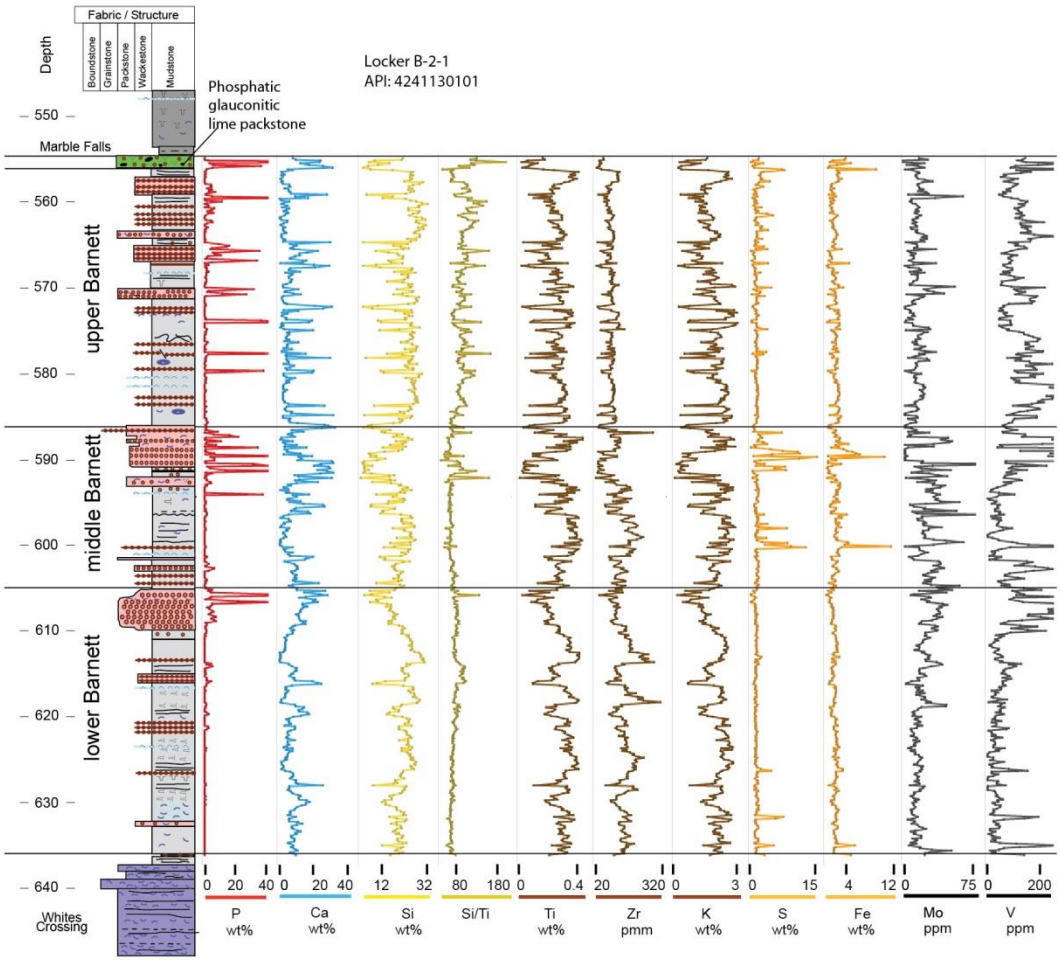
Fabric / Structure
Depth
Boundstone
Grainstone
Packstone
Wackestone
Mudstone
Locker B-2-1
API: 4241130101
Phosphatic glauconitic lime packstone
Marble Falls
upper Barnett
middle Barnett
lower Barnett
Whites Crossing
550
560
570
580
590
600
610
620
630
640
0 20 40
P wt%
0 20 40
Ca wt%
12 32
Si wt%
80 180
Si/Ti
0 0.4
Ti wt%
20 320
Zr ppm
0 3
K wt%
0 15
S wt%
4 12
Fe wt%
0 75
Mo ppm
0 200
V ppm

Moore C-1-1
API: 4241130096

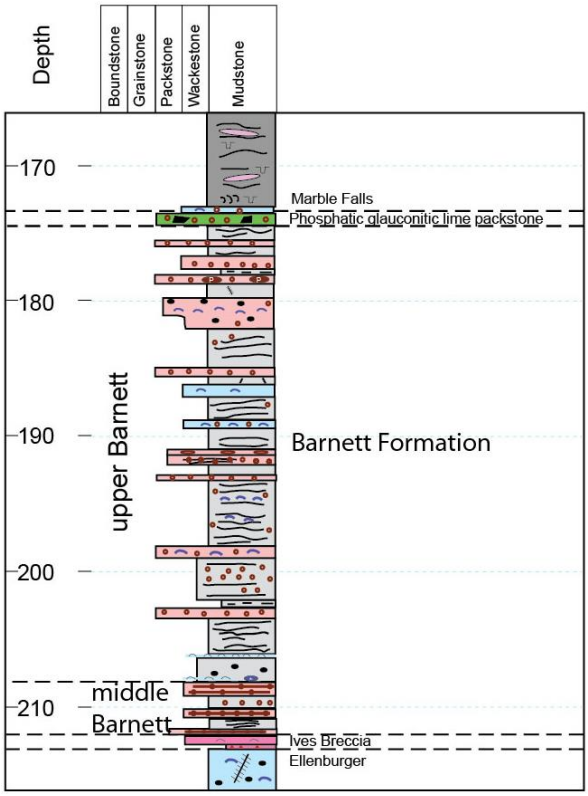

Mullis A-4-1
API: 4204931813

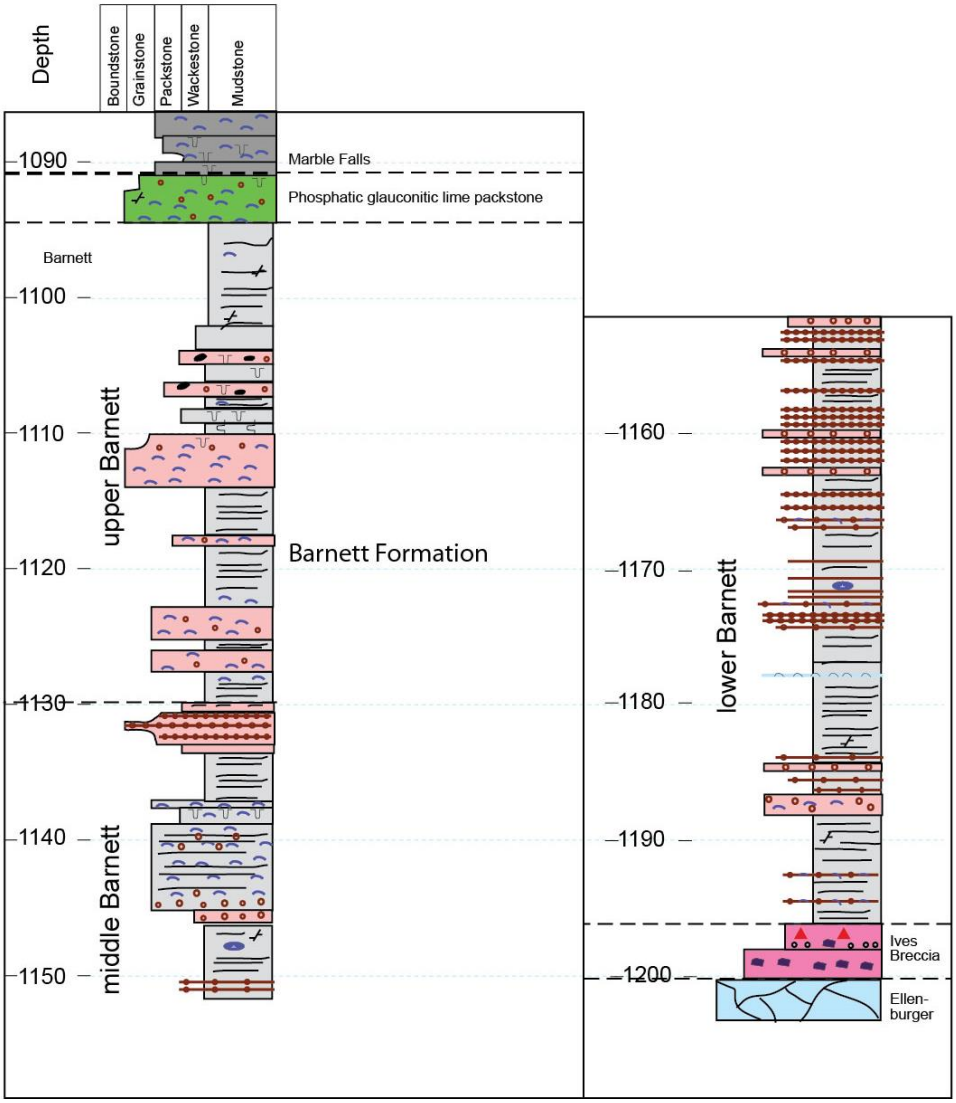

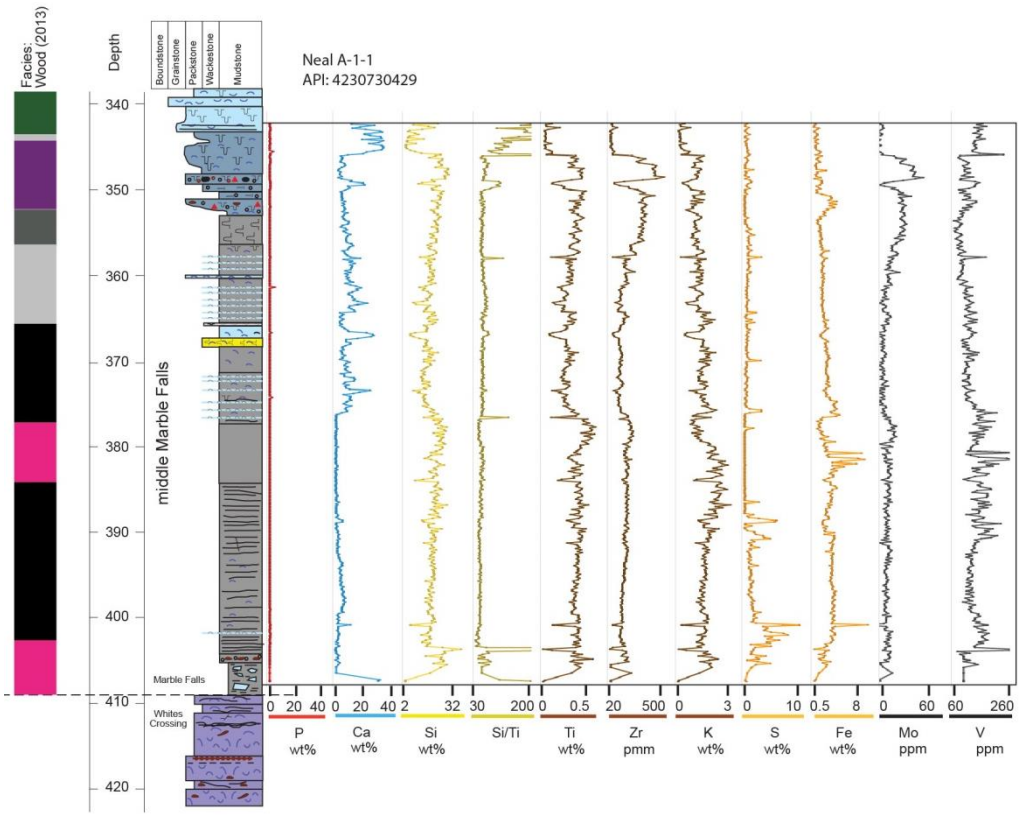
Facies: Wood (2013)
Depth
Boundstone
Grainstone
Packstone
Wackestone
Mudstone
Neal A-1-1
API: 4230730429
middle Marble Falls
Marble Falls
Whites Crossing
340
350
360
370
380
390
400
410
420
0 20 40
P wt%
0 20 40
Ca wt%
2 32
Si wt%
30 200
Si/Ti
0 0.5
Ti wt%
20 500
Zr pmm
0 3
K wt%
0 10
S wt%
0.5 8
Fe wt%
0 60
Mo ppm
60 260
V ppm

Old C-8-1
API: 4204931787

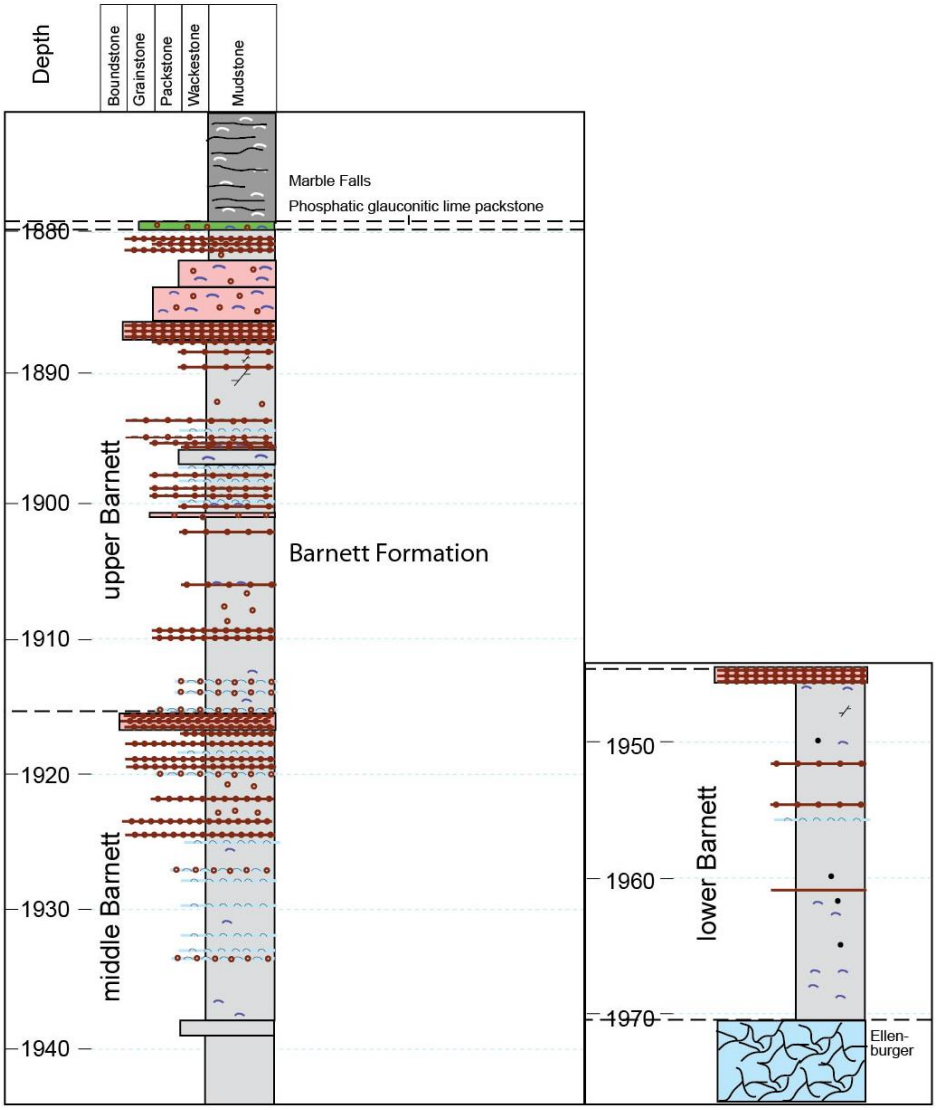

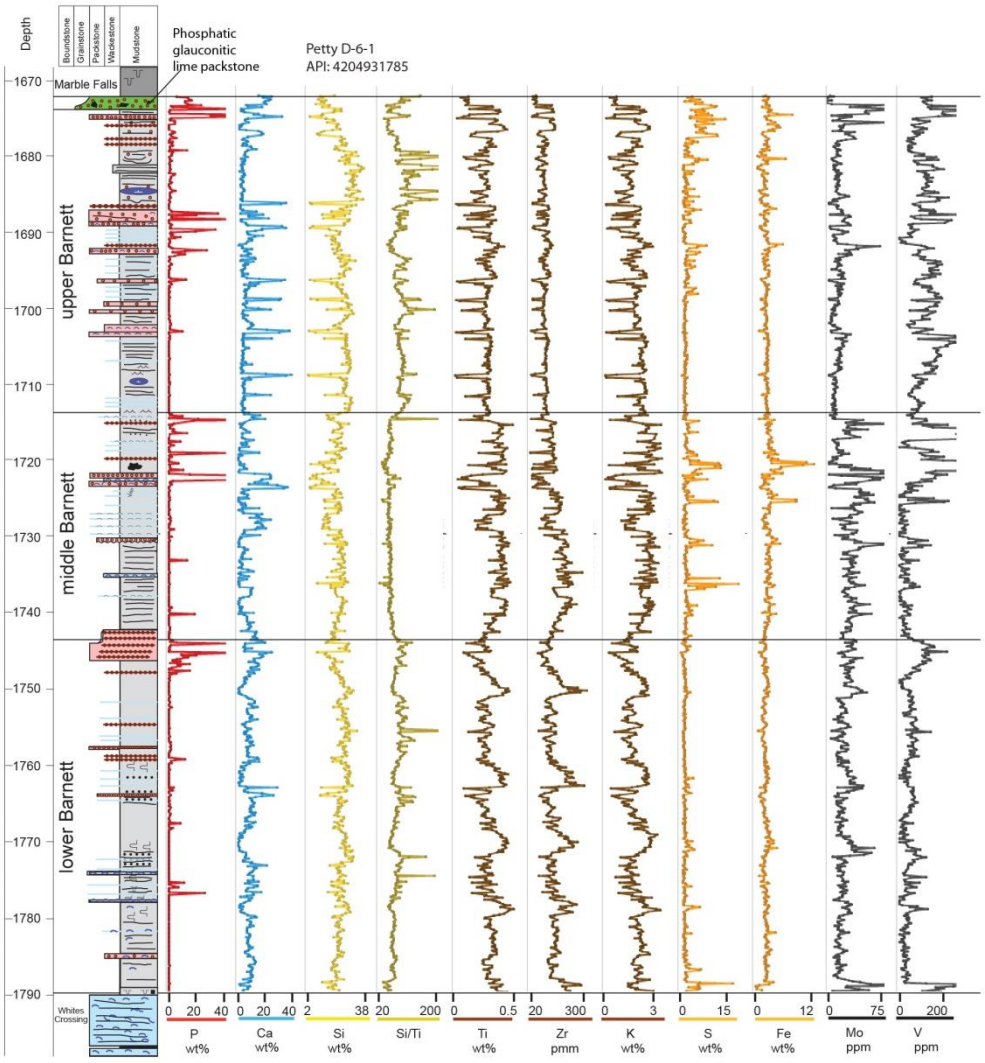
Depth
Boundstone
Grainstone
Packstone
Wackestone
Mudstone
Phosphatic glauconitic lime packstone
Petty D-6-1
API: 4204931785
Marble Falls
upper Barnett
middle Barnett
lower Barnett
Whites Crossing
1670
1680
1690
1700
1710
1720
1730
1740
1750
1760
1770
1780
1790
0 20 40
P wt%
0 20 40
Ca wt%
2 38
Si wt%
20 200
Si/Ti
0 0.5
Ti wt%
20 300
Zr pmm
0 3
K wt%
0 15
S wt%
0 12
Fe wt%
0 75
Mo ppm
0 200
V ppm

Posey B-4-1
API: 4204931786

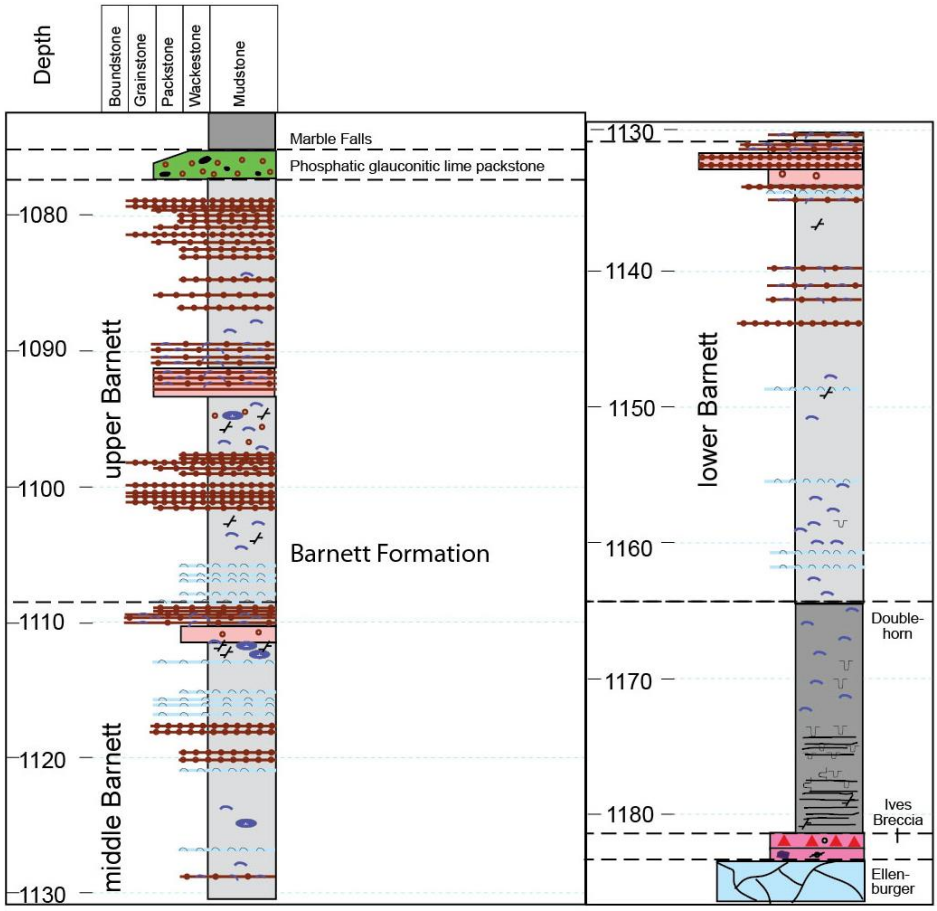

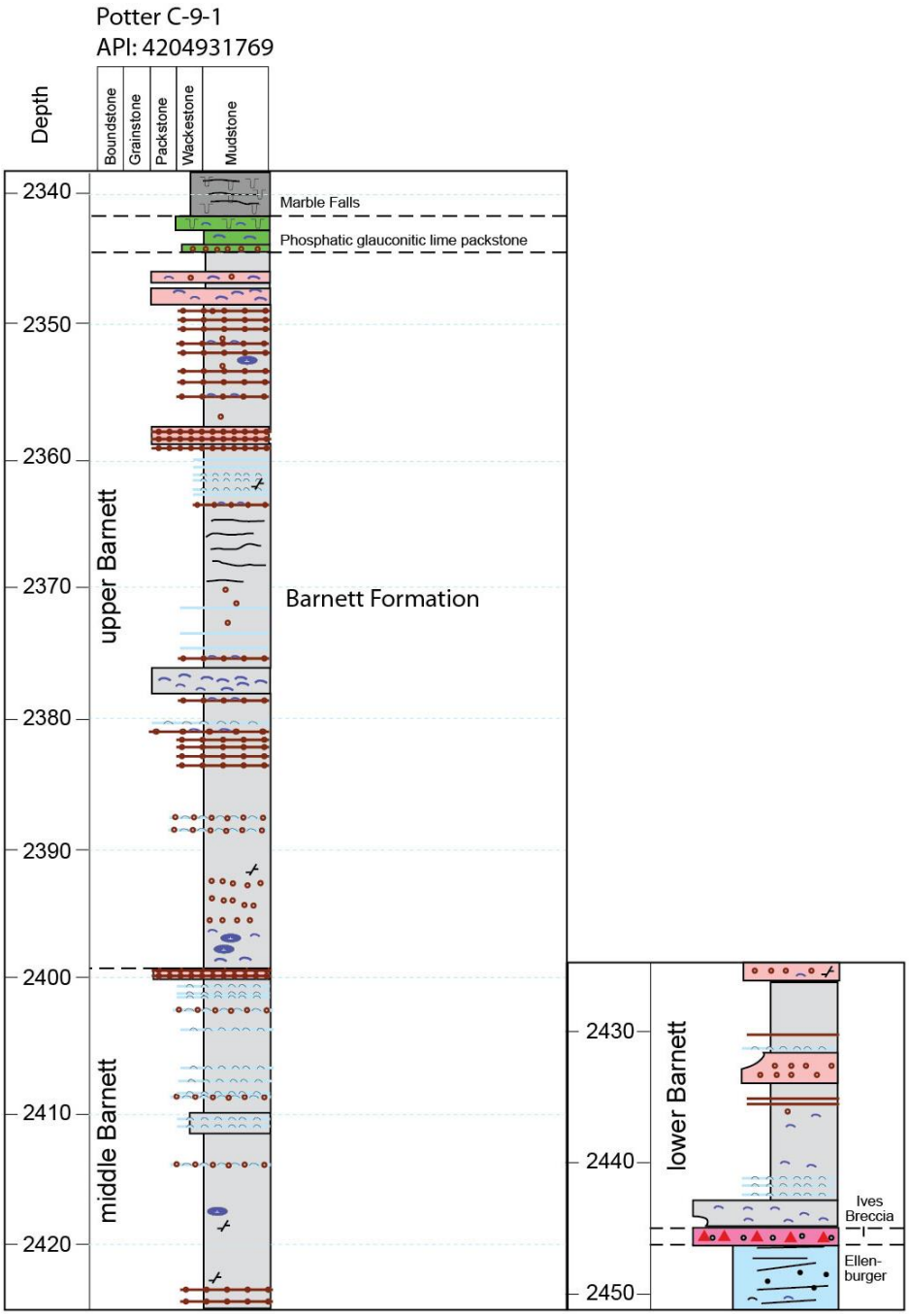
Potter C-9-1
API: 4204931769
Depth
Boundstone
Grainstone
Packstone
Wackestone
Mudstone
2340
2350
2360
2370
2380
2390
2400
2410
2420
Marble Falls
Phosphatic glauconitic lime packstone
upper Barnett
Barnett Formation
middle Barnett
2430
2440
2450
lower Barnett
Ives Breccia
Ellen-burger

Powell B-3-1
API: 4241130097

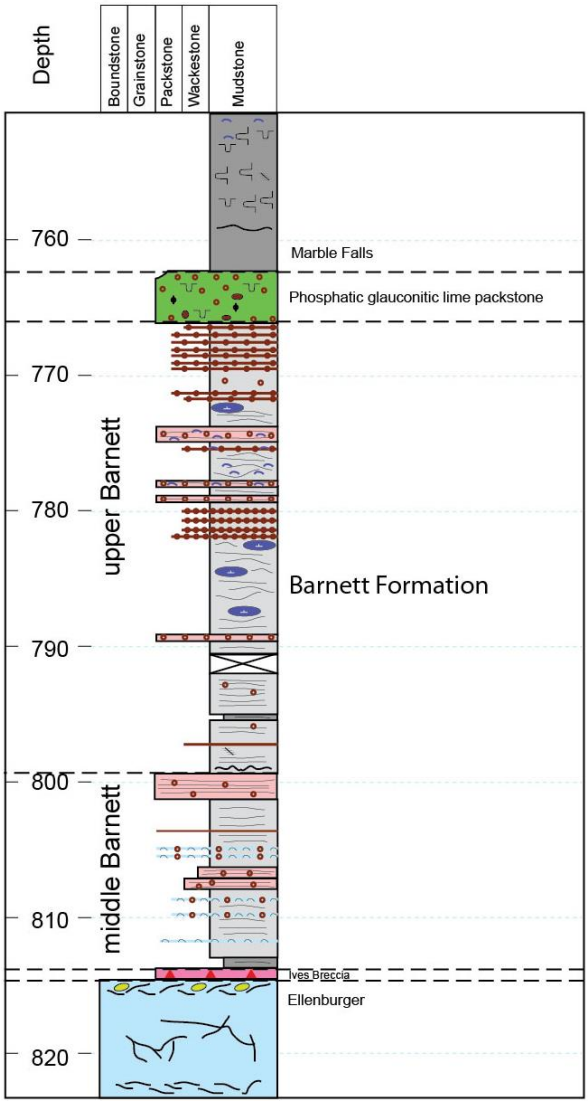

Rasco D-4-1
API: 4233330195

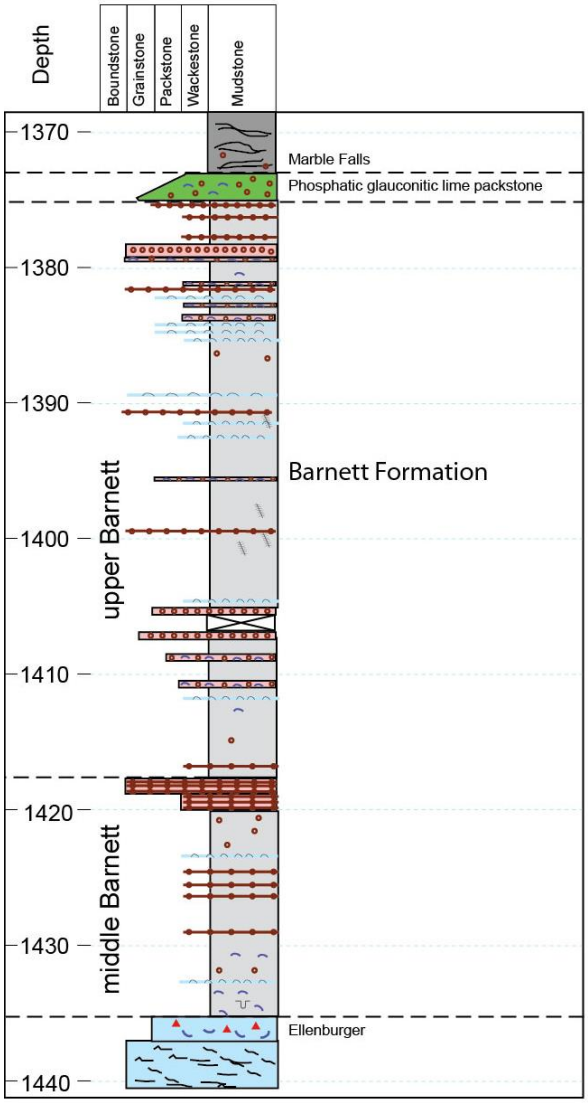

Scoggins A-2-1
API: 4230730447

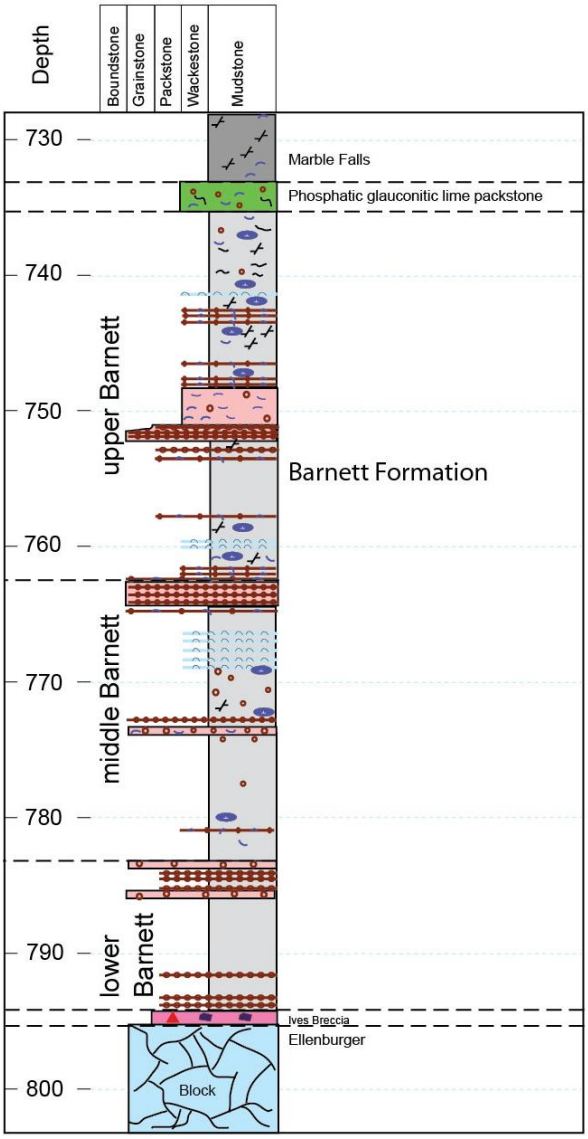

Smith C-2-4
API: 4241130106

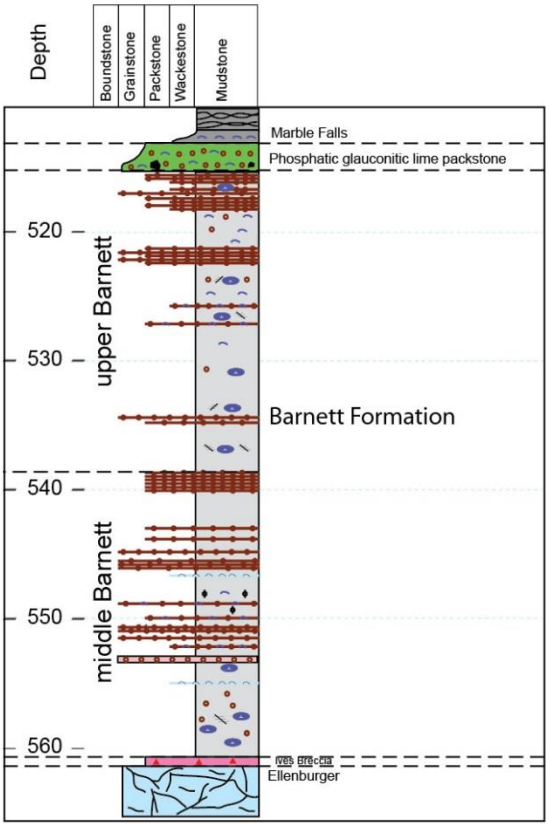

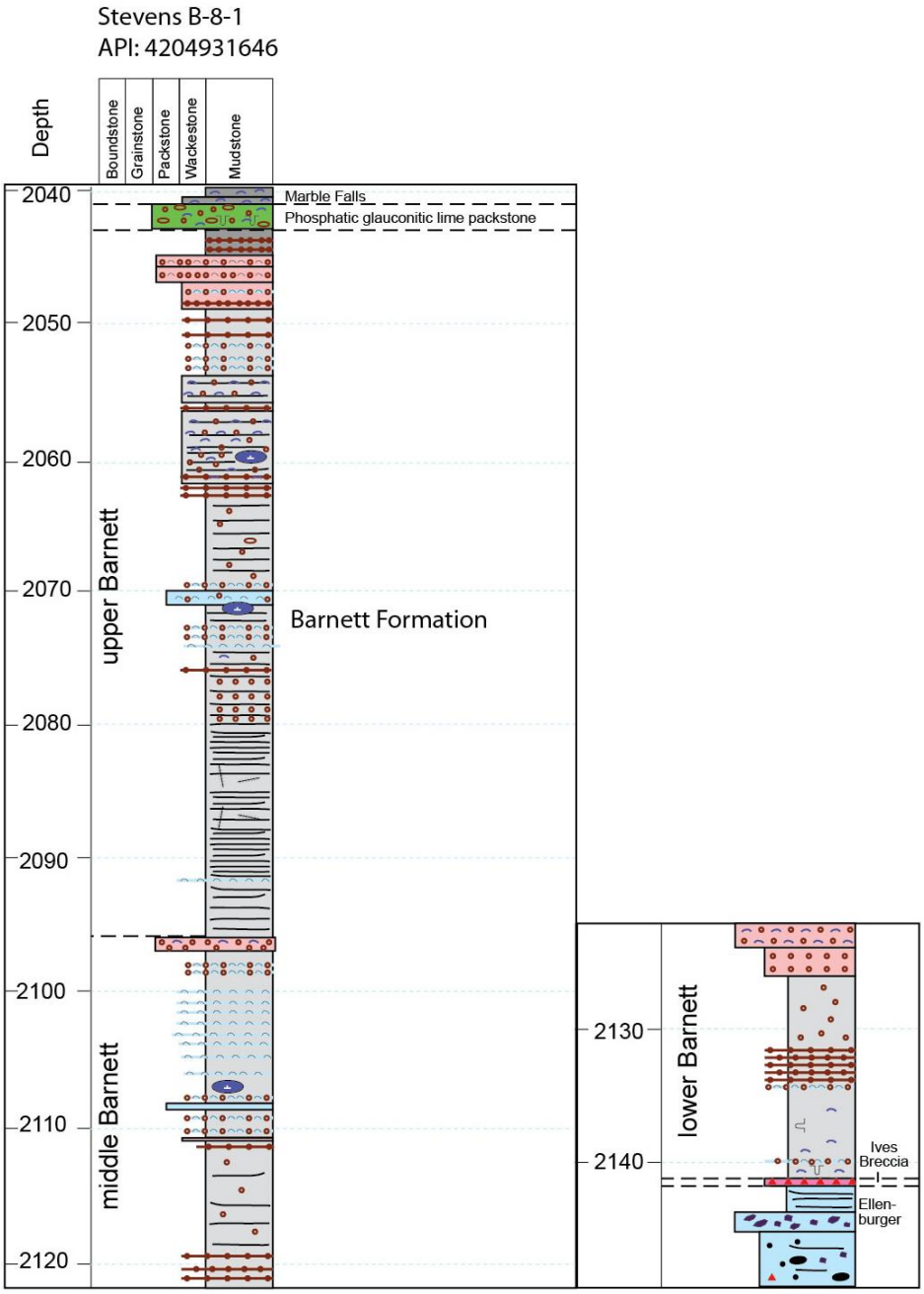
Stevens B-8-1
API: 4204931646
Depth
Boundstone
Grainstone
Packstone
Wackestone
Mudstone
2040
2050
2060
2070
2080
2090
2100
2110
2120
Marble Falls
Phosphatic glauconitic lime packstone
upper Barnett
Barnett Formation
middle Barnett
2130
2140
lower Barnett
Ives Breccia
Ellen-burger

Walker D-1-1
API: 4241130100

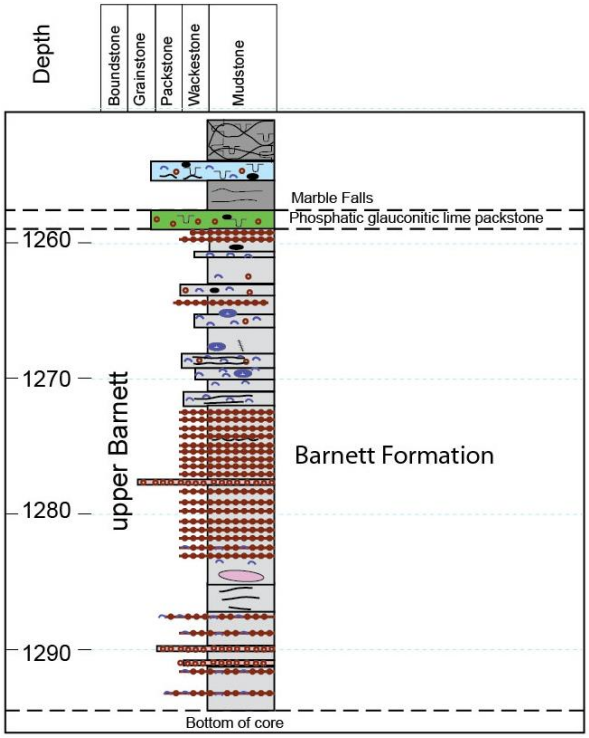

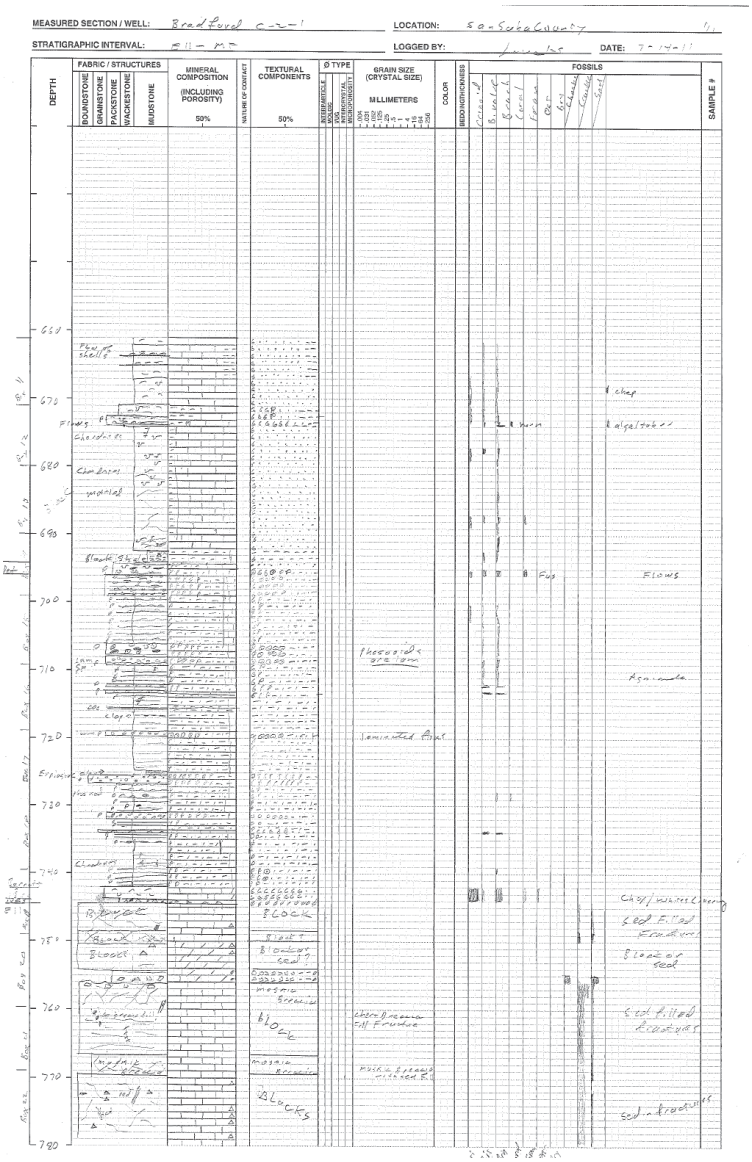
MEASURED SECTION / WELL: Bradford C-2-1
LOCATION: San Juan County
STRATIGRAPHIC INTERVAL: P11 - M7
LOGGED BY:
DATE: 7-14-11
DEPTH
FABRIC / STRUCTURES
BOUNDSTONE
GRAINSTONE
PACKSTONE
WACKESTONE
MUDSTONE
MINERAL COMPOSITION (INCLUDING POROSITY)
50%
NATURE OF CONTACT
TEXTURAL COMPONENTS
50%
Ø TYPE
INTERGRANULAR
VUGS
INTERCRYSTAL
INTRAPARTICLE
GRAIN SIZE (CRYSTAL SIZE)
MILLIMETERS
COLOR
BEDDING THICKNESS
FOSSILS
SAMPLE #
650
660
670
680
690
700
710
720
730
740
750
760
770
780
Flows
Interbedded
Channel
Thrombolite
Stromatolitic Mound
Laminated Algal
Erosional
Flows
Algal mats
Ch3/1 Wanakah
Red E. Ind
Formation
Bloom of
Red
Bloom
Red
Bloom
Red
Massive
Breccia
Block
Chert Nodules
Fill Fracture
Massive
Breccia
Block
Fluvial Filled
Fractures
Sedimentary

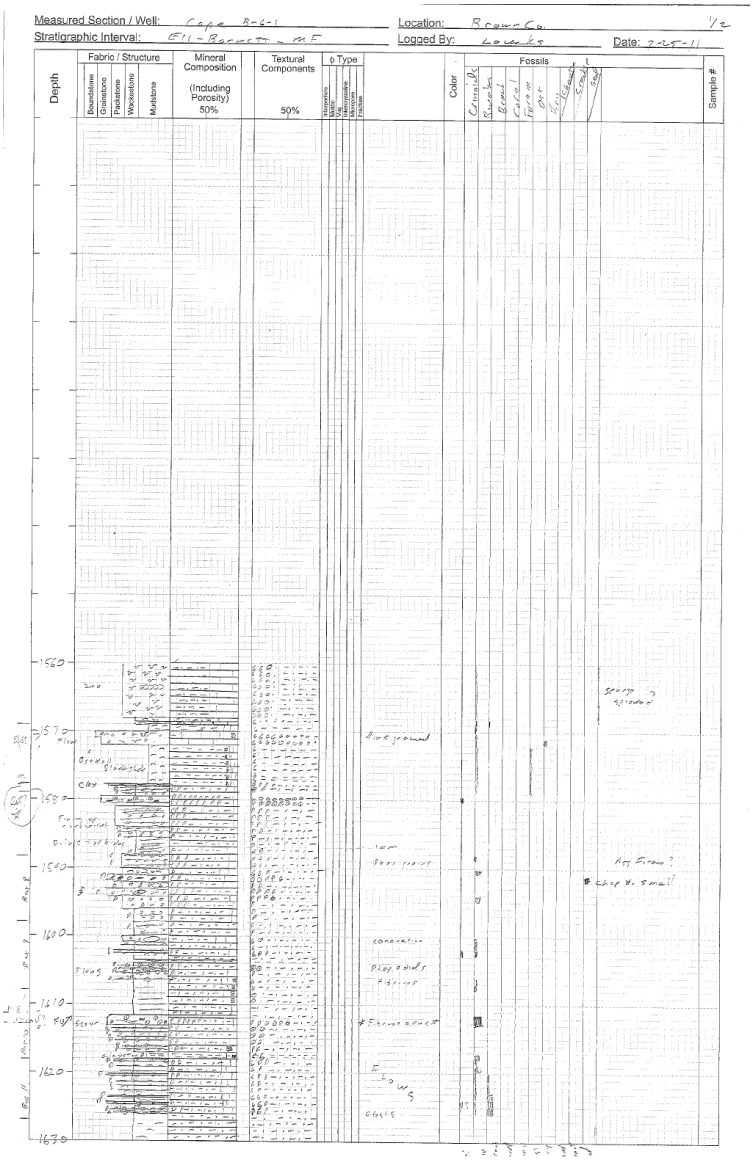
Measured Section / Well: Cape R-6-1
Location: Brown Co.
Stratigraphic Interval: Ft. Bacett - ME
Logged By: Lewis
Date: 7-25-11
Depth
Fabric / Structure
Boundstone
Grainstone
Packstone
Wackestone
Mudstone
Mineral Composition (Including Porosity) 50%
Textural Components 50%
ϕ Type
Vugular
Moldic
Intercrystal
Microvugular
Fracture
Color
Fossils
Sample #
1560
1570
1580
1590
1600
1610
1620
1630

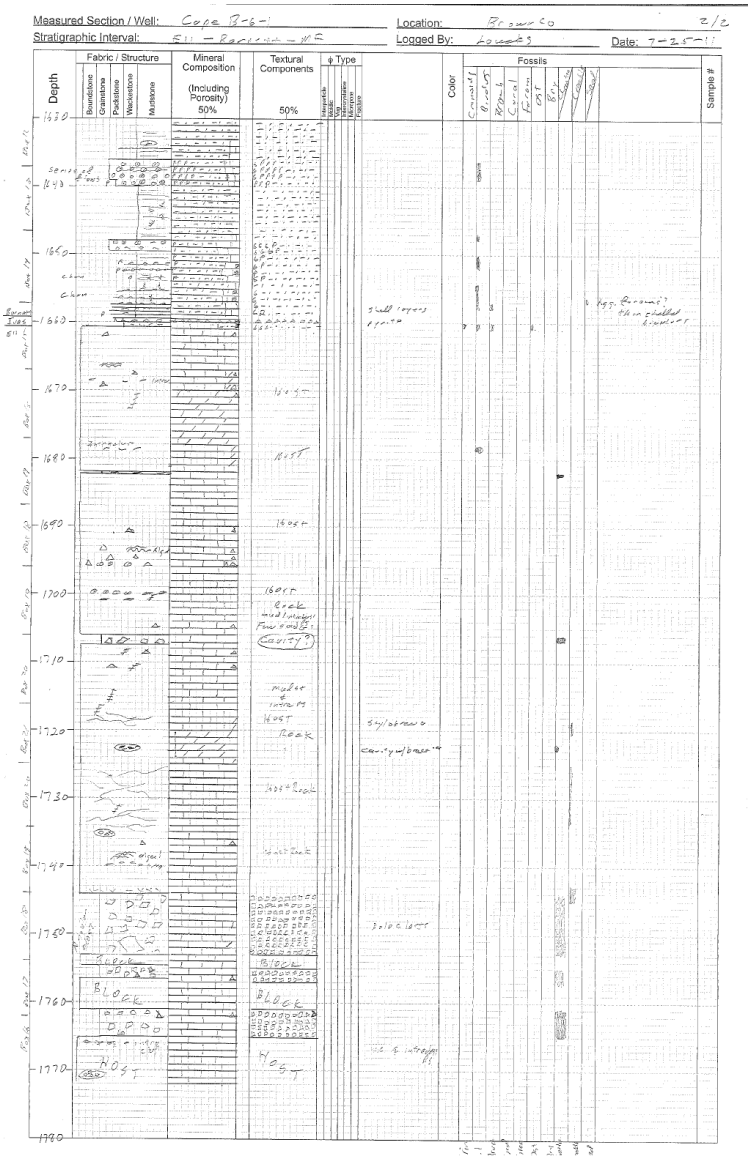
Measured Section / Well: Cope Rock-1
Location: Brown Co
Stratigraphic Interval: Ft. Riley – Barneston – WE
Logged By: Howard S
Date: 7-25-11
Fabric / Structure
Boundstone
Grainstone
Packstone
Wackestone
Mudstone
Mineral Composition (Including Porosity)
50%
Textural Components
50%
φ Type
Vugs
Moldic
Intercrystalline
Fracture
Color
Fossils
Sample #
Depth
1650
1660
1670
1680
1690
1700
1710
1720
1730
1740
1750
1760
1770
1780
Shell rmns
Frm.
Neg. Reserve?
thin shelled
brachiopod
Host
Rock
mud/intrapel
Fms and
cavity?
Host
Rock
Stylolaminated
cavity w/ bmnt
Host
Rock
Block
Block
Block
Host
Host

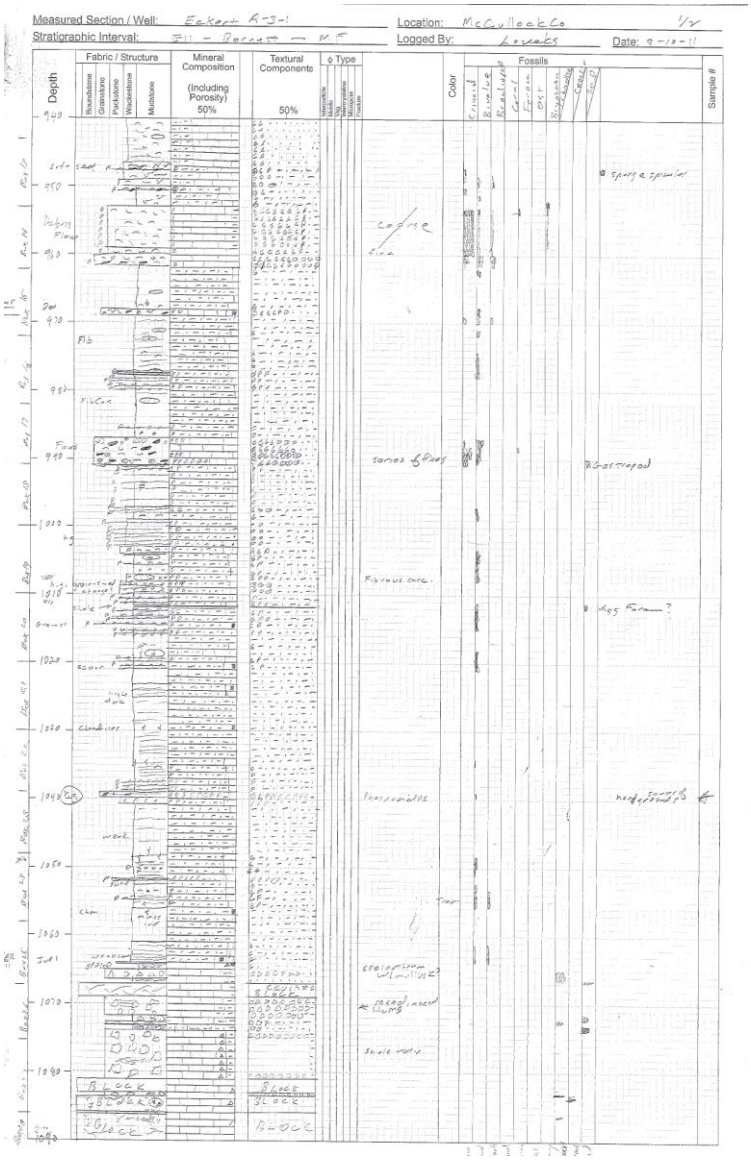
Measured Section / Well: Eckert A-3-1
Location: McCulloch Co
Stratigraphic Interval: Fl - Barnett - MF
Logged By: Loucks
Date: 9-10-11
Fabric / Structure
Mineral Composition (Including Porosity) 50%
Textural Components 50%
ϕ Type
Color
Fossils
Depth
Sample #
Boundstone
Grainstone
Packstone
Wackestone
Mudstone
Intercrystalline
Moldic
Vuggy
Interparticle
Fracture
Crinoid
Bryozoa
Brachiopod
Coral
Fusulinid
Ostracod
Algae
Gastropod
coarse
series of flows
fossiliferous
Flat pebble conglomerate
Algae Foram?
Brachiopod
Crinoid
Bryozoa
Coral
Fusulinid
Ostracod
Algae
Gastropod

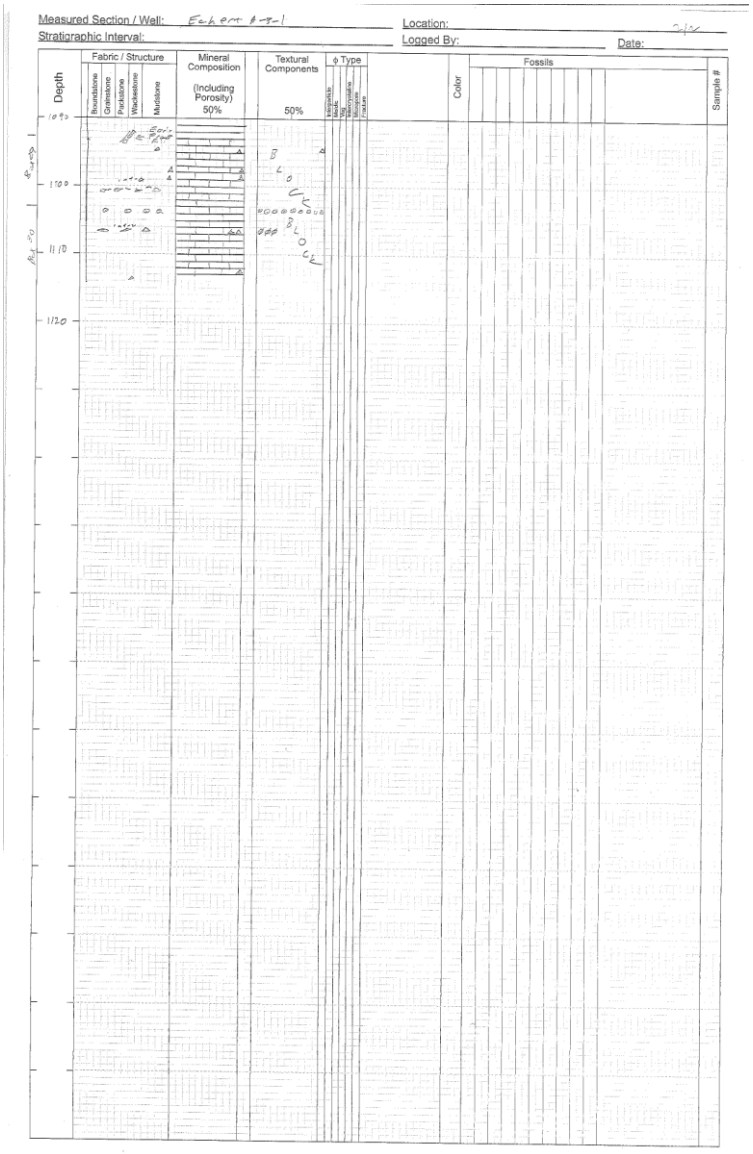
Measured Section / Well: Echem #1
Location:
Stratigraphic Interval:
Logged By:
Date:
Depth
Fabric / Structure
Boundstone
Grainstone
Packstone
Wackestone
Mudstone
Mineral Composition
(Including Porosity)
50%
Textural Components
50%
ϕ Type
Intercrystalline
Moldic
Vug
Fracture
Microvug
Channel
Color
Fossils
Sample #
1090
1100
1110
1120

MEASURED SECTION / WELL: Kouston o&m # C-2-5 Edwards LOCATION: San Saba Co 1/1

STRATIGRAPHIC INTERVAL: E11 - MF LOGGED BY: Loucks/Kappel DATE: Dec 28, 2007

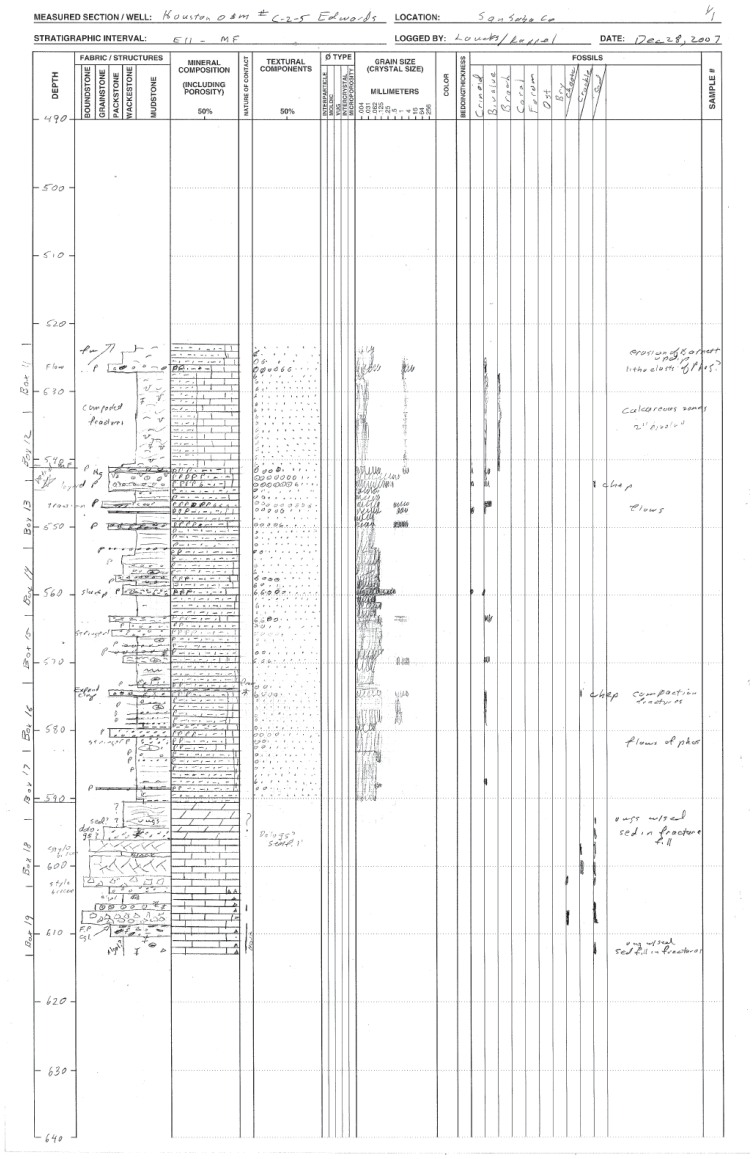

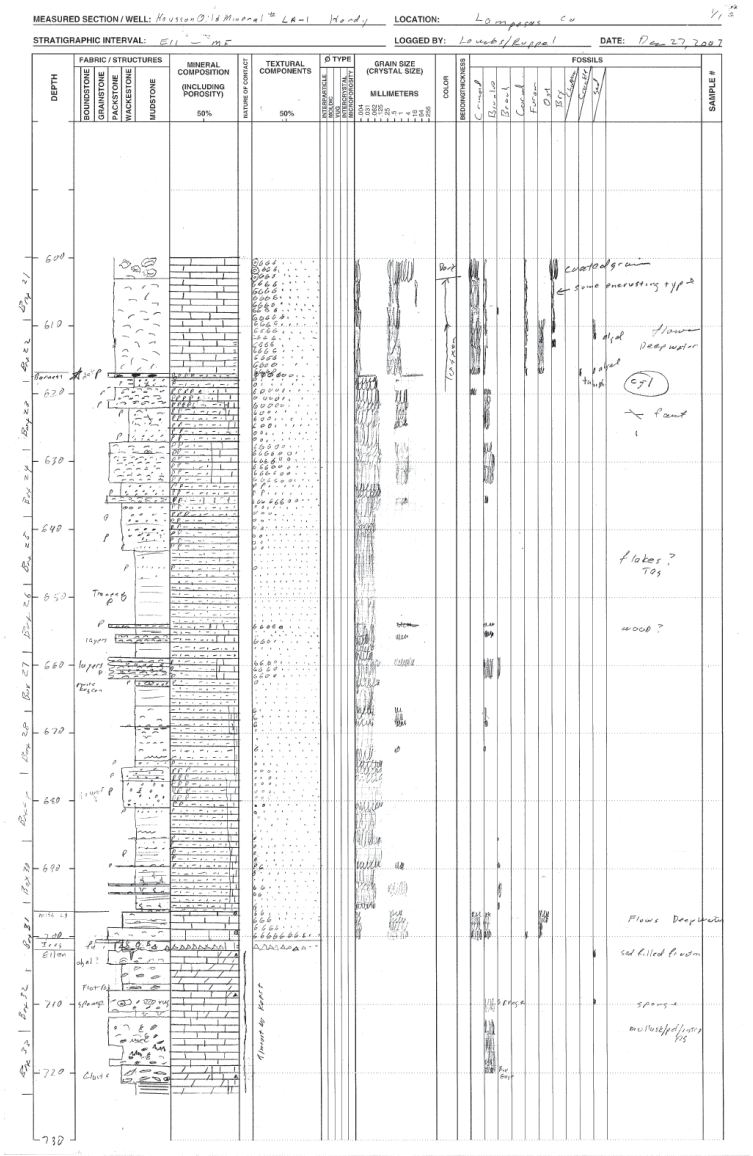

MEASURED SECTION / WELL: Houston Oil & Mineral # LA-1 Hardy

LOCATION: Lampasas Co

STRATIGRAPHIC INTERVAL: Ell – MF

LOGGED BY: Loucks/Ruppel

DATE: Dec 27, 2007

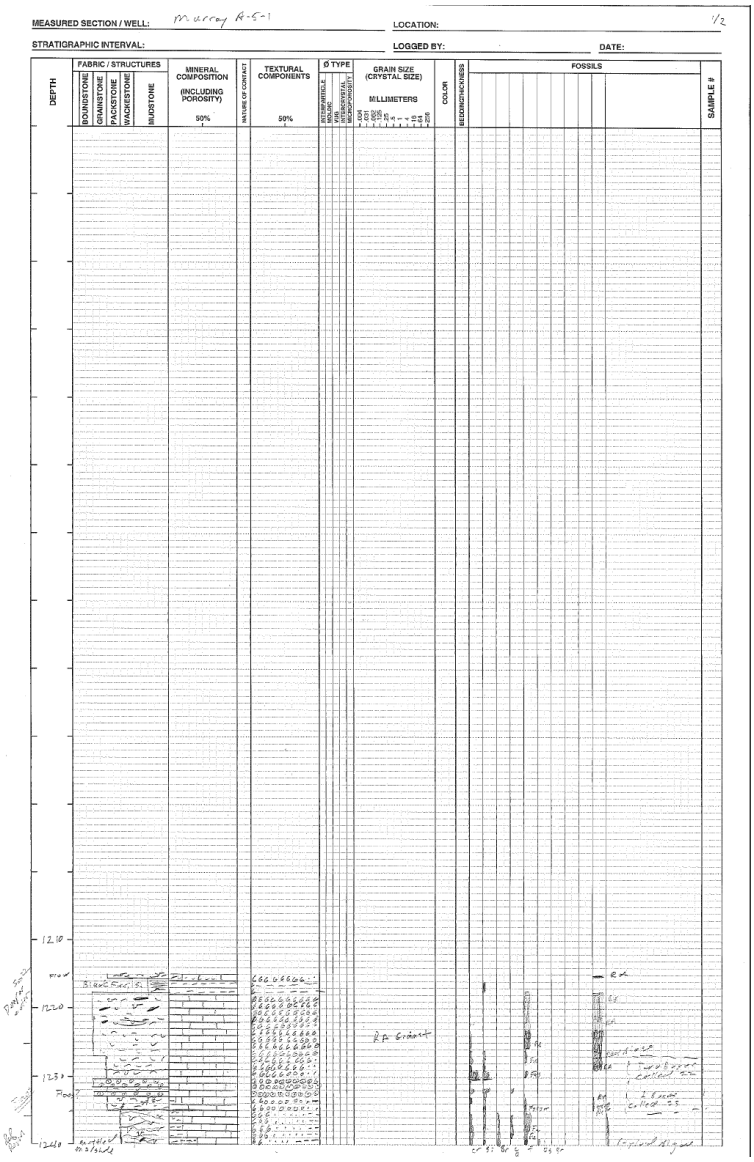
MEASURED SECTION / WELL: Murray A-5-1
LOCATION:
1/2
STRATIGRAPHIC INTERVAL:
LOGGED BY:
DATE:
DEPTH
FABRIC / STRUCTURES
BOUNDSTONE
GRAINSTONE
PACKSTONE
WACKESTONE
MUDSTONE
MINERAL COMPOSITION (INCLUDING POROSITY)
50%
NATURE OF CONTACT
TEXTURAL COMPONENTS
50%
Ø TYPE
INTERPARTICLE
MOLDIC
INTERCRYSTAL
INTERCRYSTAL
GRAIN SIZE (CRYSTAL SIZE)
MILLIMETERS
COLOR
BEDDING THICKNESS
FOSSILS
SAMPLE #
1210
1220
1230
1240

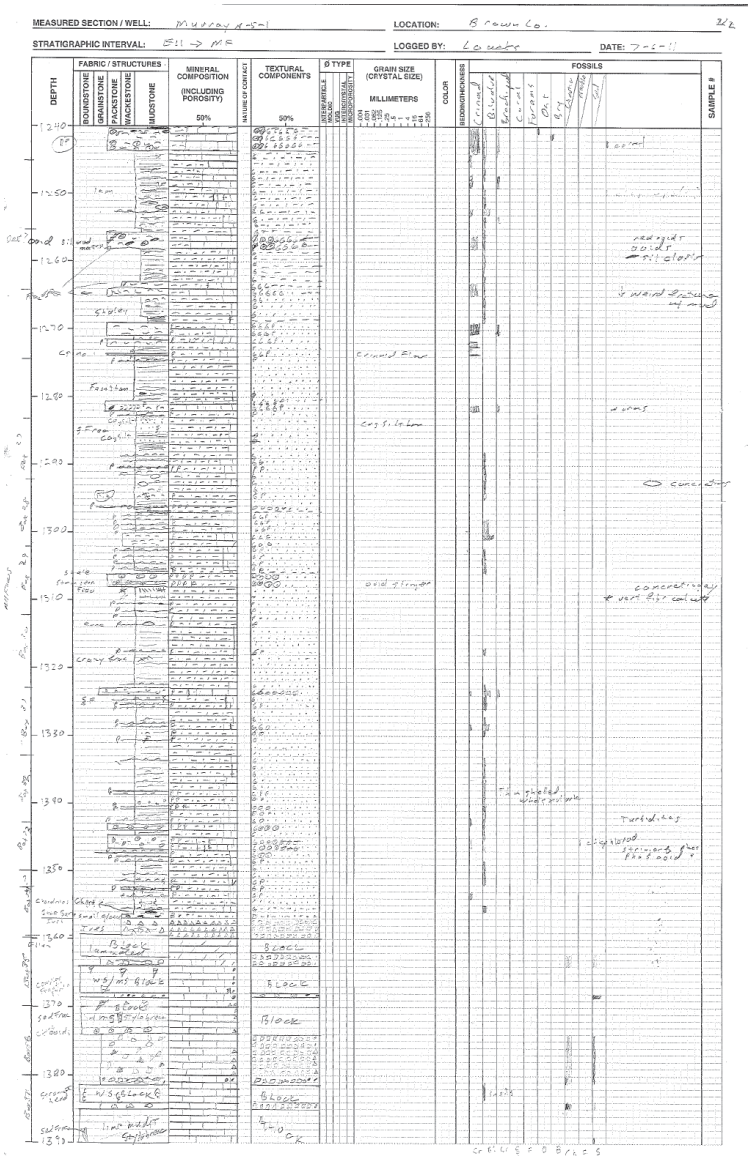
MEASURED SECTION / WELL:
LOCATION:
STRATIGRAPHIC INTERVAL:
LOGGED BY:
DATE:
DEPTH
FABRIC / STRUCTURES
BOUNDSTONE
GRAINSTONE
PACKSTONE
WACKESTONE
MUDSTONE
MINERAL COMPOSITION (INCLUDING POROSITY)
50%
TEXTURAL COMPONENTS
50%
GRAIN SIZE (CRYSTAL SIZE)
MILLIMETERS
COLOR
BEDDING THICKNESS
FOSSILS
SAMPLE #

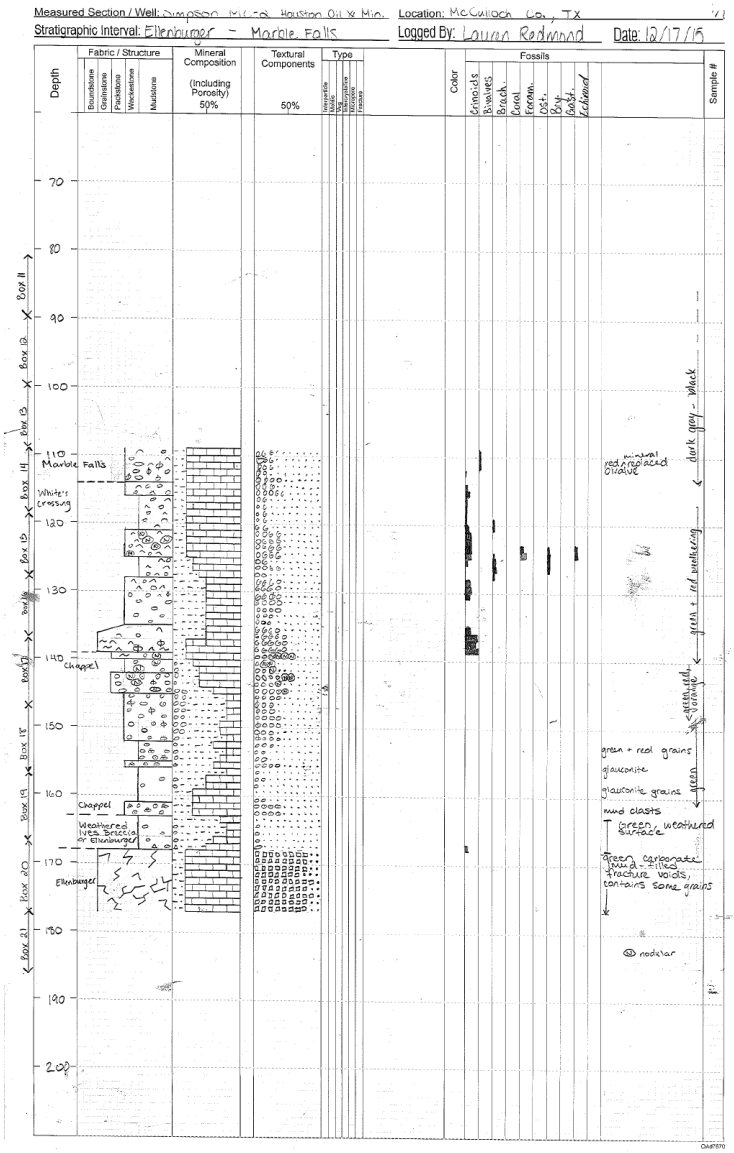
Measured Section / Well: Simpson Ritch Houston Oil & Min.
Location: McCulloch Co., Tx
Stratigraphic Interval: Ellenburger – Marble Falls
Logged By: Lauren Redmond
Date: 12/17/15
Fabric / Structure
Boundstone
Grainstone
Packstone
Wackestone
Mudstone
Mineral Composition (Including Porosity)
50%
Textural Components
50%
Type
Vugs
Fractures
Color
Fossils
Crinoids
Bivalves
Brach.
Coral
Foram.
Ost.
Gast.
Sample #
Depth
70
80
90
100
110
120
130
140
150
160
170
180
190
200
Box 11
Box 12
Box 13
Box 14
Box 15
Box 16
Box 17
Box 18
Box 19
Box 20
Box 21
Marble Falls
White's crossing
Chappel
Chappel
Weathered Ivey Breccia of Ellenburger
Ellenburger
dark gray - black
green + red grains
glauconite
glauconite grains
green
mud clasts
green, weathered surface
green carbonate mud-filled fracture voids, contains some grains
nodular

References

Amorosi, A., 1995, Glaucony and sequence stratigraphy: a conceptual framework of distribution in siliciclastic sequences: Journal of Sedimentary Research, v. B65, p. 419–425.

Arning, E. T., A. Lückge, C. Breuer, N. Gussone, D. Birgel, and J. Peckmann, 2009, Genesis of phosphorite crusts off Peru: Marine Geology, v. 262, p. 68–81.

Arthur, M. A. and H. C. Jenkyns, 1981, Phosphorites and paleoceanography: Oceanologica Acta, v. 45, p. 83-96.

Bailey, J. V., S. B. Joye, K. M. Kalanetra, B. E. Flood, and F. A. Corsetti, 2007, Evidence of giant sulphur bacteria in Neoproterozoic phosphorites: Nature, v. 445, p. 198–201.

Baturin, G. N., 1972, Phosphorus in Mud Waters of the Southeastern Atlantic: Okeanologiya, v. 12, no. 6, p. 1020–1027.

Baturin, G. N., 1982, Phosphorites on the sea floor: Developments in Sedimentology 33: Amsterdam, Elsevier, 343 p.

Baturin, G. N. and V. S. Savenko, 1985, Mechanism of formation of phosphorite nodules: Oceanology, v. 25, p. 747-750.

Bebout, D. G., and R. G. Loucks, 1984, Handbook for Logging Carbonate Rocks: University of Texas at Austin, Bureau of Economic Geology, Handbook No. 5, 43 p.

Bernhard, J. M. and C. E. Reimers, 1991, Benthic foraminiferal population fluctuations related to anoxia: Santa Barbara Basin: Biogeochemistry, v. 15, p. 127-149.

Berrang, P. G., and E. V. Grill, 1974, The effect of manganese oxide scavenging on molybdenum in Saanich Inlet, British Columbia: Marine Chemistry, v. 2, p. 125–148.

Blakey, R., 2005, Paleogeography and geologic evolution of North America; images that track the ancient landscapes of North America: http://jan.ucc.nau.edu/~rcb7/nam.html (accessed July 11, 2016).

Boggs, S. Jr., 1987, Principles of sedimentology and stratigraphy: Columbus, Ohio, Merrill Publishing Co., 784 p.

Bograd, S. J., F. B. Schwing, C. G. Castro, and D. A. Timothy, 2002, Bottom water renewal in the Santa Barbara Basin: Journal of Geophysical Research, v. 107, p. 3216-3224.

Brett, C. E., P. I. McLaughlin, S. R. Cornell, and G. C. Baird, 2004, Comparative sequence stratigraphy of two classic Upper Ordovician successions, Trenton Shelf (New York–Ontario) and Lexington Platform (Kentucky–Ohio): implications for eustasy and local tectonism in eastern Laurentia: Palaeogeography, Palaeoclimatology, Palaeoecology, v. 201, p. 295-329.

Burnett, W. C., 1977, Geochemistry and origin of phosphorite deposits from off Peru and Chile: Bulletin of the Geological Society of America, v. 88, p. 813-823.

Calvert, S. E. and T. F. Pedersen, 2007, Elemental proxies for paleoclimatic and paleoceanographic variability in marine sediments: Interpretation and Application: Developments in Marine Geology, v. 1, p. 567-644.

Cobbold, P. R., A. Zanella, N. Rodrigues, and H. Loseth, 2013, Bedding-parallel fibrous veins (beef and cone-in-cone): Worldwide occurrence and possible significance in terms of fluid overpressure, hydrocarbon generation and mineralization: Marine and Petroleum Geology, v. 43, p. 1-20.

Coleman M. L., D. B. Hedrick, D. R. Lovley, D. C. White, and K. Pye, 1993, Reduction of Fe(III) in sediments by sulphate-reducing bacteria: Nature, v. 361, p. 436-438.

Cook, P. J., J. H. Shergold, W. C. Burnett, and S. R. Riggs, 1990, Phosphorite research: a historical overview, in A. J. G. Notholt and I. Jarvis, eds., Phosphorite Research and Development: Geological Society Special Publication 52, p. l-22.

Cosmidis, J., K. Benzerara, G. Morin, V. Busigny, O. Lebeau, D. Jézéquel, V. Noël, G. Dublet, and G. Othmane, 2014, Biomineralization of iron-phosphates in the water column of Lake Pavin (Massif Central, France): Geochimica et Cosmochimica Acta, v. 126, p. 78–96.

Crowley, T. J., and S. K. Baum, 1991, Estimating Carboniferous sea-level fluctuations from Gondwanan ice extent: Geology, v. 19, p. 975-977.

Curtis, J.B., 2002, Fracture shale-gas systems: AAPG Bulletin, v. 86, no. 11, p. 1921-1938.

Dahanayake, K., and W. E. Krumbein, 1986, Microbial structures in oolitic iron formations: Mineralium Deposita, v. 21, p. 85–94.

Dunham, R. J., 1962, Classification of carbonate rocks according to depositional texture, in W.E. Ham, ed., Classification of carbonate rocks: AAPG Memoir 1, p. 62-84.

Emerson, S. R., and S. S. Huested, 1991, Ocean anoxia and the concentrations of molybdenum and vanadium in seawater: Marine Chemistry, v. 34, p. 177–196.

Erlich, R. N., and J. L. Coleman, Jr., 2005, Drowning of the Upper Marble Falls carbonate platform (Pennsylvanian), central Texas: A case of conflicting “signals?”: Sedimentary Geology, v. 175, p. 479-499.

Fielding, C. R., T. D. Frank, and J. L. Isbell, eds., 2008, Resolving the Late Paleozoic Ice Age in Time and Space: Geological Society of America Special Paper 441, 354 p.

Folk, R. L. and L. S. Land, 1975, Mg/Ca Ratio and Salinity: Two Controls over Crystallization of Dolomite: AAPG Bulletin, v. 59, no. 1, p. 60-68.

Folk, R. L., 1980, Petrology of Sedimentary Rocks: Austin, Texas, Hemphill Publishing Co., 182 p.

Föllmi, K. B., R. E. Garrison, and K. A. Grimm, 1991, Stratification in phosphatic sediments: Illustrations from the Neogene of Central California, in G. Einsele, W. Ricken and A. Seilacher, eds., Cycles and Events in Stratigraphy: Berlin, Springer, p. 492-507.

Föllmi, K. B., 1993, Phosphorus and phosphate-rich sediments: an environmental approach: Chemical Geology, v. 107, p. 375-378.

Föllmi, K. B., H. Weissert, M. Bisping, and H. Funk, 1994, Phosphogenesis, carbon-isotope stratigraphy, and carbonate-platform evolution along the Lower Cretaceous northern Tethyan margin: Geological Society of America Bulletin, v. 106, p. 729-746.

Föllmi, K. B., 1996, The phosphorus cycle, phosphogenesis and marine phosphate-rich deposits: Earth-Science Review, v. 40, p. 55-124.

Föllmi, K. B., 2016, Sedimentary Condensation: Earth-Science Reviews, v. 152, p. 143-180.

Glenn, C. R., M. A. Arthur, H. W. Yeh, and W. C. Burnett, 1988, Carbon isotopic composition and lattice-bound carbonate of Peru-Chile margin phosphorites, in W. C. Burnett and P. N. Froelich, eds., The Origin of Marine Phosphorite, The Results of the R.V. Robert D. Conrad Cruise 23-06 to the Peru Shelf: Marine Geology, v. 80, p. 287-307.

Glenn, C. R. and M. A. Arthur, 1990, Anatomy and origin of a Cretaceous phosphorite-greensand giant, Egypt: Sedimentology, v. 37, p. 123-154.

Glenn, C. R., M. A. Arthur, J. M. Resig, W. C. Burnett, W. E. Dean, and R. A. Jahnke, 1994a, Are modern and ancient phosphorites really so different?, in A. Iijima, A. M. Abed and R. E. Garrison, eds., Siliceous, Phosphatic and Glauconitic Sediments of the Tertiary and Mesozoic: Proceedings of the 29th International Geological Congress Part C. VSP, Utrecht, p. 159-188.

Glenn, C. R., K. B. Föllmi, S. R. Riggs, G. N. Baturin, K. A. Grimm, J. Trappe, A. M. Abed, C. Galli-Olivier, R. E. Garrison, A. V. Ilyin, C. Jehl, V. Rohrlich, R. M. Y. Sadaqah, M.Schidlowski, R. E. Sheldon, and H. Siegmund, 1994b, Phosphorus and phosphorites: sedimentology and environments of formation, in K. B. Föllmi, ed., Concepts and Controversies in Phosphogenesis: Eclogae geologicae Helvetiae, v. 87, p. 747–788.

Goldhammer, T., V. Brüchert, T.G. Ferdelman, and M. Zabel, 2010, Microbial sequestration of phosphorus in anoxic upwelling sediments: Nature Geoscience, v. 3, p. 557-561.

Gradstein, F., J. Ogg, M. Schmitz, and G. Ogg, eds., 2012, The Carboniferous Period: The Geological Time Scale: Amsterdam, Elsevier, v. 2, p. 603-651.

Grayson, R. C. and G. K. Merrill, eds., 1991, Carboniferous geology and tectonic history of the Southern Fort Worth (Foreland) Basin and Concho Platform, Texas: AAPG, 1991 Annual Convention, Dallas Geological Society Guidebook, Field Trip No. 13, 67 p.

Groves, J. R., 1991, Fusulinacean biostratigraphy of the Marble Falls Limestone (Pennsylvanian), western Llano region, central Texas: Journal of Foraminiferal Research, v. 21, p. 67-95.

Gutschick, R., and C. Sandberg, 1983, Mississippian continental margins on the conterminous United States, in D. J. Stanley and G. T. Moore, The shelf break: Critical interface on continental margins: SEPM Special Publication 33, p. 79–96.

Hiatt, E., and D. A. Budd, 2001, Sedimentary phosphate formation in warm shallow waters: new insights into the palaeoceanography of the Permian Phosphoria Sea from analysis of phosphate oxygen isotopes. Sedimentary Geology, v. 145, p. 119-133.

Hass W. H., 1953, Conodonts of Barnett Formation of Texas, Geological Survey Professional Paper 243-F, p 69-94.

Heckel, P. H., 1994, Evaluation of evidence for glacio-eustatic control over marine Pennsyvlanian cyclothems in North America and consideration of possible tectonic effects, in J. M. Dennison and F. R Ettensohn, eds., Tectonic and Eustatic Controls on Sedimentary Cycles, SEPM, Tulsa, OK: Concepts in Sedimentology and Paleontology, v. 4, p. 65-87.

Heckel, P. H., 2008, Pennsylvanian cyclothems in Midcontinent North America as far-field effects of waxing and waning of Gondwana ice sheets, in C. R. Fielding, T. D. Frank, and J. L. Isbell, eds., Resolving the Late Paleozoic Ice Age in Time and Space: Geological Society of America Special Paper 441, p. 275–289.

Heggie, D. T., G. W. Skyring, G. W. O'Brien, C. Reimers, A. Herczeg, D. J. W. Moriarty, W. C. Burnett., and A. R. Mimes, 1990, Organic carbon cycling and modern phosphorite formation on the east Australian continental margin: an overview, in A. J. G. Notholt and I. Jarvis, eds., Phosphorite Research and Development. Geological Society Special Publication 52, p. 87-117.

Henry, J. D., 1982, Stratigraphy of the Barnett Shale (Mississippian) and Associated Reefs in the northern Fort Worth Basin: Dallas Geological Society, p. 157-177.

Hesselbo, S. P., A. L. Coe, and H. C. Jenkyns, 1990, Recognition and documentation of depositional sequences from outcrop: an example from the Aptian and Albian on the eastern margin of the Wessex Basin. Journal of the Geological Society of London, v. 147, p. 549-559.

Hoelke, J. D., 2011, Chemostratigraphy and Paleoceanograpy of the Mississippian Barnett Formation, Southern Fort Worth Basin, Texas, USA, Master's thesis, University of Texas at Arlington, Arlington, Texas, 108 p.

Jarvis, I., W. C. Burnett, Y. Nathan, F. Almbaydin, K. M. Attia, L. N. Castro, R. Flicoteaux, M. E. Hilmy, V. Husain, A. A. Qutawna, A. Serjani, and Y. N. Zanin, 1994, Phosphorite Geochemistry: State-of-the-art and Environmental Concerns, in K. B. Föllmi, ed., Concepts and Controversies in Phosphogenesis: Eclogae geologicae Helvetiae, v. 87, p. 643–700.

Jiang, G., S. Zhang, X. Shi, X. Wang, 2008, Chemocline instability and isotope variations of the Ediacaran Doushantuo basin in South China: Science in China Series D: Earth Sciences, v. 51, p. 1560–1569.

Joachimski, M. M., P. H. von Bitter, and W. Buggish, 2006, Constraints on Pennsylvanian glacioeustatic sea-level changes using oxygen isotopes of conodont apatite: Geology, v. 34, p. 277–280.

Kier, R. S., 1972, Carboniferous stratigraphy of Eastern San Saba County and Western Lampasas County, Texas, unpublished Doctoral Dissertation, University of Texas at Austin, Austin, Texas, 509 p.

Kier, R. S., L. F. Brown, Jr., and E. F. McBride, 1979, The Mississippian and Pennsylvanian (Carboniferous) systems in the United States-Texas: U.S. Geological Survey Professional Paper 1110-S, p. S1-S45.

Kier, R. S., 1980, Depositional history of the Marble Falls Formation of the Llano region, Central Texas in D. Windle, ed., Guidebook to the annual field trip of the West Texas Geological Society, October 19-21, 1980, Publication, v. 80-73, West Texas Geological Society, p. 59-75.

Klein, G. D., 1993, Paleoglobal change during deposition of cyclothems: calculating the contributions of tectonic subsidence, glacial eustasy and long-term climate influences on Pennsylvanian sea-level change: Tectonophysics, v. 222, p. 333-360.

Krajewski, K. P., 1984, Early diagenetic phosphate cements in the Albian condensed glauconitic limestone of the Tatra Mountains, western Carpathians: Sedimentology, v. 31, p. 443-470.

Krajewski, K. P., 1989, Organic geochemistry of a phosphorite to black shale transgressive succession: Wilhelmöya and Janusfjellet Formations (Rhaetian–Jurassic) in Central Spitsbergen, Arctic Ocean: Chemical Geology, v. 74, p. 249-263.

Liner R. T., W. L. Manger, and D. L. Zachry, 1978, Conodont evidence for the Mississippian-Pennsylvanian Boundary Northeastern Llano Region, Central Texas: Texas Journal of Science, v. 31, no. 4, p. 309-317.

Loucks R. G., and S. C. Ruppel, 2007, Mississippian Barnett Shale: Lithofacies and Depositional Setting of a Deepwater Shale-Gas Succession in the Fort Worth Basin, TX. AAPG Bulletin, v. 91, p. 597-601.

Loucks R. G., R. M. Reed, S. C. Ruppel, and D. M. Jarvie, 2009, Morphology, genesis and the distribution of nanometer-scale pores in siliceous mudstones of the Mississippian Barnett Shale: Journal of Sedimentary Research, v. 79, p. 848-861.

Lovick, G. P., G. C. Mazzine, and D. A. Kotila, 1982, Atokan clastics- depositional environments in a foreland basin in C. A. Martin, ed., Petroleum geology of the Fort Worth Basin and Bend Arch area: Dallas Geological Society, p. 129-155.

Manger, W. L., and P. K. Sutherland, 1984, Preliminary conodont biostratigraphy of the Morrowan-Atokan boundary (Pennsylvanian), eastern Llano Uplift, central Texas in P. K. Sutherland and W.L. Manger, eds., the Atokan Series (Pennsylvanian) and its boundaries; a symposium: Oklahoma Geological Survey, v. 136, p. 115-121.

Meckel, L. D., D. G. Smith, and L. A. Wells, 1992, Ouachita Foredeep Basins: Regional Paleogeography and Habitat of Hydrocarbons in R.W. Macqueen and D.A. Leckie, eds., Foreland Basins and Fold Belts: AAPG Memoir 55, p. 427-444.

Merrill, G. K., 1980, Road log-Day two, in Geology of the Llano region, central Texas: Guidebook to the Annual Field Trip of The West Texas Geological Society, Oct. 19-21, 1980, p. 60-199.

Monroe, R. M., 2009, Petrographic and Stratigraphic Analysis of the Barnett Shale (Mississippian) in Hill County, Texas: Evidence for Eustacy and Tectonism, Master's thesis, Texas Christian University, 154 p.

Montgomery, S. L., D. M. Jarvie, K. A. Bowker, and R. M. Pollastro, 2005, Mississippian Barnett Shale, Fort Worth Basin, northcentral Texas: Gas-shale play with multi-trillion cubic foot potential: AAPG Bulletin, v. 89, p. 155–175.

Morgan, W. A., 2012, Sequence stratigraphy of the great American carbonate bank, in J. R. Derby, R. D. Fritz, S. A. Longacre, W. A. Morgan, and C. A. Sternbach, eds., The great American carbonate bank: The geology and economic resources of the Cambrian — Ordovician Sauk megasequence of Laurentia: AAPG Memoir 98, p. 37–79.

Mulder, T., and J. Alexander, 2001, The physical character of subaqueous sedimentary density flows and their deposits: Sedimentology, v. 48, p. 269–299.

Namy, J. N., 1974, Origin of a lower Pennsylvanian depositional cycle: Journal of Sedimentary Petrology, v. 44, no. 3, p. 793-803.

Odin, G. S., and A. Matter, 1981, De glauconiarum origine: Sedimentology, v. 28, p. 611-641.

Papazis, P. K., 2005, Petrographic Characterization of the Barnett Shale, Fort Worth Basin, Texas, Master's thesis, University of Texas at Austin, Austin, TX, 142 p.

Parnell, J., C. Honghan, D. Middleton, T. Haggan, and P. Carey, 2000, Significance of fibrous mineral veins in hydrocarbon migration: fluid inclusion studies: Journal of Geochemical Exploration, v. 69-70, p. 623-627.

Pemberton, G., J. A. MacEachern, and M. Gingras, 2009, Atlas of trace fossils: the recognition of common trace fossils in outcrop and cores: London: Elsevier Science, 130 p.

Pike, J., A. E. S. Kemp, 1996. Silt aggregates in laminated marine sediment produced by agglutinated Foraminifera. Journal of Sedimentary Research 66, 625–631.

Pollastro, R. M., D. M. Jarvie, R. J. Hill, and C. W. Adams, 2007, Geologic framework of the Mississippian Barnett Shale, Barnett – Paleozoic total petroleum system, Bend arch – Fort Worth Basin, Texas: AAPG Bulletin, v. 91, no. 4, p. 405 – 436

Proust, J. N., B. I. Chuvashov, E. Vennin, and T. Boisseau, 1998, Carbonate platform drowning in a foreland setting: the Mid-Carboniferous platform in western Urals (Russia): Journal of Sedimentary Research, v. 68, p. 1175–1188.

Pufahl, P. K., K. A. Grimm, A. M. Abed, and R. M. Y. Sadaqah, 2003, Upper Cretaceous (Campanian) phosphorites in Jordan: implications for the formation of a south Tethyan phosphorite giant: Sedimentary Geology, v. 161, p. 175-205.

Reed, R. M., and R. G. Loucks, 2015, Low-Thermal-Maturity (<0.7% VR) Mudrock Pore Systems: Mississippian Barnett Shale, Southern Fort Worth Basin: GCAGS Journal, v. 4, p. 15-28.

Reitlinger, E. A., 1975, Paleozoogeografiya vizeyskikh I rannenamyurskikh basseynov po foraminiferam. Paleozoogeography of Visean and early Namurian basins based on foraminifera: Voporsy Mikropaleontologi, v. 18, p. 3-20.

Riggs, S. R., 1984, Paleoceanographic model of Neogene phosphorite deposition, U.S. Atlantic continental margin: Science, v. 223, p. 123–131.

Riggs, S. R. and R. P. Sheldon, 1990, Paleoceanographic and paleoclimatic controls of the temporal and geographic distribution of Upper Cenozoic continental margin phosphorites, in W.C. Burnett and S.R. Riggs, eds., Phosphate Deposits of the World: Vol. 3, Genesis of Neogene to Recent Phosphorites: Cambridge University Press, p. 207-222.

Rodrigues, N. T., 2008, Fracturation hydraulique et forces de courant: modélisation analogique et données de terrain, Doctoral Dissertation, University of Rennes, Rennes, France, 164 p.

Rodrigues, N., P. R. Cobbold, H. Løseth, and G. Ruffet, 2009, Widespread bedding parallel veins of fibrous calcite ("beef") in a mature source rock (Vaca Muerta Fm, Neuquén Basin, Argentina): evidence for overpressure and horizontal compression: Journal of the Geological Society, London, v. 166, p. 695-709, doi 10.1144/0016-76492008-111.

Roepke, H. H., 1970, Petrology of carbonate units in the Canyon Group (Missourian Series), Central Texas, Doctoral dissertation, University of Texas at Austin, Austin, Texas, 254 p.

Ross, C. A., and J. R. P. Ross 1987, Biostratigraphic zonation of Late Paleozoic depositional sequences in C.A. Ross, and D. Harman, eds., Timing and Depositional History of Eustatic Sequences Constraints on Seismic Stratigraphy: Cushman Foundation for Foraminiferal Research, Special Publication no. 24, p. 150-168.

Rowe, H. D., R. G. Loucks, S. C. Ruppel, and S. M. Rimmer, 2008, Mississippian Barnett Formation, Fort Worth Basin, Texas: Bulk geochemical inferences and Mo-TOC constraints on the severity of hydrographic restriction: Chemical Geology, v. 257, p. 16-25.

Rowe, H. D., E. N. Hughes, and R. Robinson, 2012, The quantification and application of handheld energy-dispersive x-ray fluorescence (ED-XRF) in mudrock chemostratigraphy and geochemistry: Chemical Geology, v. 324–325, p. 122-131.

Ruppel, S. C., 1989, Summary of Mississippian stratigraphy in north and north-central Texas, in C. E. Mear, C. L. McNulty, and M. E. McNulty, eds., A Symposium on the Petroleum Geology of Mississippian Carbonates in North-Central Texas: Fort Worth Geological Society and Texas Christian University, p. 49– 55.

Schieber, J., 2009, Discovery of agglutinated benthic foraminifera in Devonian black shales and their relevance for the redox state of ancient seas: Paleogeography, Palaeoclimatology, Palaeoecology, v. 271, p. 292-300.

Schulz, H. N., and H. D. Schulz, 2005, Large sulfur bacteria and the formation of phosphorite: Science, v. 307, p. 416-418.

Schutter, S. R., 1996, The Glenwood Shale as an example of a Middle Ordovician condensed section, in B. J. Witzke, G. A. Ludvigson, and J. Day, eds., Paleozoic Sequence Stratigraphy: Views from the North American Craton: Geological Society of America, Special Paper 306, p. 55–66

Shaffer, G., 1986, Phosphate pumps and shuttles in the Black Sea: Nature, v. 321, p. 5l5-517.

Sheldon, R. P., 1980, Episodicity of phosphate deposition and deep ocean circulation - a hypothesis, in Y. K. Bentor, ed., Marine Phosphorites - Geochemistry, Occurrence, Genesis: Society Economic Paleontologists and Mineralogists, Special Publication, v. 29, p. 239-247.

Shields, G. A., H. Kimura, J. Yang, and P. Gammon, 2004, Sulphur isotopic evolution of Neoproterozoic–Cambrian seawater: new francolite-bound sulphate δ34S date and a critical appraisal of the existing record: Chemical Geology, v. 204, p. 163-182.

Shen, Y., M. Schidlowski, and X. Chu, 2000, Biogeochemical approach to understanding phosphogenic events of the terminal Proterozoic to Cambrian. Palaeogeography, Palaeoclimatology, Palaeoecology, v. 158, p. 99–108.

Siegmund, H., J. Trappe, and W. Oschmann, 2002, Sequence stratigraphic and genetic aspects of the Tournaisian "liegender Alaunschiefer" and adjacent beds: International Journal of Earth Sciences, v. 91, p. 934-949.

Soudry, D., I. Segal, Y. Nathan, C.R. Glenn, L. Halicz, Z. Lewy, and D.L. von der Haar, 2004, 44Ca/42Ca and 143Nd/144Nd isotope variations in Cretaceous–Eocene Tethyan francolites and their bearing on phosphogenesis in the southern Tethys: Geology, v. 32, p. 389-392.

Suan, G., K. B. Föllmi, T. Adatte, B. Bomou, J. Spangenberg, and B. van de Schootbrugge, 2011, Major environmental change and bonebed genesis prior to the Triassic–Jurassic mass extinction: Journal of the Geological Society, v. 169, p. 191-200.

Thompson, D. M., 1982, Atoka Group (lower–middle Pennsylvanian), northern Fort Worth basin, Texas: Terrigenous depositional systems, diagenesis, and reservoir distribution and quality: University of Texas at Austin, Bureau of Economic Geology, Report of Investigations No. 125, 62 p.

Thompson, D.M., 1988, Fort Worth Basin, in L.L. Sloss, ed., The Geology of North America: Geological Society of America, vol. D-2, p. 346-352.

Trappe, J., 1998, Phanerozoic phosphorite depositional systems: a dynamic model for a sedimentary resource system: New York, Springer, 316 p.

Trela, W., 1998, Sedimentary environment of the condensed Ordovician limestones from Mójcza section (Holy Cross Mts.): Geological Quarterly, v. 42, p. 289-300.

Turner, N. L., 1970, Carboniferous stratigraphy of western San Saba County, Texas, unpublished Doctoral Dissertation, University of Texas at Austin, Austin, Texas, 378 p.

Van Cappellen. P., 1991, The Formation of Marine Apatite: A Kinetic Study. Doctoral Dissertation, Yale University, New Haven. 240 pp.

Veevers, J. J, and C. McA. Powell, 1987, Late Paleozoic glacial episodes in Gondwanaland reflected in transgressive-regressive depositional sequences in Euramerica: Geological Society of America Bulletin, v. 98, no. 7-8, p. 475-487.

Verardo,D. J., P. N. Froelich, and A. McIntyre, 1990, Determination of organic carbon and nitrogen in marine sediments using the Carlo Erba NA-1500: Deep-Sea Research, v. 37, p. 157-165.

Walper, J. L., 1982, Plate tectonic evolution of the Fort Worth Basin, in C.A. Martin, ed., Petroleum Geology of the Fort Worth Basin and Bend Arch Area: Dallas Geological Society, p. 237-251.

White, J.R., 1948, A study of the Mississippian deposits in the subsurface of North-Central Texas: Master's thesis, Texas Christian University, Fort Worth, Texas, 79 p.

Wilkin, R. T., H. L. Barnes, and S. L. Brantley, 1996, The size distribution of framboidal pyrite in modern sediments: An indicator of redox conditions: Geochimica et Cosmochimica Acta, v. 60, p. 3897–3912.

Wilkin, R. T., M. A. Arthur, and W. E. Dean, 1997, History of water column anoxia in the Black Sea indicated by pyrite framboids size distributions: Earth and Planetary Science Letters, v. 148, p. 517– 525.

Wignall, P. B., 1994, Black Shales: Oxford Monographs on Geology and Geophysics Book 30: Oxford University Press, 127 p.

Wood, S. G., 2013, Lithofacies, Depositional Environments, and Sequence Stratigraphy of the Pennsylvanian (Morrowan-Atokan) Marble Falls Formation, Central Texas, Master's thesis, University of Texas at Austin, Austin, Texas, 276 p.